ISTC Project # 3813

Phase relations in corium systems (PRECOS)

Annual Technical Report

on the work performed from 01.06. 2009 to 31.05. 2010

(Second year)

Federal public unitary company "Alexandrov Scientific Research Institute of Technology" (FGUP NITI)

Project Manager	**Sevostyan V. Bechta** **Dr. (Tech.Sci.)**	
Director General	**Vyacheslav A. Vasilenko** **Dr. (Tech.Sci.), Prof.**	

October 2010

This work is financially supported by the European Union and performed under the contract with the International Science and Technology Center (ISTC), Moscow.

Title of the Project:	**Phase relations in corium systems (PRECOS)**
Contracting Institute:	Federal public unitary company "Alexandrov Scientific Research Institute of Technology" (FGUP NITI
Participating Institutes:	ITES OIVT RAS
Commencement Date:	01.06.2008
Duration:	36 months
Project Manager	S.V. Bechta, Dr. Tech. Sci. Head of department, NITI
tel.:	+7(813-69) 60 625
fax:	+7(813-69) 23 961
e-mail:	rital@sbor.net

1. Brief description of the work plan: objective, expected results, technical approach

Main Project objective is the experimental and theoretical evaluation of data on phase diagrams, which are important for modeling corium systems, in particular:

- concentration correlations of liquidus and solidus systems;
- coordinates of eutectic points;
- solubility limits of components in the solid phase;
- compositions of coexisting liquids in the miscibility gap.

The list of studied phase diagrams, objectives of experimental series and number of experiments are given in the experimental matrix (Table 1.1), which was updated at the meeting with collaborators.

Project results will be used to:

- optimize thermodynamic databases, NUCLEA in particular;
- refine numerical thermodynamic models, specifically in the stratification modeling;
- analyze safety of operating and designed NPPs.

Experimental studies within the projects were carried out on the RASPLAV-3 and RASPLAV-4 test facilities adjusted for compositions, which have considerably different

properties. To prepare melts with temperatures up to 3300 K the method of induction melting in a cold crucible (IMCC) was used. The method has the following features:

- power deposition in the melt;
- presence of crystallized melt (crust) between the melt and cold crucible wall, which prevents the mass transfer of crucible material into the melt.

The combination of contact-free heating and non-polluting melting of oxides provides:

- melt having the purity of the initial materials;
- advantage of a considerable superheating of melt above the liquidus temperature, also for the chemically active oxidic materials;
- advantage of meting and long-term maintenance of oxidic system in the molten condition, both in the inert and oxidizing atmosphere;
- universality and compactness of the melting device.

RASPLAV-3,4 setups can produce up to 2 kg of high-temperature corium melt in the inert and oxidizing atmospheres.

Medium-scale experiments determined liquidus and solidus temperatures by the visual polythermal analysis in the cold crucible (VPA IMCC), examined melt stratification and synthesized samples for studies using other methods.

The small-scale experiments determined liquidus and solidus temperatures using the following methods:

- visual polythermal analysis in the Galakhov microfurnace (VPA GM).
- differential thermal analysis (DTA)
- high-temperature microscopy (HTM)
- laser pulse heating (LPH).

The following methods were used in the physicochemical analysis of corium samples:

- X-ray fluorescence (XRF) and chemical analysis (ChA) – to determine elemental composition.
- X-ray diffractometry (XRD) and energy dispersion X-ray (EDX) – to determine phase composition and number of elements in the identified phases.
- Scanning electron microscopy (SEM) – to determine microstructure of sample.

Table 1.1 – Experimental matrix

Task	Composition	Atmosphere	Experimental data	Priority level	No of tests in accordance with Work plan/completed
1	U-Zr-Fe-O	Argon	Liquidus and solidus temperatures (T_{liq}, T_{sol}), tie lines in the miscibility gap	1	6/8[1]
2	ZrO_2-FeO_y	Air and mixtures with controlled O_2 partial pressure	T_{liq}, T_{sol}, solubility limits	2	3/3[2]
	UO_2-SiO_2	Neutral	T_{liq}, T_{sol}, eutectic point	1	7/(5[3]+40[4])
	CaO-UO_2			1	7/7[3]
3	UO_2-FeO-SiO_2		T_{liq}, T_{sol}, solubility limits, eutectic point, tie lines in the miscibility gap, ternary eutectic point	1	10/(1[3]+4[4])
	UO_2-FeO-CaO		T_{liq}, T_{sol}, solubility limits, ternary eutectic point		10/1[3]
	ZrO_2 - FeO - SiO_2		Ternary eutectic point	2	2/0
	ZrO_2 - FeO - CaO		Ternary eutectic point		2/0
4	Prototypic multi-component corium	Argon or air	Eutectic point for the composition (atmosphere) proposed by partners from - France (1 composition) - Germany (1 composition) - Russia (1 composition)	2	3/0

Note: [1]- LPH (Zr-O), [2]- HTM, [3]- VPA IMCC, [4]- VPA in the Galakhov microfurnace

2. Technical progress during the second year

In accordance with the experimental matrix (Table 1) during the second project year the following tasks on binary oxidic systems UO_2-SiO_2, UO_2-CaO, ZrO_2-FeO_x and metal-oxidic system U-Zr-Fe-O were implemented.

Task 1 - Investigation of various compositions of the metal-oxidic system aimed at determining T_{liq}, T_{sol} and tie-lines in the miscibility gap.
Subtask 1.2 Experimental investigations and analysis of produced data.

Task 2 - Study of binary oxidic systems.
Subtask 2.2 Experimental investigations and analysis of produced data.

Task 3 - Study of ternary oxidic systems.
Subtask 3.2 Experimental investigations and analysis of produced data.

The following work has been completed during the second year:

Task 1 Investigation of various compositions of the metal-oxidic system aimed at determining T_{liq}, T_{sol} and tie-lines in the miscibility gap

Subtask 1.2.: Experimental investigations and primary analysis of produced data.

Main project activities of the second year performed in the Institute of High Temperatures of the Russian Academy of Sciences (IHT RAS) by LPH:

- Calibration of high-speed multi-channel pyrometer against the blackbody;
- Measurement of the temperature field on the studied specimen surface with high time resolution;
- Fine-tuning of technology and fabrication of specimens of the ZrO_2–FeO system in a wide range of composition changes from ZrO_2 to the eutectic point;
- Preliminary study of phase transitions in the ZrO_2–FeO system in the temperature region above the eutectic temperature;
- Measurement of the CaO melting temperature;
- Further development of the mathematical model describing the dynamics of non-congruent melting and solidification in two-component materials.
- Development of the model for uranium oxide melting based on the defect model of crystalline lattice.

Theoretical studies

1. Mathematical and numerical modeling of non-congruent phase transitions in the two-component materials.

A proposed mathematical model describes the dynamics of non-congruent phase transitions (melting – solidification) in two-component materials at their surface heating by laser pulses. The model is based on the main assumption about the local thermodynamic equilibrium throughout the condensed phase, including the boundaries of regions with different phase states. The main parameters characterizing material conditions are temperature T, mass concentration of one of the components C and mass fraction of solid phase α. Dynamics of their transformation is described by the differential equations in partial derivatives, which are the mathematical formulation of the laws of conservation of mass and energy in the framework of continuum model. It is assumed that energy transfer is determined by heat transfer and diffusion, and mass transfer – only by diffusion (the Fick law). Main difference of this model from those previously published is in the assumed possibility that the condensed phase can have two-phase regions 'solid phase – melt'. Transfer processes in these regions are described by the model of "parallel conductivities": alternating layers of solid and liquid phases of variable thickness; in each point they have the condition of local thermodynamic equilibrium.

Numerical modeling was made for a 1D case, which describes well the real experimental conditions, when a characteristic thickness of a layer heated during pulse t_l is much smaller than the diameter of laser beam d_l. Main objective of the first stage was in comparison of produced results with previously made calculations in the framework of so-called "Stephan model", which neglects a possible formation of two-phase systems in the material. Melting and solidification of non-stoichiometric UO_x ($x=2.17$) was modeled, when the specimen was subjected to the impact of real laser pulse q_{las} with characteristic duration $t_l = 0{,}02\ c$, shown in Fig. 1.1. Surface thermograms, calculated within the considered models and shown in the same figure, practically coincide and agree well with the experiment, excluding the late cooling stage. Even if the calculations disregard the separation of components in the material at non-congruent phase transitions, i.e. the composition is assumed to be constant ($x = x_0 = const$), the resulting thermogram and calculations also have just a minor divergence with $x = var$. This testifies to a weak influence of mass transfer on the surface thermogram in the condensed phase.

Fig. 1.2 shows calculated dynamics of changes in composition x of condensed phase on the heated surface. It can be seen that a more adequate model with a two-phase zone predicts smaller variations of material stoichiometry on the surface in comparison with "Stephan model". Beside this, at the time of melting ($t = 0.03\ s$) and appearance of solid phase on the surface ($t = 0.062\ c$) stoichiometry has a small difference from the initial $x_0 = 2.17$.

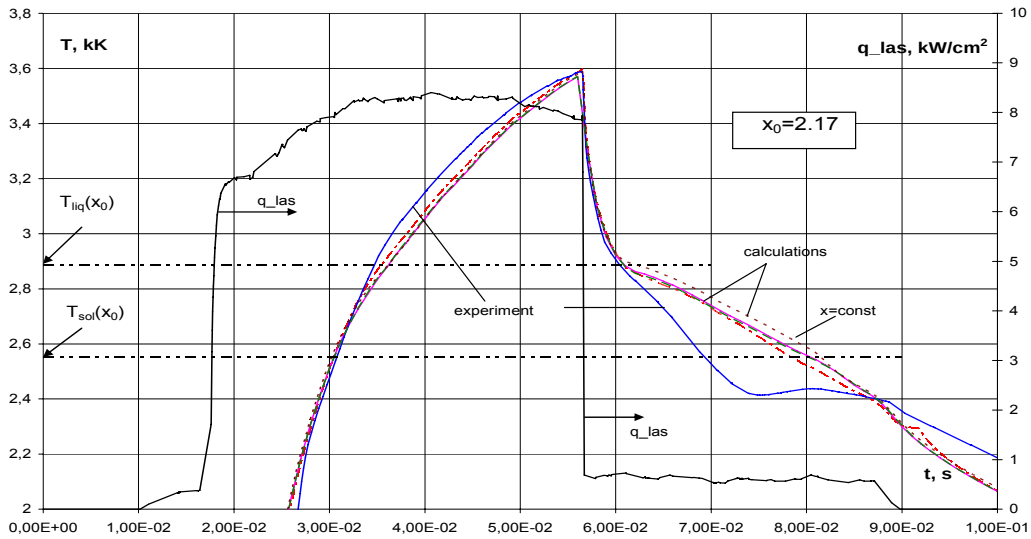

Fig. 1.1 – Thermograms of the surface

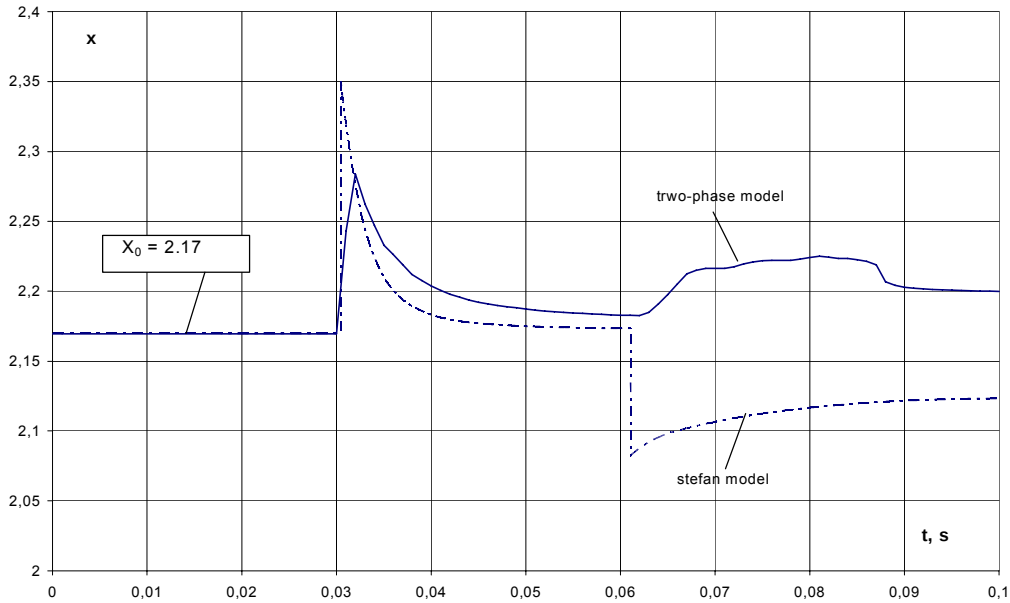

Fig. 1.2 – Calculated *x* composition dynamics of phase condensed on the heated surface

2. Development of the model for uranium oxide melting using the defect model of crystalline lattice.

The defect structure of UO_2 crystalline lattice was found and the number of defects in it was evaluated. This enabled to calculate the temperature of its melting and identify physical mechanisms determining the domain of solid phase sustainability.

Main provisions of the model:

i) Appearance-disappearance of defects in the crystalline lattice of an oxide is the result of its chemical interaction with ambient oxygen (around the crystal).

ii) Types of defects occurring in this lattice are determined by the character of experimental dependence of the crystal mass (its non-stoichiometry – x) on the partial pressure of oxygen in the ambient atmosphere at T=const.

iii) All defects occur and exist in the lattice as compact electro-neutral groups.

iv) When the number of defects located in the interstitial space of the lattice reaches its filling limit, the lattice is destructed – melts down (completely at x=0 or partially), which gives solidus boundaries.

v) If the condition of defect location for a particular lattice is violated, it leads to the separation of a phase from it; and this removes the excess of this defect from the lattice.

This approach was developed first for ZrO_2 having the same fluorite type of crystalline lattice as UO_2. This enabled to describe all essential behavior peculiarities of this oxide, also to reveal the nature of existence of so-called "low-temperature" cubic modification.

For UO_2 the general configuration of boundaries of the UO_{2-x} monophase existence region for x>0 and x<0 (Fig. 1.3) was calculated. It has a good agreement with available experimental data.

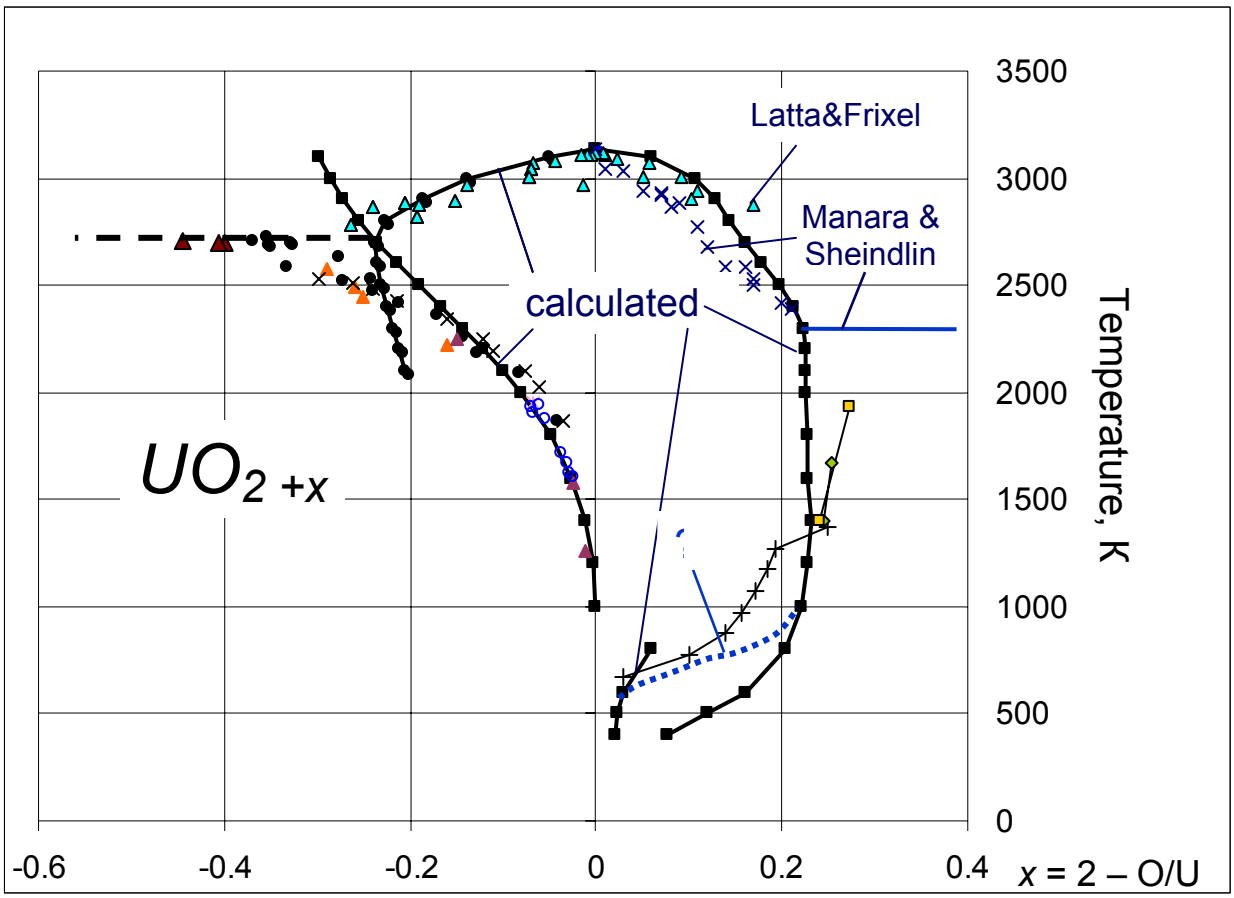

Fig. 1.3 – Boundaries of the region with monophase existence of UO_{2-x} for x>0 and x<0

Improvements of the experimental setup with laser heating

1. The attention was focused on the upgrade of experimental setup by adding up-to-date optical diagnostics instruments. Primarily it is high-speed video recording of the specimen surface (rate 1000 frame/s). After the upgrade the system can operate in two modes:

- Registration with external lighting to reduce self glow of the specimen. For that a laser was used, which is operated in pulse-periodic regime with pulse sequence frequency of 1 kHz and pulse duration of about 5 μs. The exposure time of high-speed video camera was set at the level of ≈10 μs, which provided an additional reduction of unwanted illumination by the specimen glow. By this a clear image of the heated ceramic surface in the whole measured temperature range was achieved (including the liquid state).
- Registration with self glow. Measurements were made at the wavelength of ≈ 850 nm, which, in comparison with traditional "pyrometric" wavelength of 650 nm slowed down the signal dynamics or increased the experimental temperature range. The non-linearity and inhomogeneity of sensitivity across the image field was studied. The appropriate corrections were made and the absolute calibration was performed using the temperature lamp. Temperature fields at the solidification of reference material (ZrO_2) were made.

2. A new system was made for heating semitransparent (high-reflection) ceramics by the radiation of neodymium YAG-laser operating at the wavelength of 1064 nm. In particular, such ceramics are ZrO_2 and CaO. The problem is that such materials reflect practically all incident radiation at room temperature, and their absorption coefficient increases with temperature. In this way their radiation by the subsecond laser pulse at moderate power densities (normally used in such experiments) does not heat the material. Considerable (several times) increase of power density results in the material heating, but the surface temperature grows exponentially due to the sharp dependence of absorption coefficient from temperature. It is practically impossible to control the maximum heating temperature and manage the cooling rate in this case. The established heating system provides the preliminary heatup of the specimen up to the temperature, at which the absorption capacity reaches the level sufficient for its controlled heating by the time-profiled laser pulse. The time of preliminary heatup can amount to tens and hundreds of seconds. The starting exponential temperature growth is controlled by the pyrometer. After the predetermined temperature is reached (normally in the range of 1500-2000 K depending on the material) the preliminary heating is disconnected and the programmed pulse is turned on simultaneously. This enabled to heat high-reflection ceramics of CaO, and prevent considerable superheating versus the boiling temperature at atmospheric pressure.

3. The spectropyrometer was recalibrated using the blackbody model, in the experiments with laser heating it provided a possibility of simultaneous measurement of the actual temperature on the material surface and its spectral emissivity. The applied method of polychromatic pyrometry is based on the registration of heat radiation spectrum $\Psi(\lambda,T)$ in a wide range of wave lengths (usually in the 500–900 nm range) by the quick-response spectropyrometer and subsequent computer processing of the signal using the algorithm briefly described below:

$\Psi(\lambda,T) = P(\lambda,T)\cdot\varepsilon(\lambda,T)$, where $\varepsilon(\lambda,T)$ - spectral emissivity, $P(\lambda,T) = C_1\lambda^{-5}(\exp(C_2/\lambda T)-1)^{-1}$ - blackbody radiation spectrum.

i) using different criteria, such as comparison with well-studied materials, theoretical presentation and others, the type of functional correlation is chosen for the $\varepsilon(\lambda,T)$ approximation;

ii) $\varepsilon(\lambda,T)$ is presented as a к-parametrical function λ, T: $\varepsilon = \varepsilon(\alpha_1,\alpha_2,...,\alpha_k,\lambda,T)$, starting from $k = 1$. Using recursive algorithm from the minimum functional condition $\Phi = \int|\Psi - \varepsilon P|^2 d\lambda$ all α_i parameters and T are evaluated;

iii) the accuracy of resulting approximation is analyzed; after that the program run is either stopped or k is increased by 1 and calculations continue starting from stage ii).

Efficiency of the methodology has been checked in the experiments with laser heating of ZrO_2 specimens. Fig. 1.4 shows the emissivity dynamics of the material surface and its actual (true) temperature derived from the measured spectra of self-radiation. The measured true melting temperature agrees well with publications.

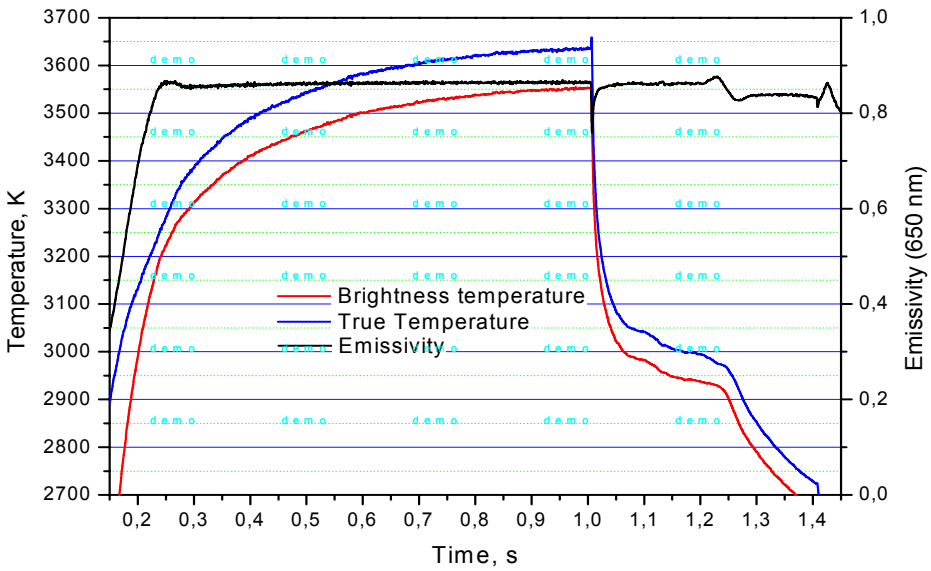

Fig. 1.4 – Temperature and emissivity dynamics

Subtask 1.2 – Experiments and analysis of produced data

As the shipment of uranium-bearing specimens manufactured by NPU "Lutsch" is postponed due to a delay in granting a license authorizing IHT RAS to handle natural uranium, the main activities were focused on the fine-tuning of experimental techniques and working with materials without uranium, which present an interest in the context of the current project.

1. Experiments on melting ZrO_2 and CaO used all measurement complex facilities, as foreseen at the stage of project development. In comparison with instruments produced in JRC, Karlsruhe, which were previously used for these experiments, the spectropyrometer speed performance increased five times in combination with unlimited spectra recordings time. The instrumentation was complemented by a high-speed camera, which registers temperature fields on the melt surface with time resolution of more than 1 ms. So, for the first time such experiments provide an opportunity to analyze peculiarities of the melting and crystallization

processes at laser heating and to correlate heating and cooling thermograms with temperature fields formation.

The attention was focused on the specification of CaO melting temperature. The complexity of these experiments is explained by the high transparency of CaO at temperatures below 2000 K, and by a relatively low boiling temperature, which is approximately 3300 K. Its melting temperature happens to be close to the boiling temperature, which, in our opinion, has led to a large scattering in the published values of CaO melting temperature. According to different authors it has a several hundred K difference.

Fig. 1.5 shows characteristic thermograms of heating at a rectangular laser pulse of 300 ms.

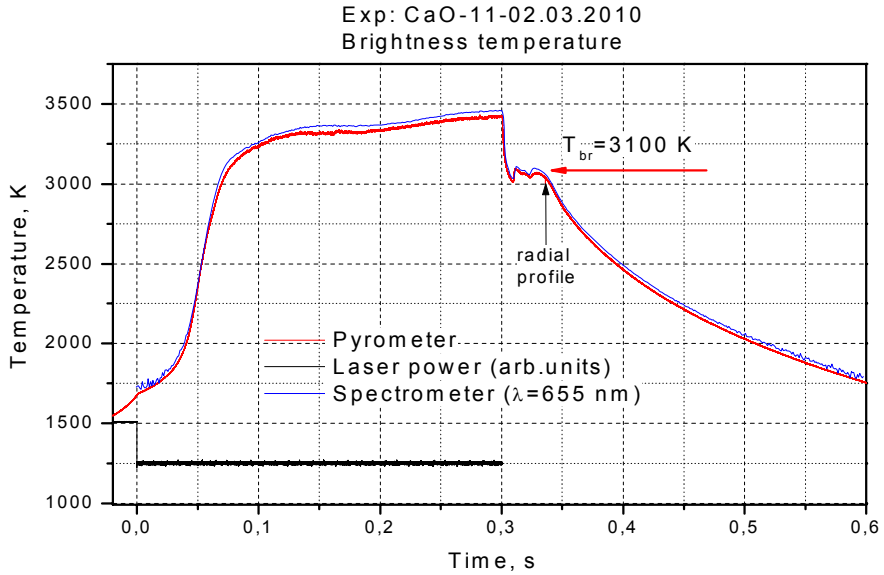

Fig. 1.5 – Characteristic heating thermograms at 300 ms rectangular laser pulse

The power was disconnected completely, which led to a high rate of cooling and, consequently, to the reduced length of crystallization site. At first sight the sharp drop of temperature below that of crystallization after the disconnection of heating radiation could be attributed to the subcooling of liquid. But a high tempo of "return" to the crystallization plateau enabled to assume that this peculiarity of the thermogram is caused by the steam condensation leading to the surface screening. The high-speed video recording confirmed the presence of characteristic convective steam flow at maximum temperatures, and further darkening of steam torch, which indicates the screening of surface by steam. Fig. 1.6 shows the radial temperature distribution at the moment when crystallization is over.

2. Technology for preparing polished sections from specimens subjected to laser impact will make possible to study structure, phase and elemental compositions of the material in the bulk of the heated zone. Three polished sections of three different compositions of the Zr–O system revealed large (up to 0.1 mm) inclusions of metallic phase, which indicates a possible stratification of the liquid melt phase into two unmixable liquids.

Video recording has shown that during heating in the central practically isothermal and originally homogeneous part of the melt regions with different brightness are formed; they change shape and position chaotically. It takes place up to the time when boiling temperature is

reached. At cooling the reverse process is observed: the merger of dark and light spots to form the visually homogeneous melt surface (cooling rate 10^4 – 10^5 K/s). The effect is likely to be explained by the melt separation into two unmixable liquids – assumably metallic and oxidic - with substantially different emissivity values. If this is confirmed by further experiments, we can talk about the existence of melt stratification region in the Zr-O system close to the boiling temperature (not to the liquidus temperature, as it is in the studied systems U-O, SiO_2-UO_2 and others.), and it does not reach liquidus temperature by 100–400 K.

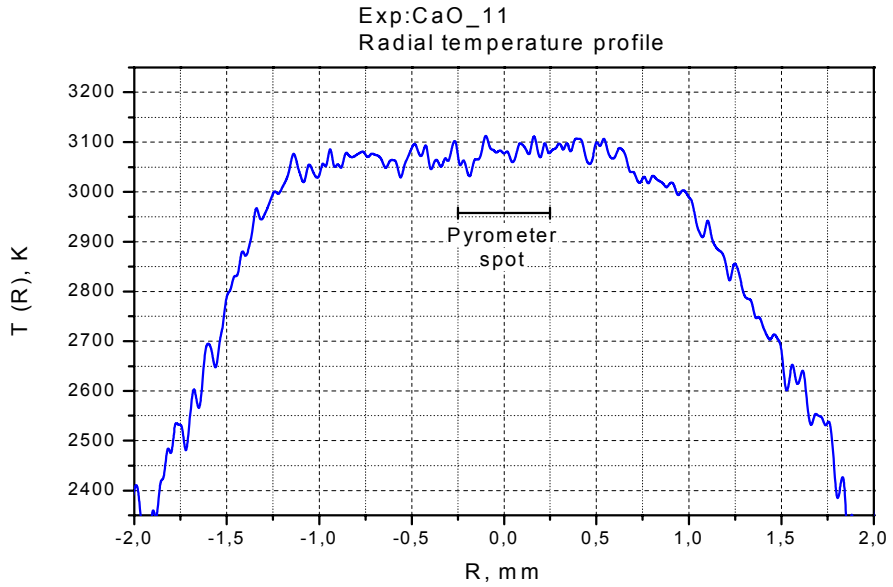

Fig. 1.6 - Radial temperature distribution at the moment of crystallization completion

3. Preliminary experiments with 3 compositions in the ZrO_2-FeO systems were made. The specimens were prepared by compacting previously mixed powders in specified proportions without thermal treatment. To homogenize the material several preliminary cycles of heating – cooling were made until the thermogram reproducibility. The measured values of liquidus and solidus temperatures (monotectics) are given in Fig. 1.7.

For compositions with Fe O<0.30 results agree well with available data. For compositions with FeO=0.54 the measured liquidus temperature was lower. Video recording has shown that melt stratification takes place in this composition. The studies will be continued.

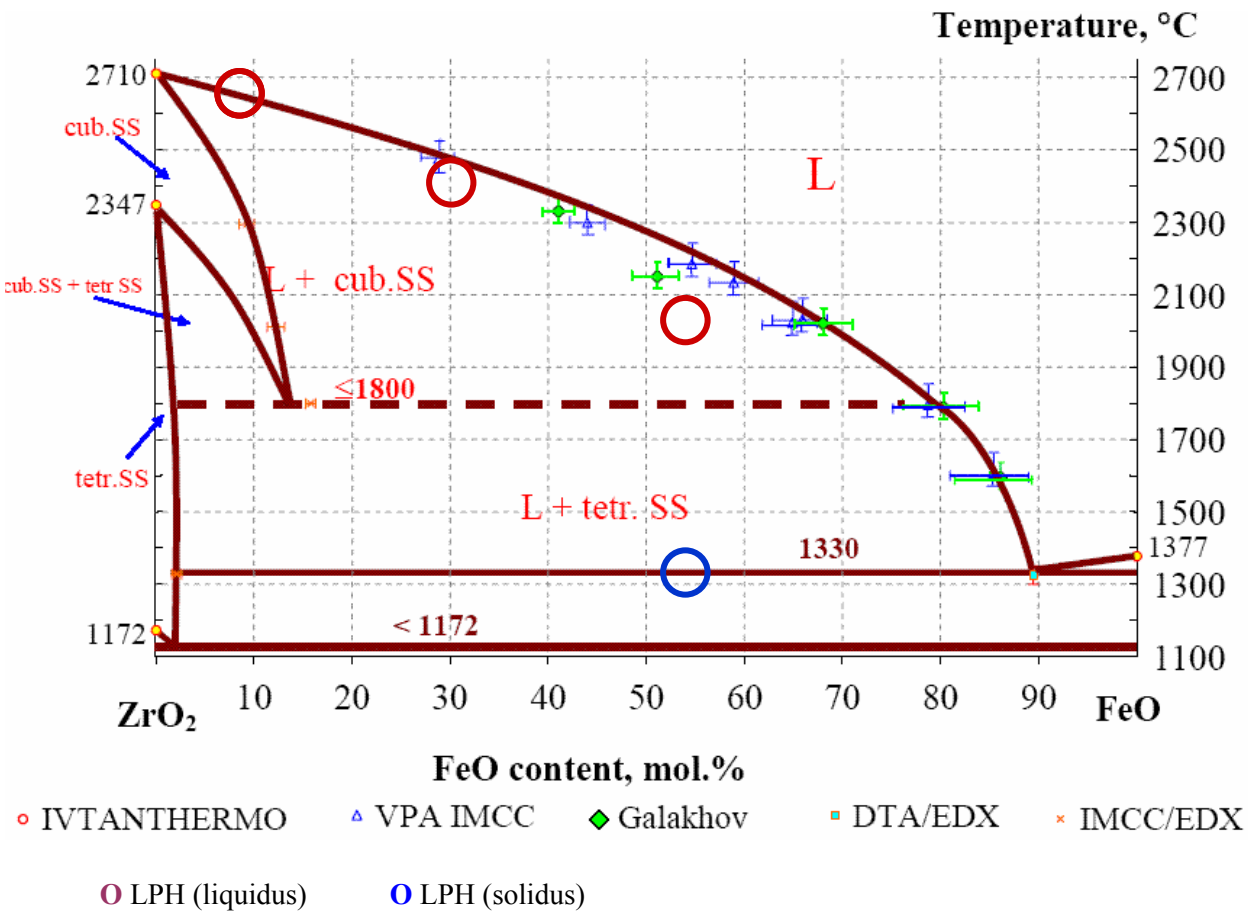

Fig. 1.7 – Measured liquidus and solidus values

The laboratory room licensing procedure, the first-priority issue in this project, has a slower than anticipated progress. The problem is explained in the explanatory note on the work progress.

By now difficulties with the licensing of laboratory for handling natural uranium have been resolved, though they seemed to be unsolvable in the beginning of the reported period. A clear action plan has been made; its implementation will result in getting the permit. The approved design of the laboratory for handling natural uranium has been sent for the final approval, the required additional construction-and-fitting work is close to completion. All these activities are funded by IHT RAS, the participating institute.

Task 2: Study of binary oxidic systems

Subtask 2.2.: Experimental investigations and analysis of produced data.

The UO_2-SiO_2 system

In the reported period the activities were in particular directed at the specification of liquidus line position in the high-temperature domain of the diagram from the UO_2 side.

To study the binary oxidic system UO_2-SiO_2 the method of VPA IMCC was used (PRS experimental series), high-temperature annealing in the Galakhov microfurnace was followed by the specimen quenching (GPRS experimental series) and SEM/EDX analysis.

Table 2.1 gives the original version of the PRS experimental matrix for the UO_2-SiO_2.

Table 2.1 - PRS experimental matrix for the UO_2-SiO_2 system

Experiment	Charge composition, mass% / mol.%	
	UO_2	SiO_2
PRS9	93.1 / 75	6.9 / 25

Small-scale experiments GPRS19-28, 32, 52-55 with melting followed by quenching of the mixture in molybdenum crucibles were conducted.

The GPRS experimental matrix for the UO_2-SiO_2 system is given in Table 2.2.

Compositions from experiments of the PRS and GPRS series cover a wide range of concentrations from 51 to 98 mass% for UO_2.

Table 2.2 - GPRS experimental matrix for the UO_2-SiO_2 system

Experiment	Charge composition, mass% / mol.%		Annealing temperature°C	Exposition, min
	UO_2	SiO_2		
GPRS19	91.3 / 70	8.7 / 30	2200	10
GPRS20	87.1 / 60	12.9 / 40		
GPRS21	81.8 / 50	18.2 / 50		
GPRS22	75.0 / 40	25.0 / 60		
GPRS23	91.3 / 70	8.7 / 30	2300	
GPRS24	87.1 / 60	12.9 / 40		
GPRS25	51.3 / 19	48.7 / 81	2175	
GPRS26	81.8 / 50	18.2 / 50	2300	
GPRS27	51.3 / 19	48.7 / 81	2160	
GPRS28	75.0 / 40	25.0 / 60	2300	
GPRS32	51.3 / 19	48.7 / 81	2130	
GPRS52*	87.1 / 60	12.9 / 40	2300	
GPRS53*	84.6 / 55	15.4 / 45	2300	
GPRS54*	55.9 / 22	44.1 / 78	2200	
			2140	
GPRS55*	98.8 / 95	1.2 / 5	2000	
			2000-1700	240

*- polished sections are in preparation for SEM-EDX.

Compositions from experiments of the PRS and GPRS series cover a wide range of concentrations from 51 to 98 mass% for UO_2.

- **Experiment PRS9**

Experiment PRS9 was made on the Rasplav 4 tests facility. Fig. 2.1 shows the furnace schematics.

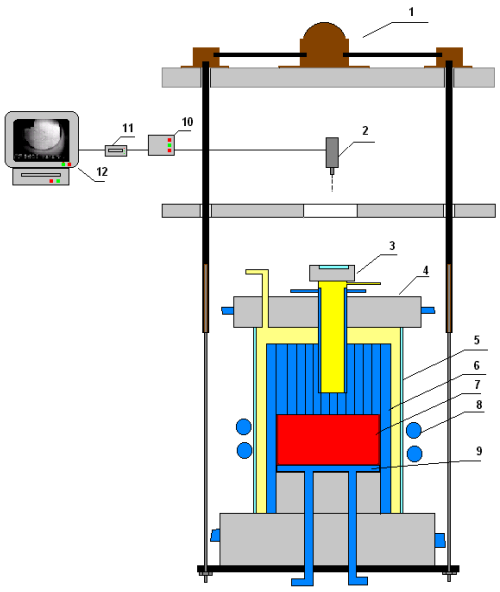

1 – driver for vertical shift if the crucible 2 – pyrometer combined with video camera;
3 – pyrometer shaft; 4– water-cooled cover; 5 – quartz tube; 6 – crucible sections; 7 - melt;
8 - inductor; 9 – bottom calorimeter; 10 – data acquisition system; 11 – device for inserting measured data into video frames; 12 – monitor/video recorder.

Fig. 2.1 – Schematics of "Rasplav-4" test facility

Table 2.3 shows the PRS9 experimental procedure

Table 2.3 –PRS9 experimental procedure

Time from the experiment start, s	Stage/event
0-1003	Startup heating , molten pool formation with charge addition. Crust having 2000C temperature is on the pool surface.
1004-1035	The shaft is lifted and lowered, observation port in the shaft is replaced
1264-1276	Pool depth and bottom crust thickness are measured; they are 45 and 2 mm respectively.
1326-1341	VPA IMCC # 1
1532-1591	1st melt sample is taken
1797-1825	VPA IMCC # 2
1940-1985	2nd melt sample is taken
2059-2070	VPA IMCC # 3
2166-2212	3rd melt sample is taken
2220-2287	The shaft is lifted and lowered, observation port in the shaft is replaced
2296	HF heating is disconnected. Ingot is crystallized in argon and frozen

Pyrometer readings (Tm), and changes of voltage (Ua), plate current (Ia), heat sink into the crucible (Q_{ccr}) versus time are given in Fig. 2.3. Figs. 2.4 – 2.6 show fragments of thermograms during VPA IMCC.

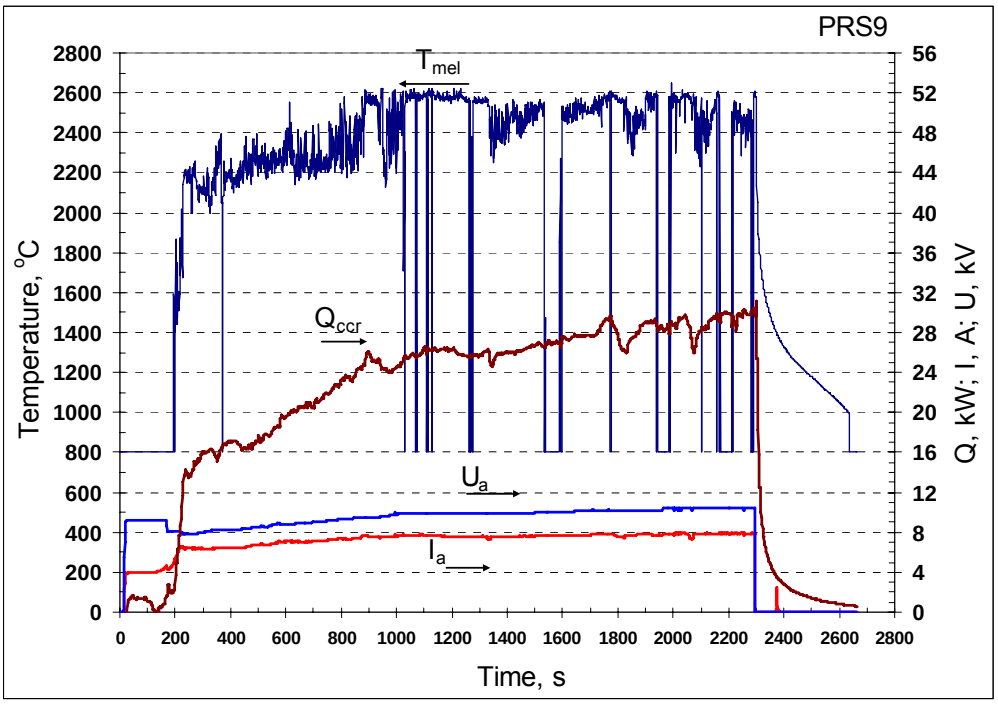

Fig. 2.3- PRS9 voltage (U_a), plate current (I_a), heat sink into crucible (Q_{ccr}) and melt surface temperature (T_{melt}) versus time

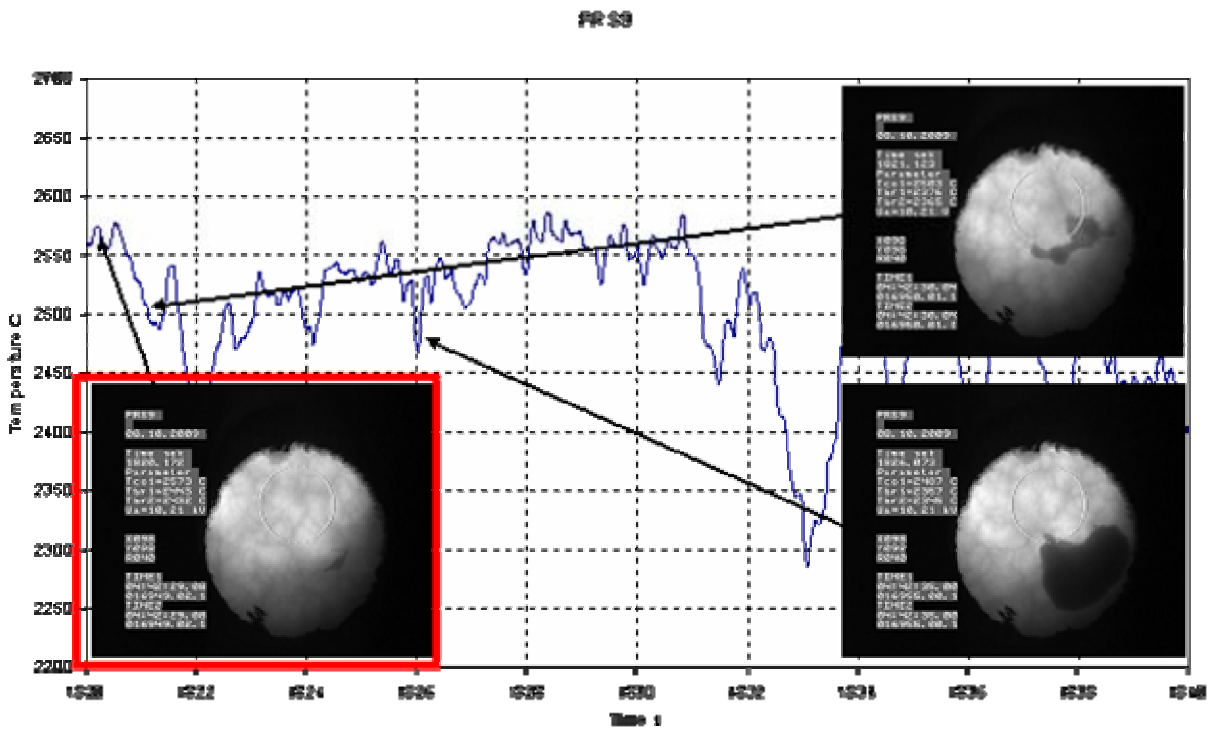

Fig. 2.4 PRS9 thermogram fragment during VPA IMCC # 1

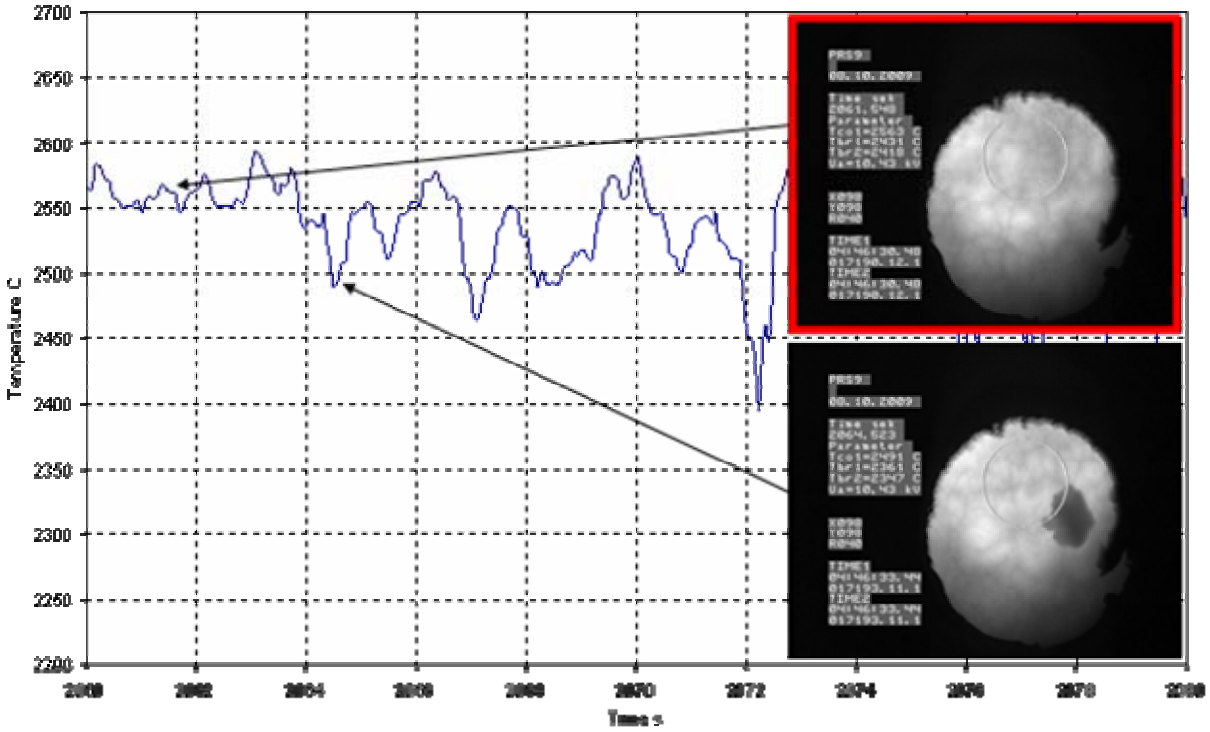

Fig. 2.5- PRS9 thermogram fragment during VPA IMCC # 2

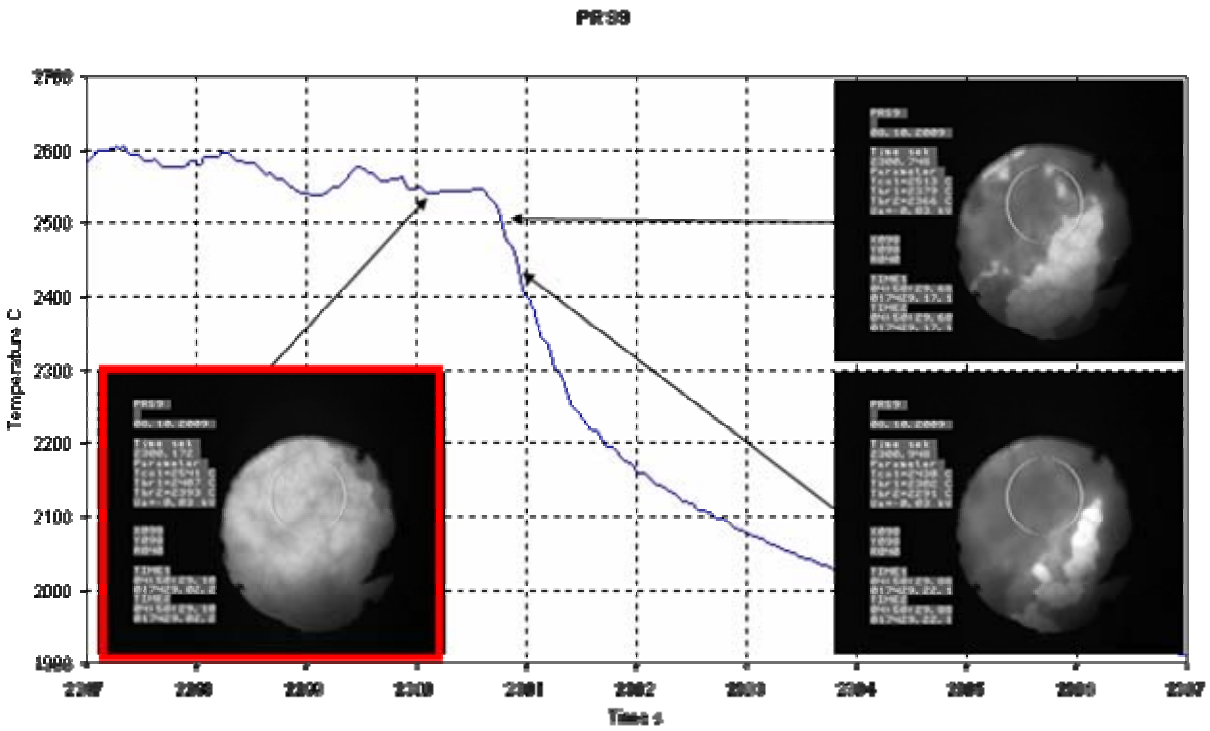

Fig. 2.6- PRS9 thermogram fragment after inductor voltage is disconnected

Liquidus temperatures measured in this experiment were 2573, 2563, 2541°C, respectively averaged T_{liq}=2559±38°C

When furnace was disassembled after PRS9 experiment aerosol deposits were found on its sections. The crust was approximately 1-2 mm, which shows that during the experiment all charge was molten.

After the experiment the ingot was taken out, weighed and included into the epoxy resin. A polished section for the SEM/EDX analysis was cut from ½ part of axial cross section, its second part was used to prepare the average sample for the physicochemical analysis. Fig. 2.7 shows the cross section of PRS9 ingot.

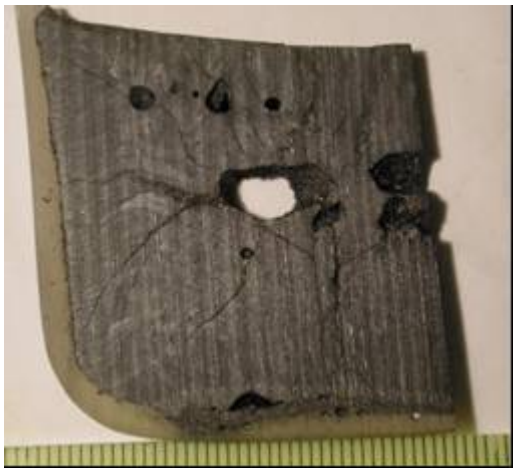

Fig. 2.7- Ingot axial section

Mass balance of Experiment PRS9 is given in Table 2.4.

Table 2.4- PRS9 mass balance

Introduced into the crucible, g		**Collected, g**	
UO_2	1456.44	**Ingot**	1272.20
SiO_2	105.08	**Samples**	21.01
U	10.00	**Probe sample**	5.00
		Aerosols	169.79
		Above-melt crust	71.38
		Spillages [1)]	29.11
Σ	**1571.52**	**Σ**	**1568.49**
Imbalance	**-3.03**		

Note:

[1)] Spillages – unreacted charge and aerosols spilled from sections at the crucible disassembly.

Molten products of experiment PRS9 were used to prepare specimens for chemical analysis. At first they were crushed to the particle size of < 1.0 mm, after that quartered to the particle size ≤ 50 µm. The resulting specimens were analyzed for the content of $U_{total.}$ All samples for analysis were prepared in the argon atmosphere.

Aerosol samples were prepared in the following way: samples of 0.1-0.5 g were molten with (3.0±0.5) g of potassium pyrosulphate at (900±25) ºC until transparent fusion cake was made, after that it was dissolved at heating in 200-250 ml of 1M sulphuric acid solution, after that U_{total} was determined by photometry with reagent arsenazo III [2,3].

Other samples were analyzed using the following methodology: the crushed portion of corium (0.1 g mass) was dissolved in a mixture of concentrated orthophosphoric and sulphuric acids (1:2) in the argon flow, after that U_{total} was determined in the solution by photometry with arsenzo III.
Table 2.5 shows the chemical analysis data and elemental material balance of PRS9 experiment recalculated for oxides.

Table 2.5 – Chemical analysis data of PRS9 molten products

Item	Content, mass %/mol.%		Mass of samples, g	Mass, g	
	UO_2	SiO_2		UO_2	SiO_2
Sample #1	94.16	5.84	6.32	5.95	0.37
Sample #2	93.68	6.32	7.73	7.24	0.49
Sample #3	93.76	6.24	6.96	6.52	0.43
Probe sample	95.53	4.47	5.00	4.78	0.22
Average ingot sample	97.80	2.20	1272.20	1244.17	28.03
Above-melt crust	91.44	8.56	71.38	65.27	6.11
Spillages [1)]	95.72	4.28	32.14	30.77	1.38
Aerosols from LAF	59.91	40.09	36.16	21.67	14.50
Aerosols from transport line	63.74	36.26	133.63	85.17	48.46
Collected, g				**1471.54**	**99.98**
Introduced, g				**1467.78**	**105.08**
Imbalance				**+3.75**	**-5.10**

[1)] Spillages – unreacted charge and aerosols spilled from sections when the crucible was disassembled.

SEM/EDX analysis from Experiment PRS9 are given in figures 2.8– 2.16 and tables 2.6-2.13.

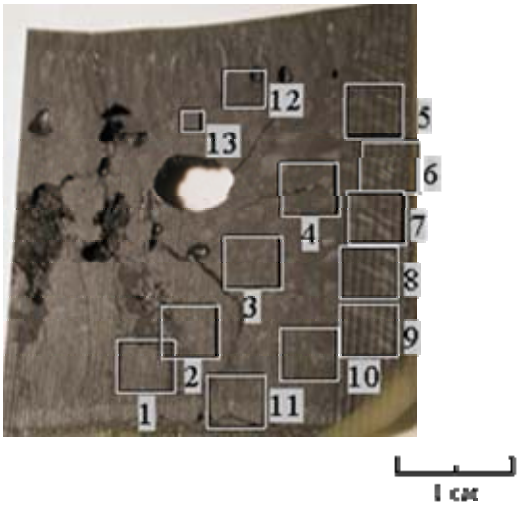

Fig. 2.8 - SEM of the PRS9 ingot section with locations chosen for SEM/EDX analysis

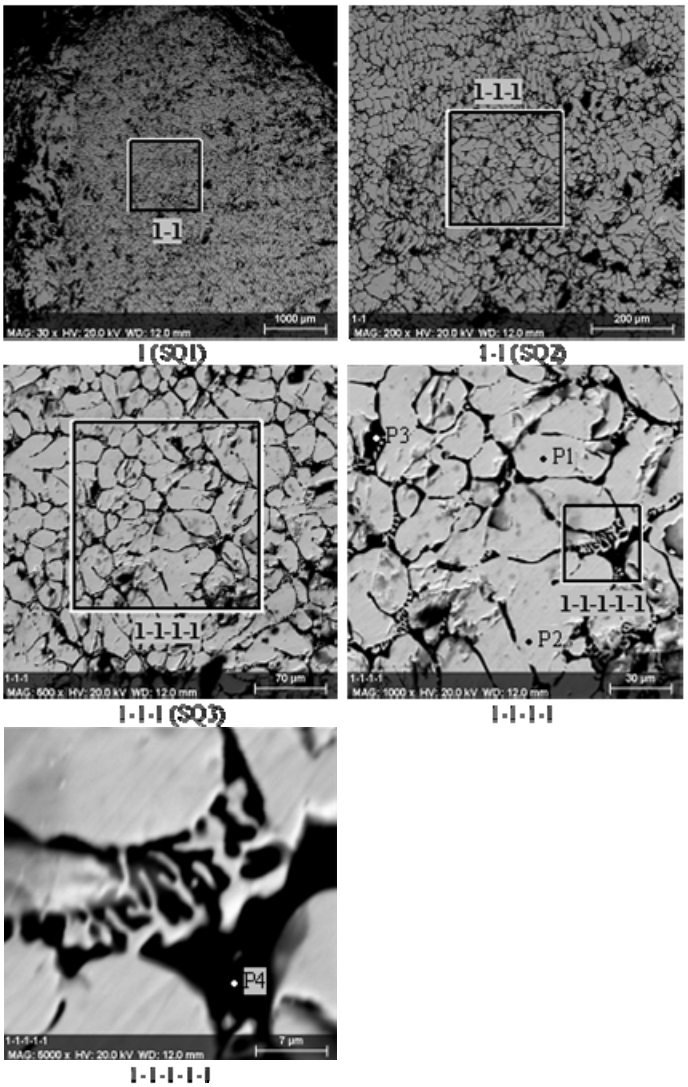

Fig. 2.9 - Microphotographs of region 1

Table 2.6- EDX data for Region 1

#		U	Si	O	UO_2	SiO_2
SQ1	mass%	80.3	3.9	15.8	91.6	8.4
	mol.%	23.0	9.5	67.5	70.8	29.2
SQ2	mass%	79.5	3.7	16.7	91.9	8.1
	mol.%	22.1	8.8	69.1	71.5	28.5
SQ3	mass%	79.7	3.9	16.4	91.5	8.5
	mol.%	22.4	9.3	68.3	70.7	29.3
P1	mass%	86.9	0.2	12.9	99.5	0.5
	mol.%	31.0	0.7	68.3	97.8	2.2
P2	mass%	87.5	0.2	12.3	99.6	0.4
	mol.%	32.2	0.5	67.3	98.4	1.6
P3	mass%	17.5	45.9	36.6	16.8	83.2
	mol.%	1.8	40.9	57.3	4.3	95.7
P4	mass%	21.2	44.9	33.9	20.1	79.9
	mol.%	2.3	42.0	55.7	5.3	94.7

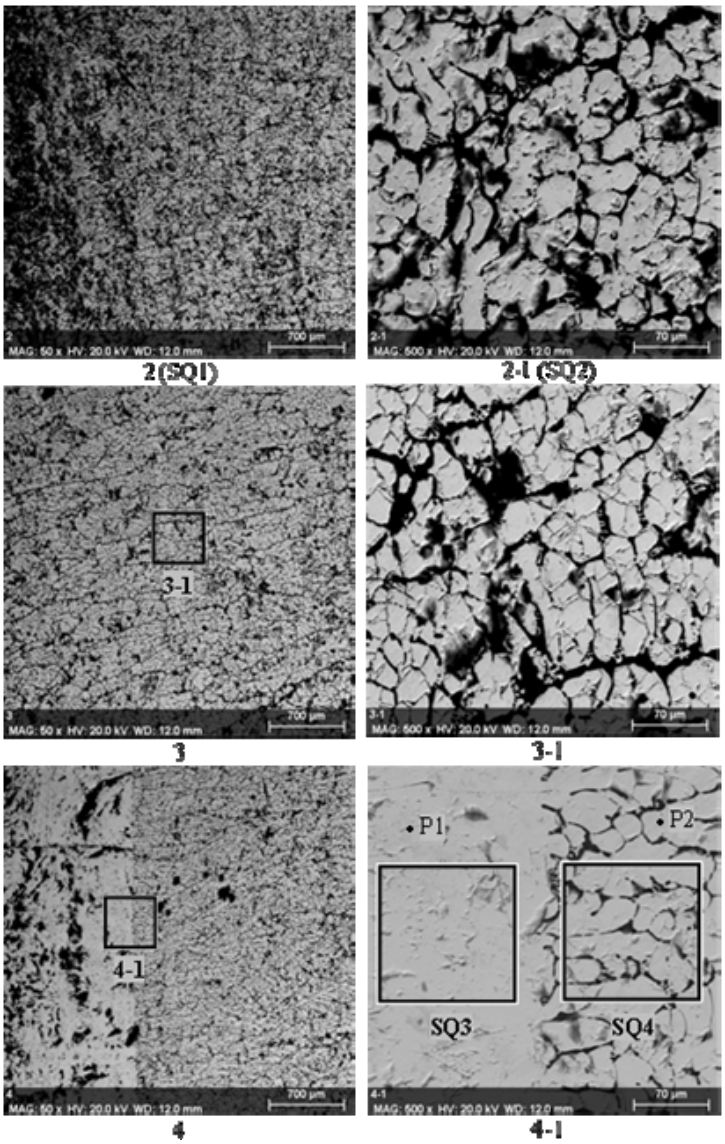

Fig. 2.10- Microphotographs of regions 2-4

Table 2.7 - EDX data for regions 2-4

#		U	Si	O	UO_2	SiO_2
SQ1	mass%	77.4	5.3	17.4	88.6	11.4
	mol.%	20.3	11.8	67.9	63.3	36.7
SQ2	mass%	78.4	4.9	16.8	89.5	10.5
	mol.%	21.2	11.2	67.6	65.5	34.5
SQ3	mass%	83.8	0.7	15.4	98.4	1.6
	mol.%	26.2	1.9	71.8	93.1	6.9
SQ4	mass%	80.1	3.5	16.4	92.4	7.6
	mol.%	22.7	8.3	69.0	73.1	26.9
P1	mass%	85.9	0.4	13.8	99.2	0.8
	mol.%	29.2	1.1	69.7	96.4	3.6
P2	mass%	87.2	0.3	12.5	99.4	0.6
	mol.%	31.6	0.9	67.5	97.2	2.8

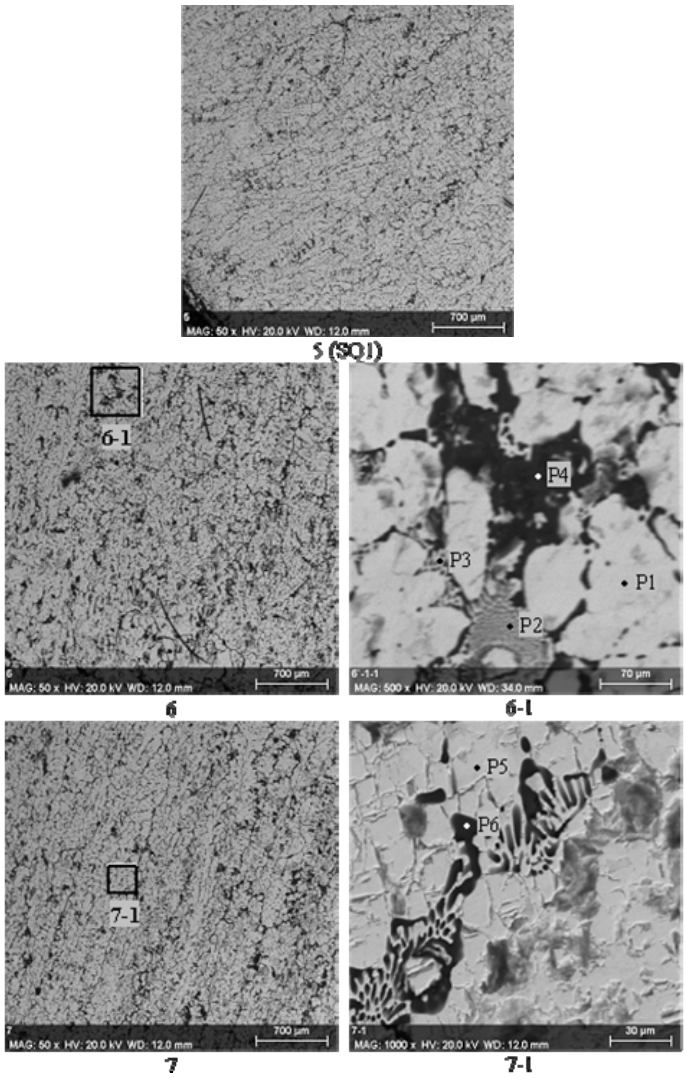

Fig. 2.11- Microphotographs of regions 5-7

Table 2.8 - EDX data for regions 5-7

#		U	Si	O	UO_2	SiO_2
SQ1	mass%	77.4	4.9	17.7	89.3	10.7
	mol.%	20.2	10.8	68.9	65.1	34.9
P1	mass%	87.0	0.3	12.7	99.3	0.7
	mol.%	31.2	1.0	67.8	97.1	2.9
P2	mass%	65.6	10.6	23.8	76.6	23.4
	mol.%	12.9	17.7	69.4	42.2	57.8
P3	mass%	66.7	9.5	23.8	78.8	21.2
	mol.%	13.3	16.1	70.5	45.2	54.8
P4	mass%	17.4	58.7	23.8	13.6	86.4
	mol.%	2.0	57.2	40.8	3.4	96.6
P5	mass%	88.4	0.2	11.4	99.5	0.5
	mol.%	34.0	0.7	65.3	97.8	2.2
P6	mass%	10.9	46.1	43.0	11.2	88.8
	mol.%	1.1	37.5	61.4	2.7	97.3

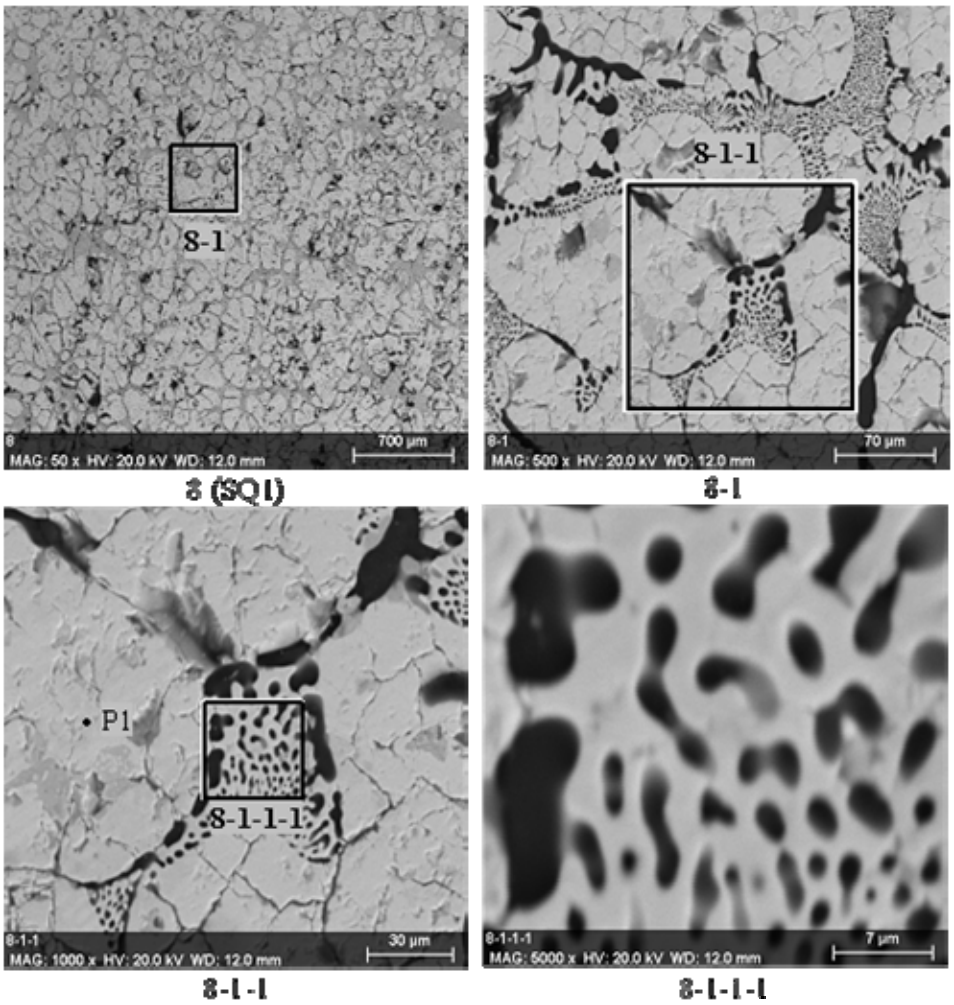

Fig. 2.12 - Microphotographs of region 8

Table 2.9- EDX data of region 8

#		U	Si	O	UO_2	SiO_2
SQ1	mass%	77.2	5.2	17.6	88.7	11.3
	mol.%	20.1	11.5	68.4	63.7	36.3
P1	mass%	85.3	0.2	14.5	99.6	0.4
	mol.%	28.2	0.5	71.3	98.4	1.6

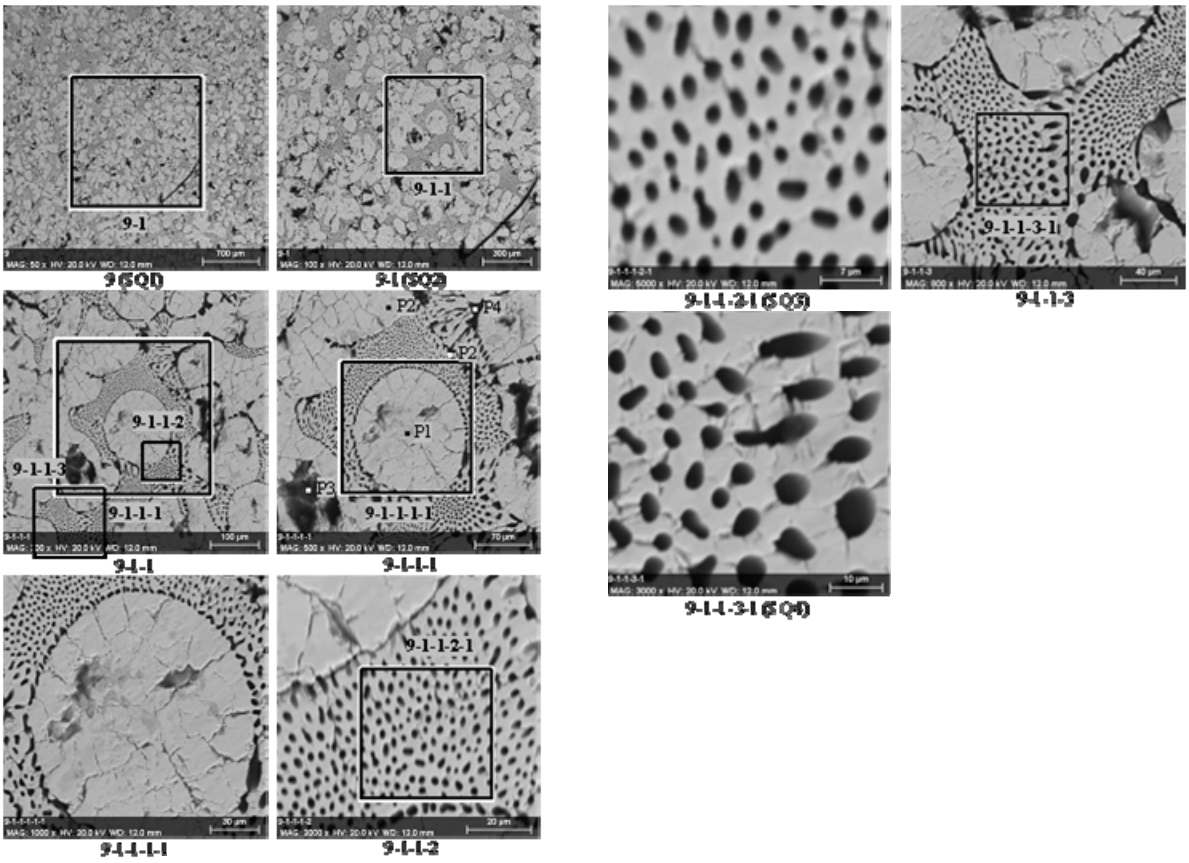

Fig. 2.13 - Microphotographs of region 9

Table 2.10 - EDX data for region 9

#		U	Si	O	UO_2	SiO_2
SQ1	mass%	78.9	4.1	17.0	91.1	8.9
	mol.%	21.5	9.5	69.0	69.4	30.6
SQ2	mass%	79.2	4.0	16.8	91.4	8.6
	mol.%	21.8	9.3	68.9	70.2	29.8
SQ3	mass%	76.2	5.4	18.4	88.1	11.9
	mol.%	19.3	11.6	69.1	62.3	37.7
SQ4	mass%	76.4	5.2	18.4	88.7	11.3
	mol.%	19.4	11.1	69.5	63.5	36.5
P1	mass%	86.0	0.3	13.7	99.3	0.7
	mol.%	29.4	1.0	69.6	96.8	3.2
P2	mass%	87.1	0.3	12.5	99.3	0.7
	mol.%	31.5	1.1	67.4	96.7	3.3
P3	mass%	30.9	35.9	33.2	31.3	68.7
	mol.%	3.7	36.7	59.6	9.2	90.8
P4	mass%	37.0	37.9	25.1	34.1	65.9
	mol.%	5.0	43.9	51.0	10.3	89.7

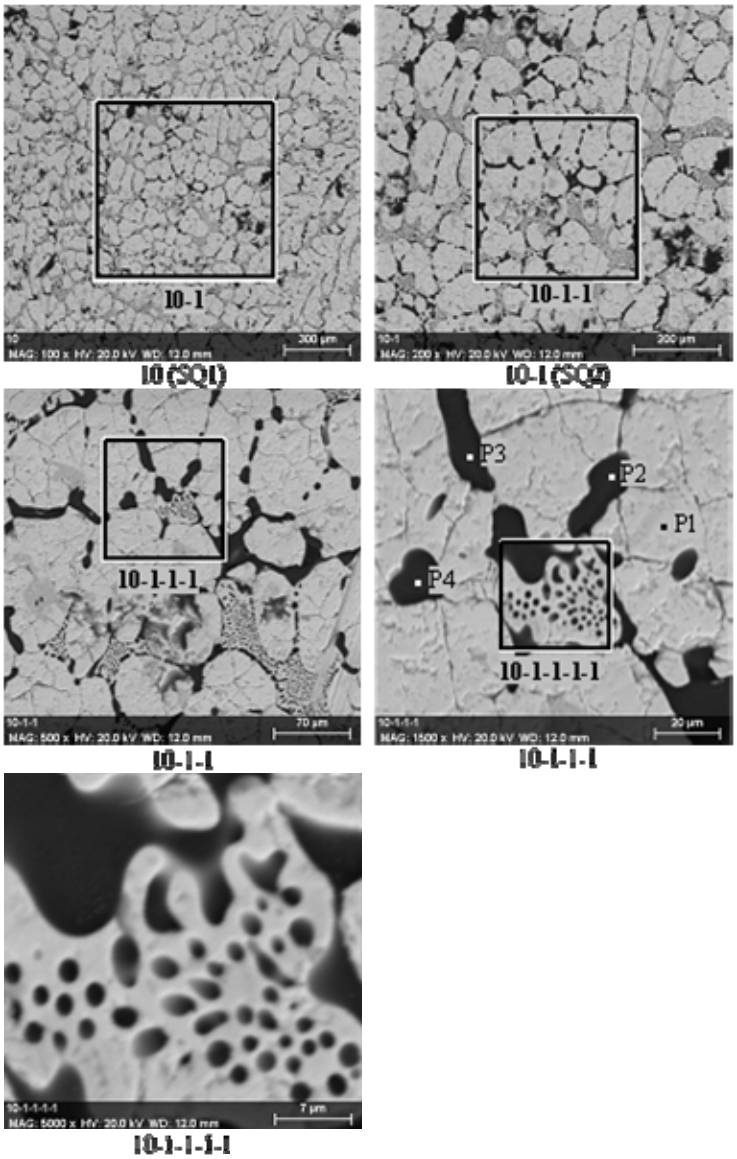

Fig. 2.14- Microphotographs of region 10

Table 2.11 - EDX data for region 10

#		U	Si	O	UO_2	SiO_2
SQ1	mass%	78.4	6.3	15.3	86.8	13.2
	mol.%	21.8	15.0	63.2	59.3	40.7
SQ2	mass%	79.7	5.6	14.8	88.3	11.7
	mol.%	23.0	13.6	63.4	62.8	37.2
P1	mass%	89.2	0.2	10.6	99.7	0.3
	mol.%	35.9	0.6	63.5	98.5	1.5
P2	mass%	11.3	45.5	43.2	11.7	88.3
	mol.%	1.1	37.1	61.9	2.9	97.1
P3	mass%	12.5	49.0	38.5	11.9	88.1
	mol.%	1.3	41.5	57.2	2.9	97.1
P4	mass%	8.9	48.9	42.2	8.8	91.2
	mol.%	0.9	39.5	59.7	2.1	97.9

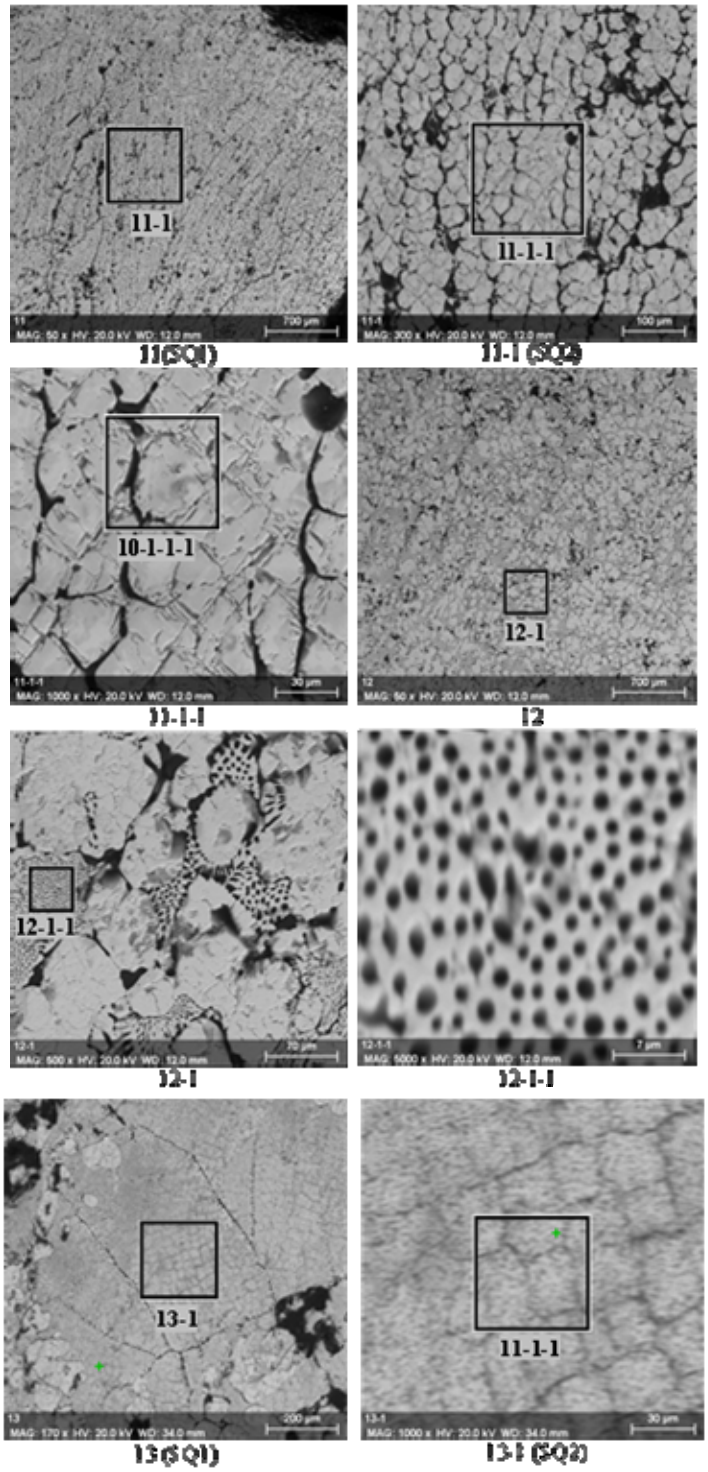

Fig. 2.15- Microphotographs of regions 11, 12 and 13

Table 2.12 - EDX data for region 13

#		U	Si	O	UO_2	SiO_2
SQ1	mass%	80.2	3.7	16.1	92.0	8.0
	mol.%	22.8	8.9	68.3	72.0	28.0
SQ2	mass%	80.2	3.9	15.9	91.6	8.4
	mol.%	23.0	9.5	67.6	70.8	29.2

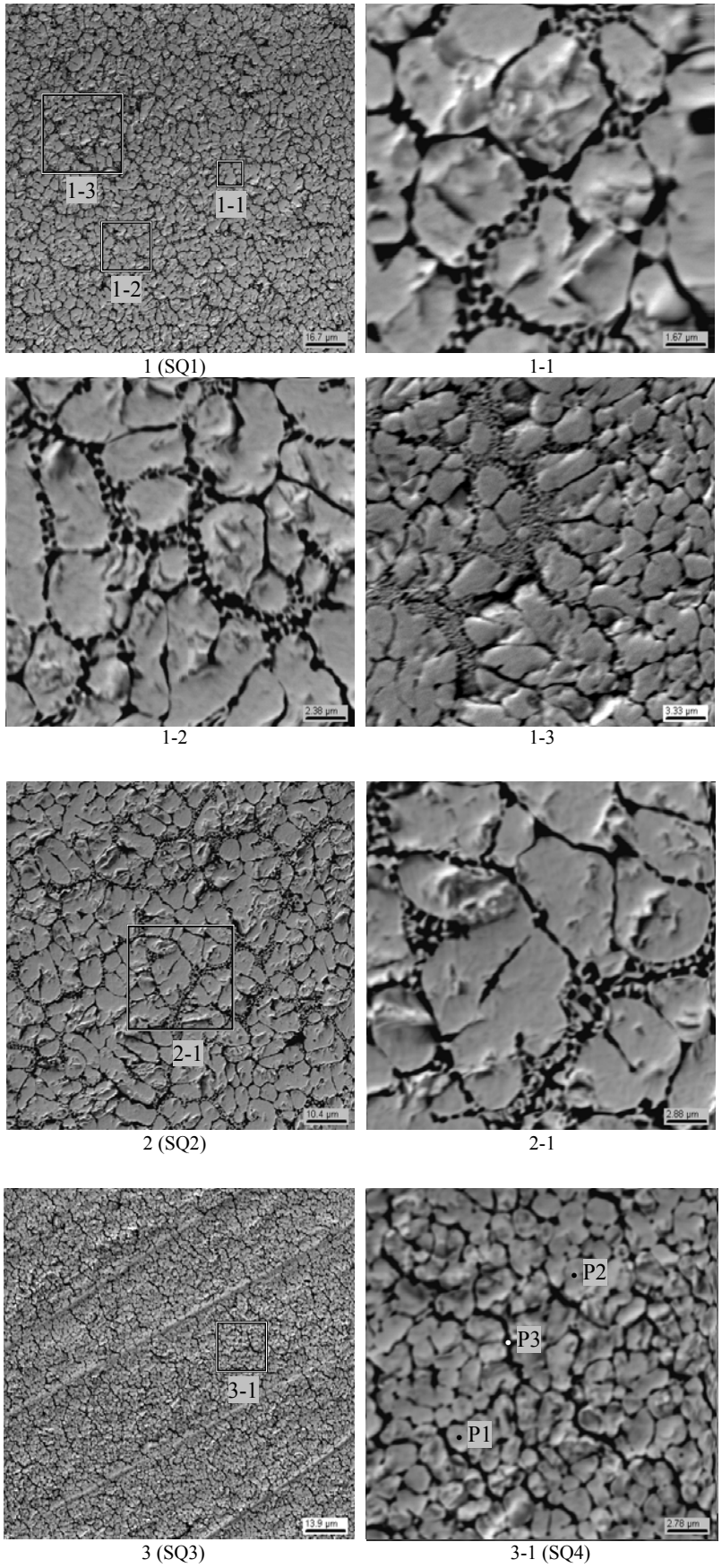

1 (SQ1) 1-1

1-2 1-3

2 (SQ2) 2-1

3 (SQ3) 3-1 (SQ4)

Fig. 2.16- Microphotographs of samples 1-3

Table 2.13- EDX data for samples 1-3

#		UO_2	SiO_2
SQ1	mass%	93.4	6.6
	mol.%	75.8	24.2
SQ2	mass%	95.0	5.0
	mol.%	80.8	19.2
SQ3	mass%	95.5	4.5
	mol.%	82.5	17.5
SQ4	mass%	95.6	4.4
	mol.%	83.0	17.0
P1	mass%	95.7	4.3
	mol.%	83.3	16.7
P2	mass%	95.8	4.2
	mol.%	83.5	16.5
P3	mass%	93.1	6.9
	mol.%	75.0	25.0

- **Experiments GPRS19-28, 32, 52-55**

Experiments GPRS were performed using the tailor-made experimental setup – Galakhov microfurnace [1] designed and built in the Grebenschikov Institute of Silicate Chemistry, Russian Academy of Sciences (ISCh RAS) and adjusted in the Alexandrov Research Institute of Technology (NITI) (Fig. 2.17).

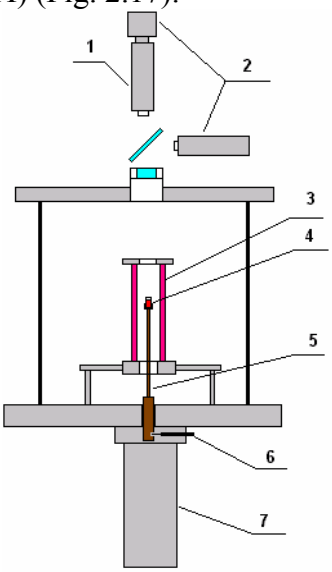

1 –pyrometer; 2- video cameras; 3 -W – tubular heater; 4 – molybdenum crucible; 5- molybdenum specimen holder; 6- electromagnetic lock; 7 – specimen quenching chamber.

Fig. 2.17 – Adjusted Galakhov mirofurnace

All GPRS experimental procedures were similar and included:

- Weighing of empty crucible.
- Layer-by-layer filling of crucible with compacting of each layer.
- Weighing of crucible with charge.

- Crucible installation into the Galakhov microfurnace,
- Degassing of furnace internal space and filling it with argon-hydrogen mixture (Ar+4.2 vol % H_2) at 3 atm. pressure.
- Heating at 1200 °C during 5 minutes.
- Stepwise heating to the specified temperature.
- Specimen exposition for 10 min (followed by its slow cooling from 2000 to 1700° C during 240 min only in GPRS55), after which it was dropped into the quenching chamber.
- Crucible is taken from the chamber after cooling, cut along the axis, a polished section is prepared for SEM/EDX analysis.

SEM/EDX analysis of experiments GPRS19-28, 32 is presented in figures 2.18– 2.38 and tables 2.14-2.28.

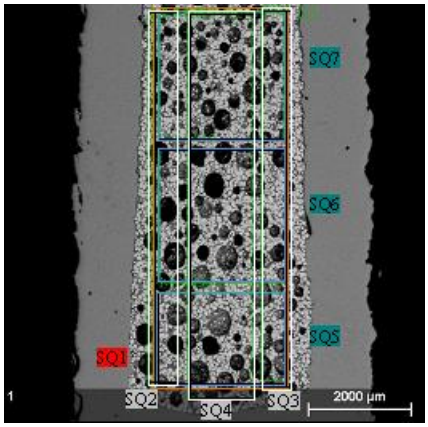

Fig. 2.18- Microphotograph of the GPRS-19 polished axial crucible section with locations chosen for SEM/EDX studies (70.0 mol.% UO_2 in charge, 2200 °C, 10 min exposition, crucible with cover)

Table 2.14 - EDX data of the average composition of the GPRS-19 crucible section (without molybdenum)

#		U	Si	O	UO_2	SiO_2
GPRS-19	mass%	67.9	7.9	24.2	82.0	18.0
	mol.%	13.7	13.5	72.8	50.4	49.6
SQ1	mass%	68.7	7.5	23.8	82.9	17.1
	mol.%	14.1	13.1	72.8	51.9	48.1
SQ2	mass%	65.7	8.7	25.6	80.0	20.0
	mol.%	12.6	14.2	73.1	47.1	52.9
SQ3	mass%	67.5	8.8	23.7	80.3	19.7
	mol.%	13.6	15.1	71.3	47.5	52.5
SQ4	mass%	67.8	7.8	24.5	82.2	17.8
	mol.%	13.6	13.2	73.1	50.7	49.3
SQ5	mass%	69.7	7.9	22.4	82.3	17.7
	mol.%	14.8	14.3	70.9	50.9	49.1
SQ6	mass%	66.1	8.6	25.3	80.4	19.6
	mol.%	12.8	14.1	73.1	47.7	52.3
SQ7	mass%	72.8	8.2	19.0	82.5	17.5
	mol.%	17.1	16.4	66.5	51.1	48.9

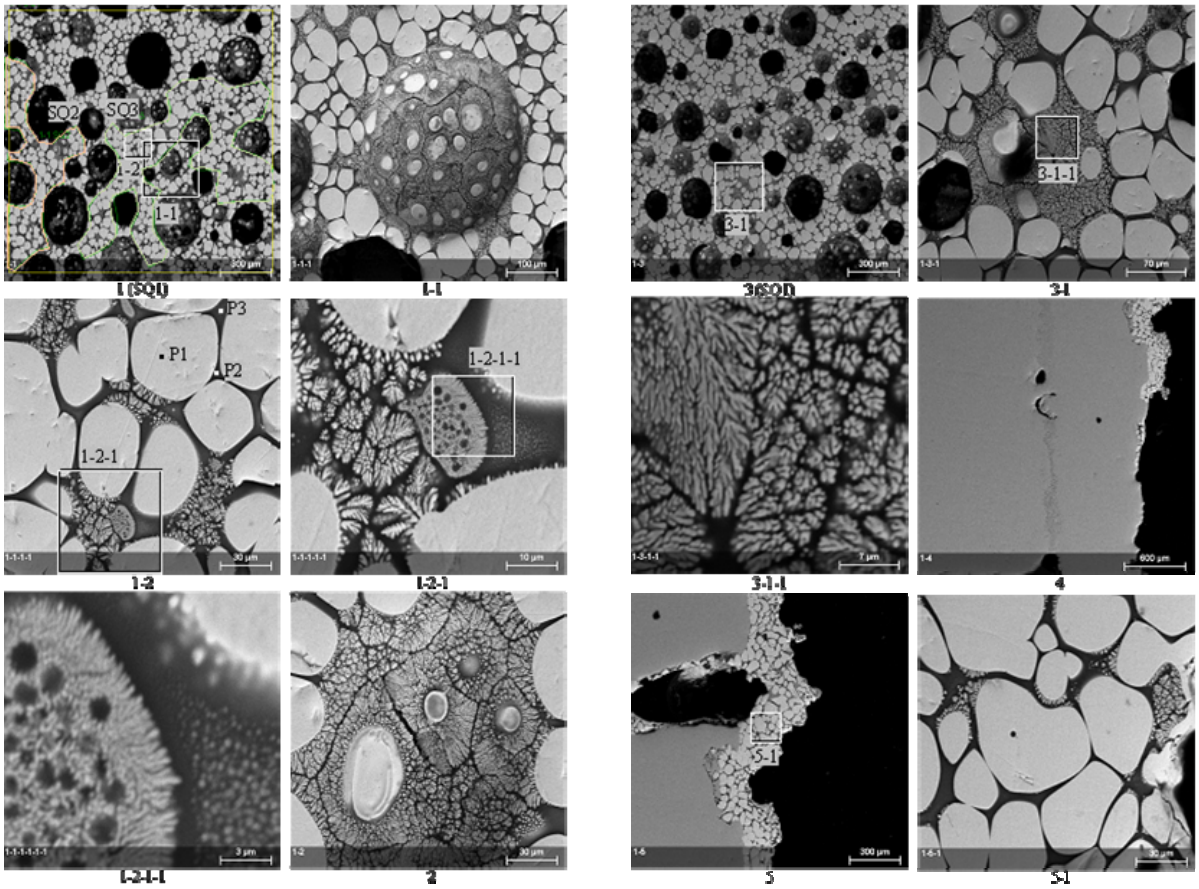

Fig. 2.19 – Microphotographs of studied GPRS-19crucible regions

Table 2.15- EDX data of studied GPRS-19 regions

#		U	Si	O	UO_2	SiO_2
SQ1	mass%	66.9	8.1	25.0	81.5	18.5
	mol.%	13.2	13.5	73.4	49.5	50.5
SQ2	mass%	70.2	7.5	22.3	83.3	16.7
	mol.%	15.1	13.6	71.3	52.6	47.4
SQ3	mass%	67.1	8.5	24.4	80.7	19.3
	mol.%	13.4	14.3	72.3	48.3	51.7
P1	mass%	88.2	0.3	11.5	99.5	0.5
	mol.%	33.7	0.8	65.5	97.6	2.4
P2	mass%	23.2	32.2	44.7	27.6	72.4
	mol.%	2.4	28.4	69.2	7.8	92.2
P3	mass%	61.5	13.1	25.4	71.3	28.7
	mol.%	11.2	20.2	68.6	35.6	64.4

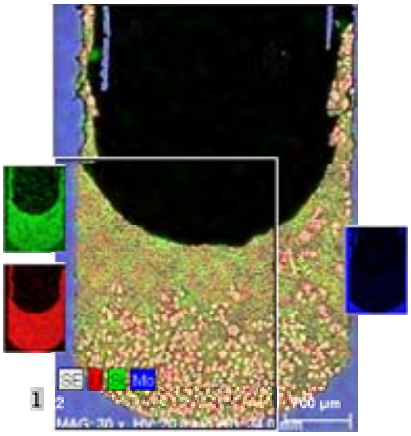

Fig. 2.20 – X-ray mapping of the GPRS-20 axial crucible section with locations chosen for SEM/EDX studies (60.0 mol.% UO_2, 2200 °C, 10 min exposition, crucible with cover)

Table 2.16- EDX data of the average composition of the GPRS-20 crucible section (without molybdenum)

#		U	Si	O	UO_2	SiO_2
GPRS-20	mass%	71.7	7.7	20.7	83.2	16.8
	mol.%	16.2	14.6	69.2	52.5	47.5

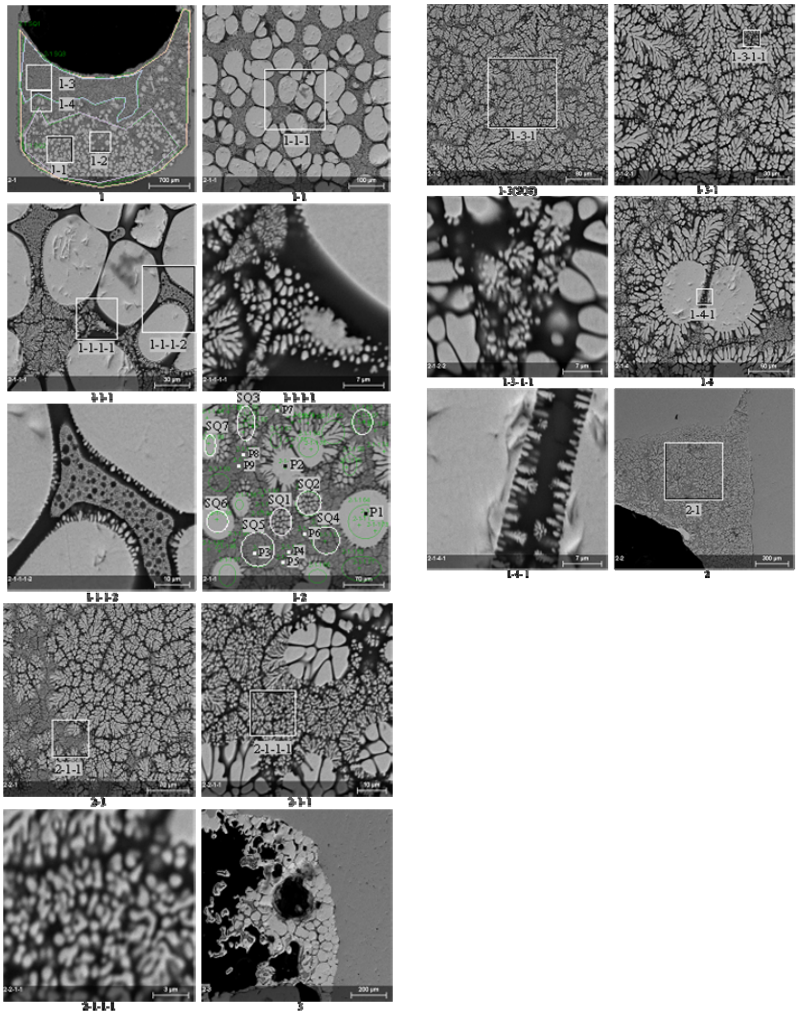

Fig. 2.21 - Microphotographs of crucible regions studied in GPRS20

Table 2.17 - EDX data of crucible regions studied in GPRS20

#		U	Si	O	UO_2	SiO_2
SQ1	mass%	64.9	10.9	24.3	76.0	24.0
	mol.%	12.5	17.8	69.7	41.4	58.6
SQ2	mass%	64.7	10.1	25.2	77.3	22.7
	mol.%	12.3	16.3	71.4	43.1	56.9
SQ3	mass%	62.1	11.2	26.6	74.6	25.4
	mol.%	11.2	17.2	71.5	39.5	60.5
SQ4	mass%	60.7	12.2	27.1	72.4	27.6
	mol.%	10.7	18.3	71.0	36.9	63.1
SQ5	mass%	59.1	14.3	26.6	68.6	31.4
	mol.%	10.3	21.1	68.6	32.8	67.2
SQ6	mass%	82.9	2.5	14.6	94.7	5.3
	mol.%	25.8	6.6	67.6	79.8	20.2
SQ7	mass%	82.7	1.7	15.5	96.2	3.8
	mol.%	25.2	4.5	70.3	84.9	15.1
SQ8	mass%	63.6	10.7	25.7	75.9	24.1
	mol.%	11.9	16.9	71.3	41.3	58.7
P1	mass%	88.1	0.2	11.7	99.6	0.4
	mol.%	33.4	0.6	66.0	98.2	1.8
P2	mass%	88.3	0.1	11.5	99.7	0.3
	mol.%	33.8	0.5	65.7	98.6	1.4
P3	mass%	61.6	11.5	26.9	74.0	26.0
	mol.%	11.0	17.4	71.6	38.8	61.2
P4	mass%	61.4	11.8	26.8	73.4	26.6
	mol.%	11.0	17.8	71.2	38.0	62.0
P5	mass%	60.3	11.8	27.9	73.0	27.0
	mol.%	10.5	17.4	72.1	37.6	62.4
P6	mass%	53.5	15.4	31.1	64.9	35.1
	mol.%	8.3	20.1	71.6	29.1	70.9
P7	mass%	61.6	12.1	26.3	72.9	27.1
	mol.%	11.1	18.4	70.5	37.5	62.5
P8	mass%	60.8	11.5	27.6	73.7	26.3
	mol.%	10.7	17.2	72.2	38.4	61.6
P9	mass%	59.6	12.4	28.0	71.8	28.2
	mol.%	10.2	18.1	71.6	36.1	63.9

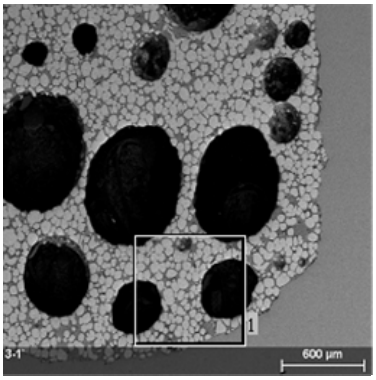

Fig. 2.22 - SEM data of the GPRS-21 polished axial crucible section with locations chosen for SEM/EDX studies (50.0 mol.% UO_2, 2200°C, 10 min exposition, crucible with cover)

Table 2.18 - EDX data of the GPRS-21 average composition of the crucible cross section (without molybdenum)

#		U	Si	O	UO_2	SiO_2
GPRS-21	mass%	69.7	6.3	24.1	85.5	14.5
	mol.%	14.5	11.0	74.5	56.8	43.2

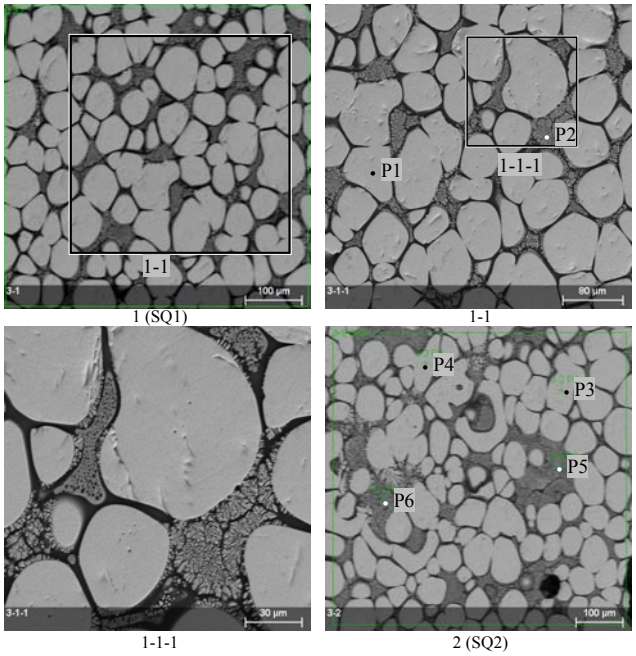

Fig. 2.23 - Microphotographs of crucible regions studied in GPRS21

Table 2.19 - EDX data of crucible regions studied in GPRS21

#		U	Si	O	UO_2	SiO_2
SQ1	mass%	73.7	6.3	20.1	86.2	13.8
	mol.%	17.3	12.5	70.2	58.1	41.9
SQ2	mass%	72.9	6.7	20.4	85.3	14.7
	mol.%	16.8	13.0	70.1	56.4	43.6
P1	mass%	86.9	0.3	12.8	99.4	0.6
	mol.%	31.1	0.8	68.0	97.4	2.6
P2	mass%	57.5	13.4	29.1	69.6	30.4
	mol.%	9.5	18.7	71.7	33.7	66.3
P3	mass%	86.5	0.2	13.2	99.5	0.5
	mol.%	30.3	0.7	68.9	97.6	2.4
P4	mass%	87.5	0.1	12.4	99.7	0.3
	mol.%	32.0	0.4	67.5	98.6	1.4
P5	mass%	57.9	14.7	27.4	67.6	32.4
	mol.%	9.8	21.1	69.0	31.7	68.3
P6	mass%	56.4	14.3	29.3	67.6	32.4
	mol.%	9.2	19.8	71.0	31.7	68.3

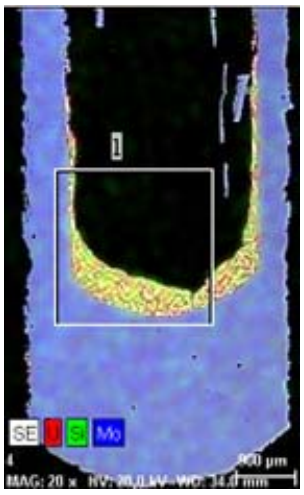

Fig. 2.24 – X-Ray mapping of the GPRS22 axial crucible section with locations marked for the SEM/EDX studies (40.0 mol.% UO_2, 2200 °C, 10 min exposition, crucible with cover)

Table 2.20- EDX data of the average composition of the GPRS-22 crucible cross section (without molybdenum)

#		U	Si	O	UO_2	SiO_2
GPRS-22	mass%	67.8	8.4	23.8	81.1	18.9
	Mol.%	13.8	14.4	71.9	48.9	51.1

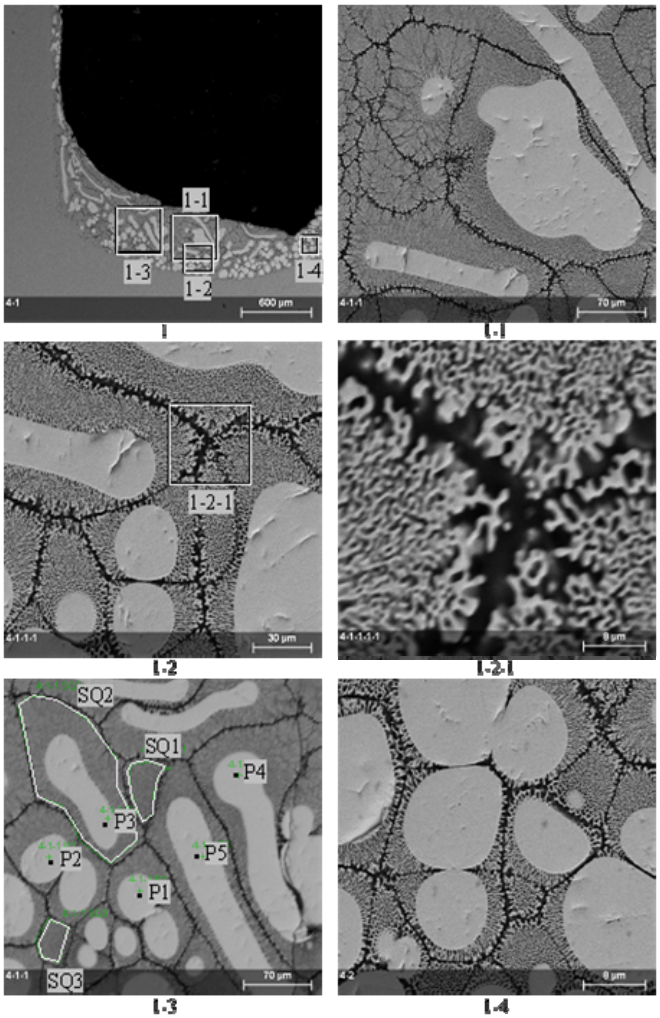

Fig. 2.25- Microphotographs of crucible regions studied in GPRS22

Table 2.21 - EDX data of crucible regions studied in GPRS22

#		U	Si	O	UO_2	SiO_2
SQ1	mass%	61.4	11.5	27.1	73.8	26.2
	mol.%	10.9	17.4	71.7	38.6	61.4
SQ2	mass%	69.2	7.9	22.9	82.2	17.8
	mol.%	14.5	14.1	71.4	50.8	49.2
SQ3	mass%	62.3	11.4	26.3	74.4	25.6
	mol.%	11.3	17.5	71.2	39.2	60.8
P1	mass%	85.0	0.3	14.7	99.3	0.7
	mol.%	27.7	0.9	71.4	96.9	3.1
P2	mass%	86.0	0.3	13.7	99.3	0.7
	mol.%	29.4	1.0	69.6	96.9	3.1
P3	mass%	86.5	0.2	13.3	99.6	0.4
	mol.%	30.2	0.5	69.3	98.2	1.8
P4	mass%	86.0	0.3	13.7	99.5	0.5
	mol.%	29.4	0.7	69.9	97.6	2.4
P5	mass%	86.5	0.2	13.2	99.5	0.5
	mol.%	30.3	0.7	69.0	97.9	2.1

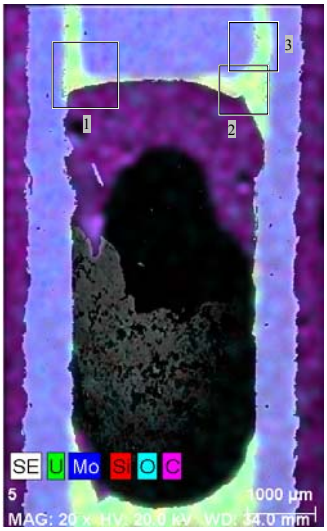

Fig. 2.26 – X-ray mapping of the GPRS23 axial crucible section with locations marked for the SEM/EDX studies SEM/EDX (70.0 mol.% UO_2, 2300 °C, 10 min exposition, crucible with cover)

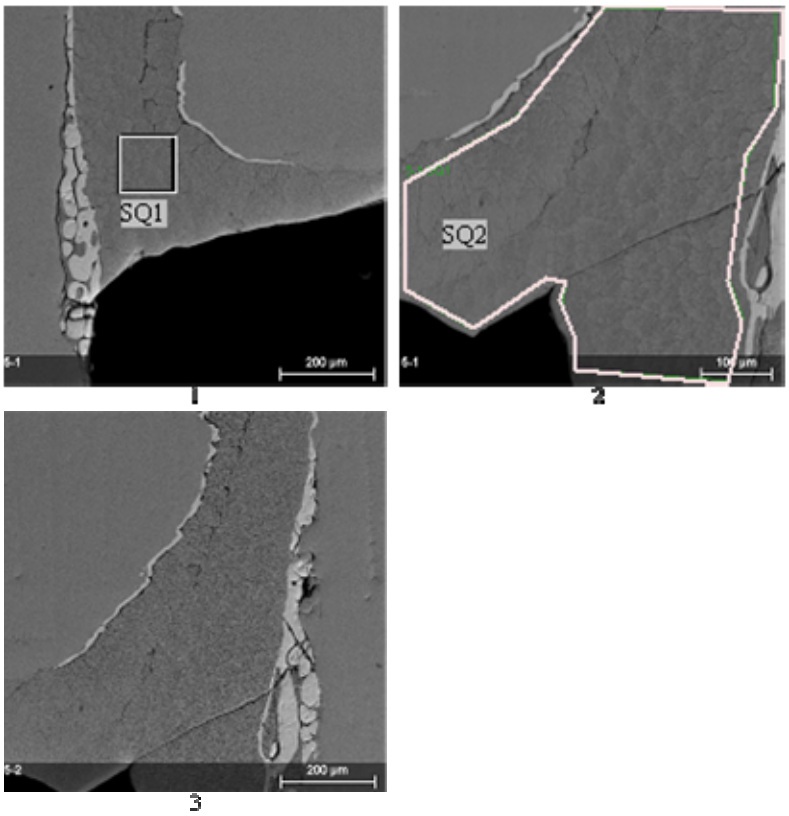

Fig. 2.27 - Microphotographs of crucible regions studied in GPRS23

Table 2.22- EDX data of crucible regions studied in GPRS23

#		U	Si	O	UO_2	SiO_2
SQ1	mass%	64.3	11.2	24.5	75.2	24.8
	mol.%	12.3	18.1	69.6	40.4	59.6
SQ2	mass%	62.9	11.0	26.2	75.2	24.8
	mol.%	11.5	17.1	71.4	40.3	59.7

Fig. 2.28- X-ray mapping of the GPRS24 axial crucible section with locations marked for the SEM/EDX studies (60.0 mol.% UO_2, 2300°C, 10 min exposition, crucible with cover)

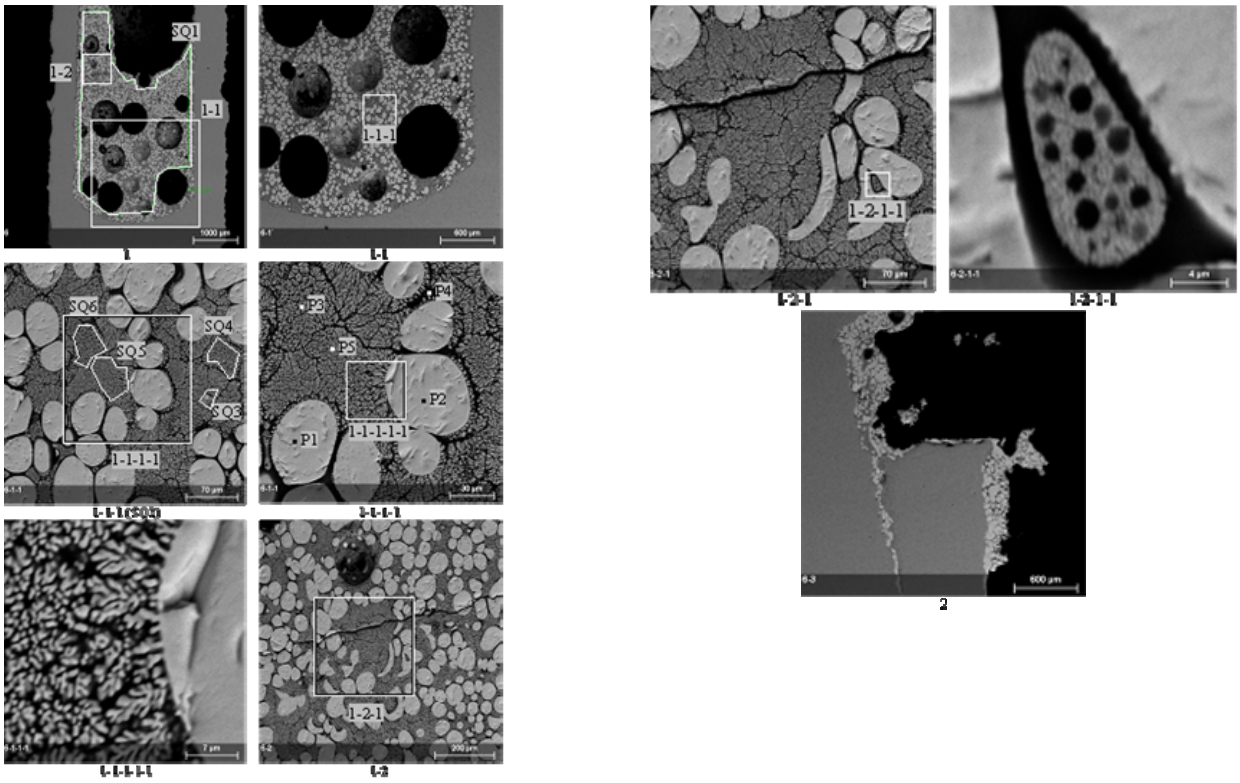

Fig. 2.29 - Microphotographs of crucible regions studied in GPRS24

Table 2.23- EDX data of crucible regions studied in GPRS24

#		U	Si	O	UO_2	SiO_2
SQ1	mass%	67.6	8.1	24.3	81.5	18.5
	mol.%	13.6	13.8	72.6	49.5	50.5
SQ2	mass%	70.1	7.5	22.4	83.3	16.7
	mol.%	15.0	13.6	71.4	52.6	47.4
SQ3	mass%	61.7	11.4	26.8	74.1	25.9
	mol.%	11.1	17.3	71.6	39.0	61.0
SQ4	mass%	61.7	11.6	26.8	73.9	26.1
	mol.%	11.1	17.6	71.4	38.6	61.4
SQ5	mass%	58.5	12.9	28.5	70.6	29.4
	mol.%	9.9	18.5	71.6	34.8	65.2
SQ6	mass%	59.0	13.1	27.8	70.4	29.6
	mol.%	10.1	19.0	70.9	34.7	65.3
P1	mass%	87.0	0.3	12.6	99.3	0.7
	mol.%	31.3	1.0	67.6	96.8	3.2
P2	mass%	85.5	0.2	14.2	99.5	0.5
	mol.%	28.6	0.7	70.8	97.8	2.2
P3	mass%	60.1	12.4	27.6	72.1	27.9
	mol.%	10.4	18.2	71.3	36.5	63.5
P4	mass%	50.0	17.7	32.2	59.9	40.1
	mol.%	7.4	22.1	70.5	25.0	75.0
P5	mass%	61.7	11.1	27.2	74.6	25.4
	mol.%	11.0	16.8	72.2	39.6	60.4

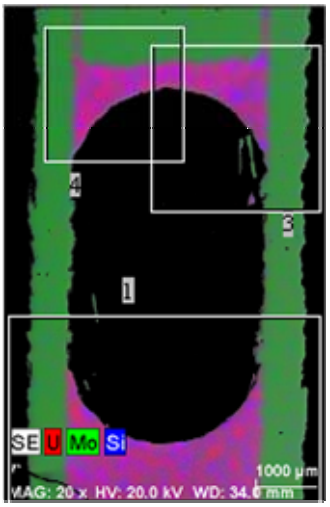

Fig. 2.30- X-ray mapping of the GPRS22 axial crucible section with locations marked for the SEM/EDX studies (50.0 mol.% UO_2, 2300°C, 10 min exposition, crucible with cover)

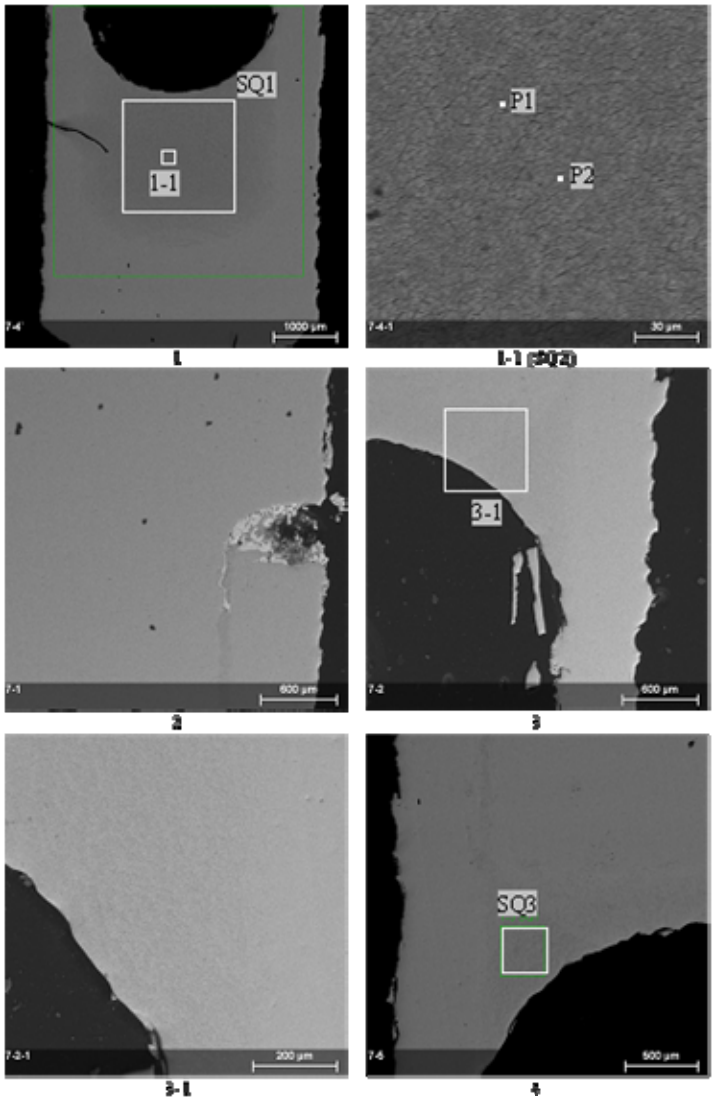

Fig. 2.31 - Microphotographs of crucible regions studied in GPRS26

Table 2.24 - EDX data of crucible regions studied in GPRS26

#		U	Si	O	UO_2	SiO_2
SQ1	mass%	64.0	11.4	24.6	74.9	25.1
	mol.%	12.2	18.3	69.5	39.9	60.1
SQ2	mass%	63.6	11.2	25.2	75.1	24.9
	mol.%	11.9	17.8	70.3	40.1	59.9
SQ3	mass%	65.9	11.3	22.9	75.6	24.4
	mol.%	13.1	19.1	67.8	40.8	59.2
P1	mass%	65.2	11.3	23.5	75.3	24.7
	mol.%	12.8	18.8	68.4	40.4	59.6
P2	mass%	63.7	11.5	24.8	74.5	25.5
	mol.%	12.0	18.4	69.5	39.4	60.6

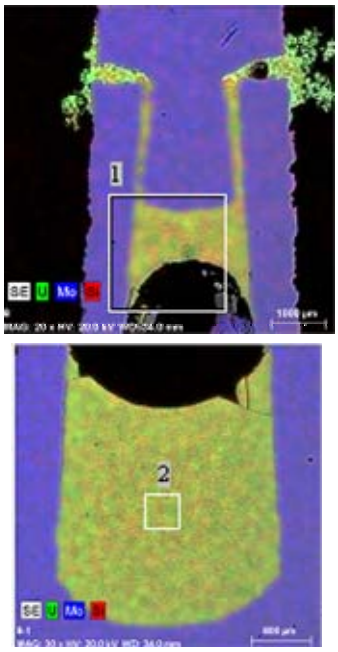

Fig. 2.32 – X-ray mapping of the GPRS24 axial crucible section with locations marked for the SEM/EDX studies (40.0 mol.% UO_2, 2300°C, 10 min exposition, crucible with cover)

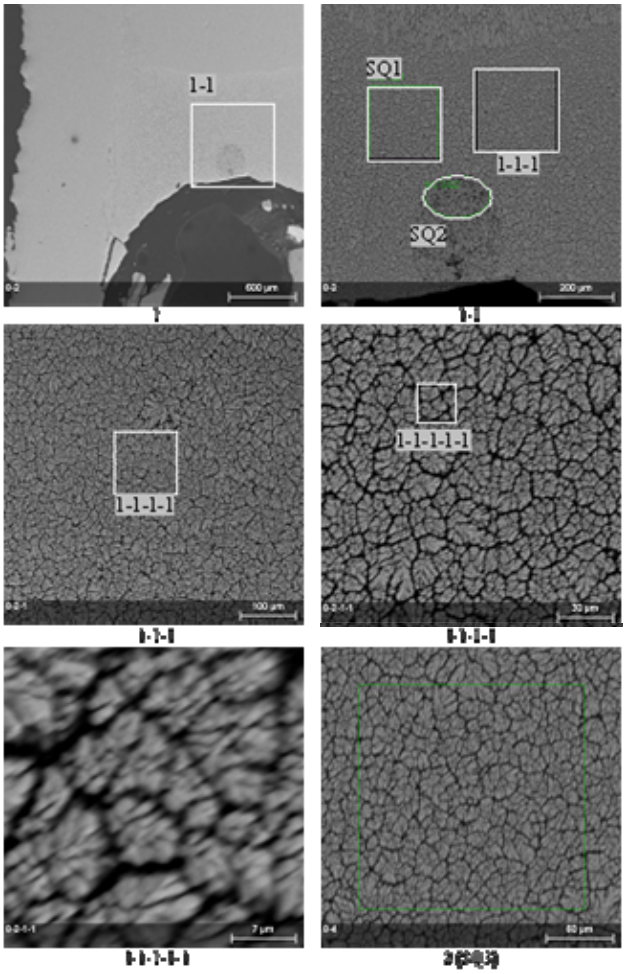

Fig. 2.33 - Microphotographs of crucible regions studied in GPRS28

Table 2.25 - EDX data of crucible regions studied in GPRS28

#		U	Si	O	UO_2	SiO_2
SQ1	mass%	67.6	9.7	22.8	78.7	21.3
	mol.%	13.8	16.8	69.3	45.1	54.9
SQ2	mass%	67.1	9.5	23.4	78.9	21.1
	mol.%	13.5	16.3	70.2	45.4	54.6
SQ3	mass%	65.9	9.7	24.4	78.3	21.7
	mol.%	12.9	16.1	71.1	44.5	55.5

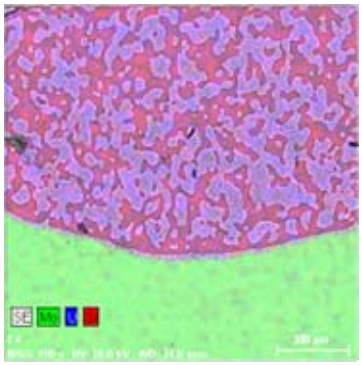

Fig. 2.34 – X-ray mapping of the GPRS25 axial crucible section with locations marked for the SEM/EDX studies (19.0 mol.% UO_2 from charge, 2175 °C, 10 min exposition)

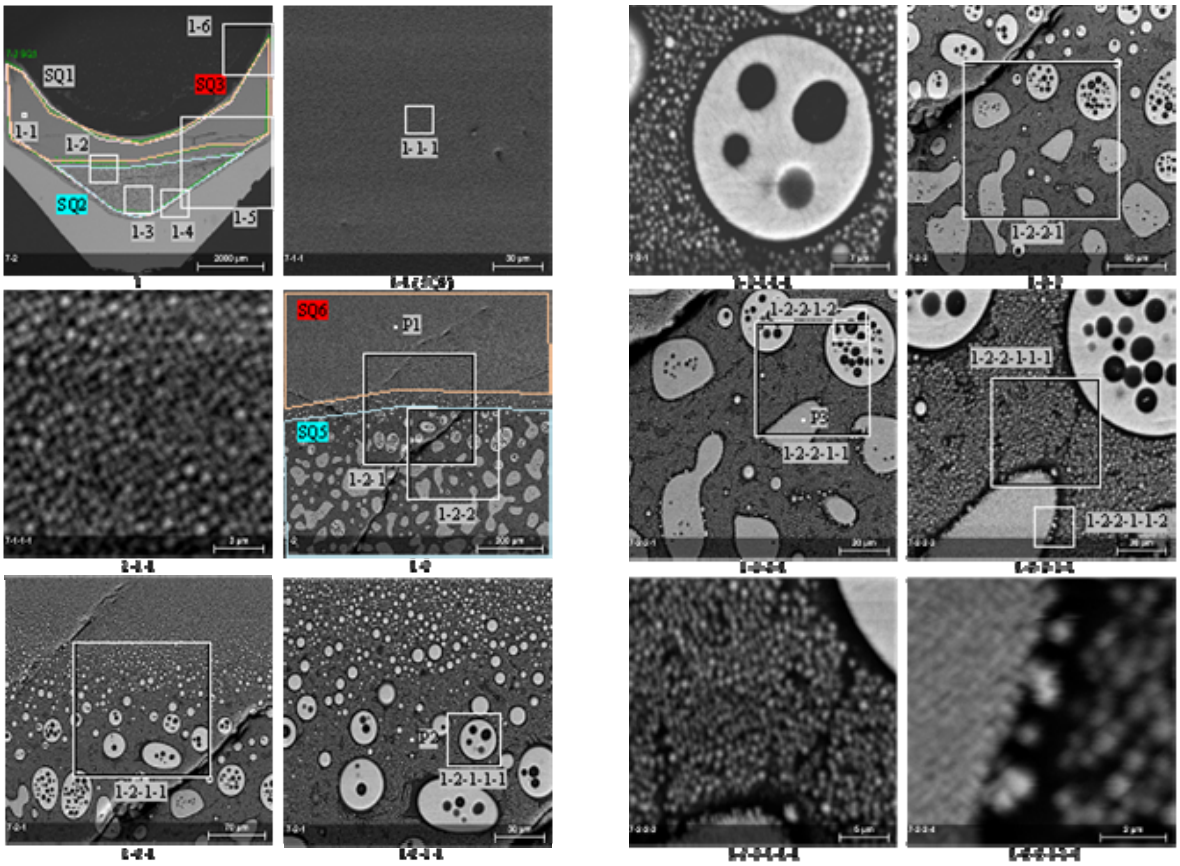

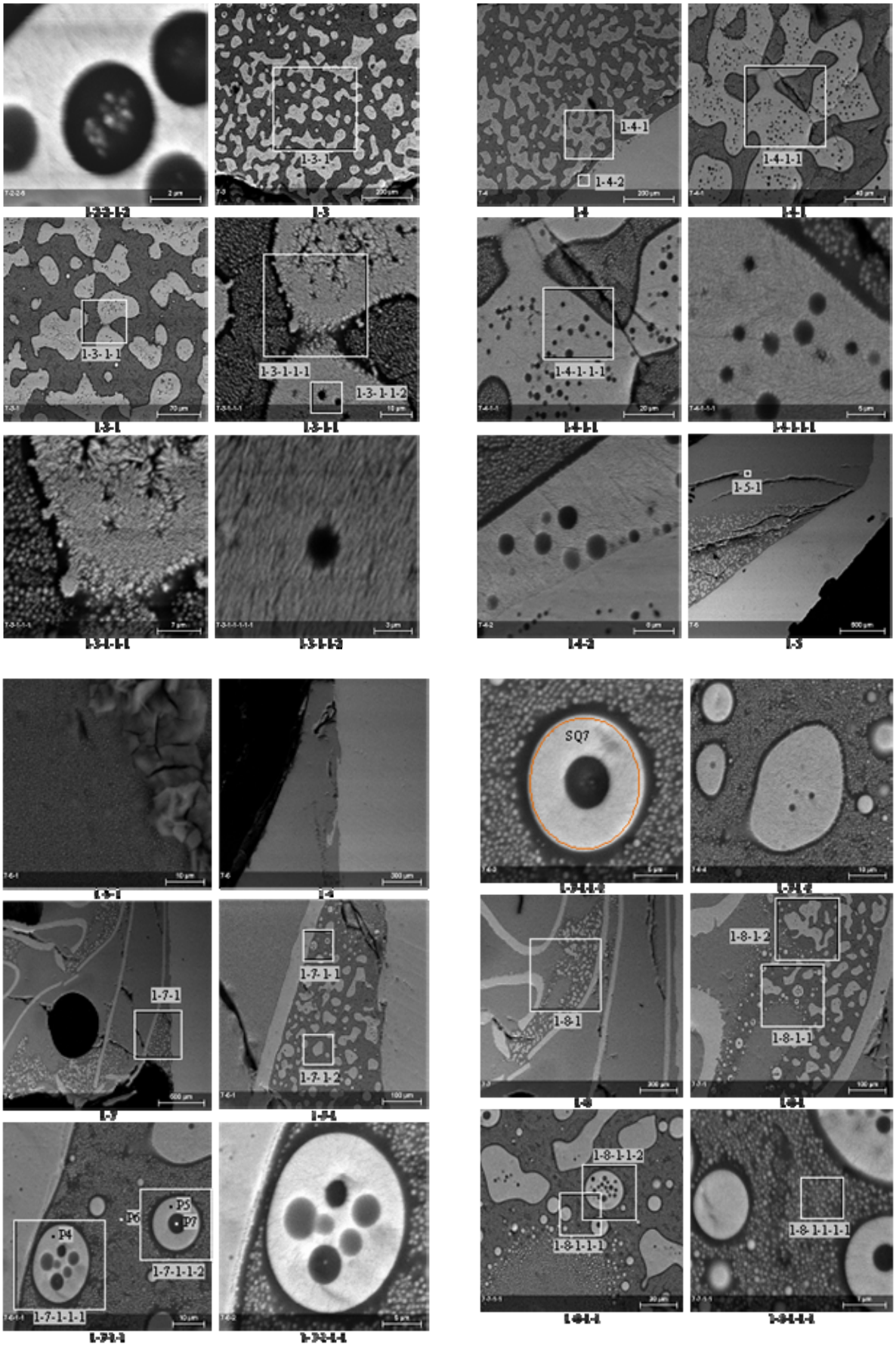
1-3-1
1-4-1
1-4-2
1-4-1-1
1-3-1-1
1-3-1-1-1
1-3-1-1-2
1-4-1-1-1
1-5-1
1-7-1
1-7-1-1
1-7-1-2
P4
P5
P6
P7
1-7-1-1-1
1-7-1-1-2
SQ7
1-8-1
1-8-1-2
1-8-1-1
1-8-1-1-2
1-8-1-1-1
1-8-1-1-1-1

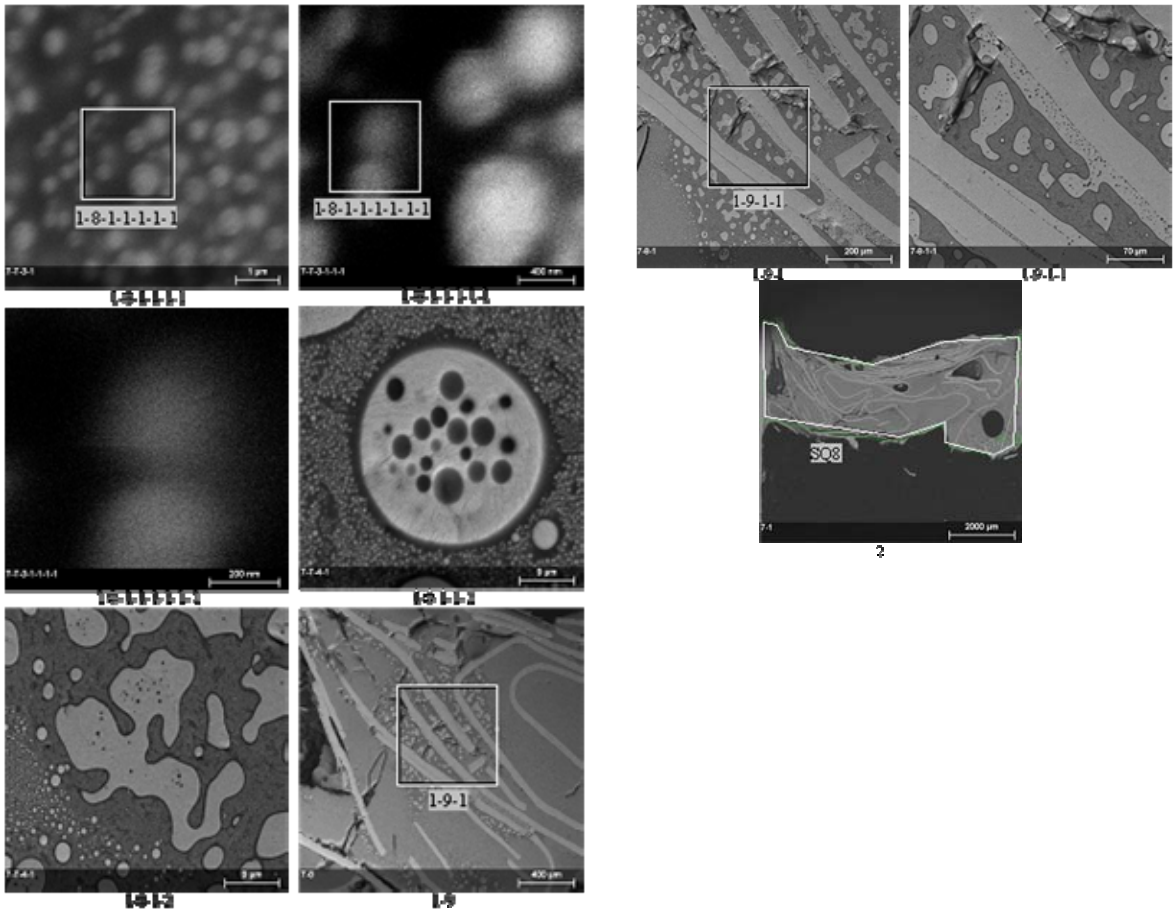

Fig. 2.35 - Microphotographs of crucible regions studied in GPRS25

Table 2.26 - EDX data of crucible regions studied in GPRS25

#		U	Si	O	UO_2	SiO_2
SQ1	mass%	43.6	21.7	34.7	51.6	48.4
	mol.%	5.9	24.7	69.4	19.2	80.8
SQ2	mass%	46.7	20.3	32.9	54.9	45.1
	mol.%	6.6	24.3	69.1	21.3	78.7
SQ3	mass%	42.8	22.1	35.1	50.7	49.3
	mol.%	5.7	24.9	69.4	18.6	81.4
SQ4	mass%	38.4	26.4	35.2	43.5	56.5
	mol.%	4.9	28.5	66.6	14.6	85.4
SQ5	mass%	45.6	20.8	33.6	53.8	46.2
	mol.%	6.3	24.4	69.3	20.6	79.4
SQ6	mass%	45.7	21.1	33.1	53.4	46.6
	mol.%	6.4	24.9	68.7	20.3	79.7
SQ7	mass%	60.6	13.9	25.6	69.8	30.2
	mol.%	10.8	21.1	68.1	34.0	66.0
SQ8	mass%	53.7	17.3	29.0	62.2	37.8
	mol.%	8.5	23.2	68.3	26.8	73.2

#		U	Si	O	UO_2	SiO_2
P1	mass%	46.2	21.4	32.4	53.4	46.6
	mol.%	6.5	25.5	68.0	20.3	79.7
P2	mass%	35.8	27.3	37.0	41.0	59.0
	mol.%	4.4	28.3	67.3	13.4	86.6
P3	mass%	61.6	12.4	26.0	72.5	27.5
	mol.%	11.1	19.0	69.8	36.9	63.1
P4	mass%	96.7	0.5	2.9	99.1	0.9
	mol.%	67.4	2.8	29.8	96.0	4.0
P5	mass%	74.5	7.0	18.5	85.0	15.0
	mol.%	18.2	14.4	67.4	55.8	44.2
P6	mass%	37.3	27.2	35.6	42.1	57.9
	mol.%	4.7	28.9	66.4	13.9	86.1
P7	mass%	51.7	18.0	30.3	60.4	39.6
	mol.%	7.9	23.3	68.8	25.3	74.7

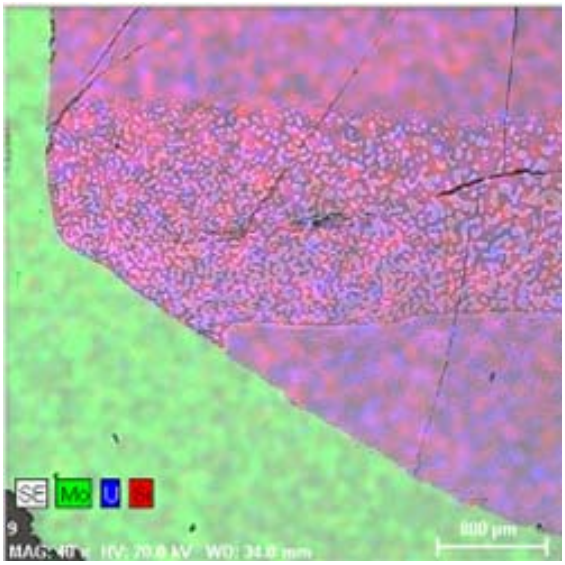

Fig. 2.36- X-ray mapping of the GPRS27 axial crucible section with locations marked for the SEM/EDX studies (19.0 mol.% UO_2 from charge, 2160 °C, 10 min exposition)

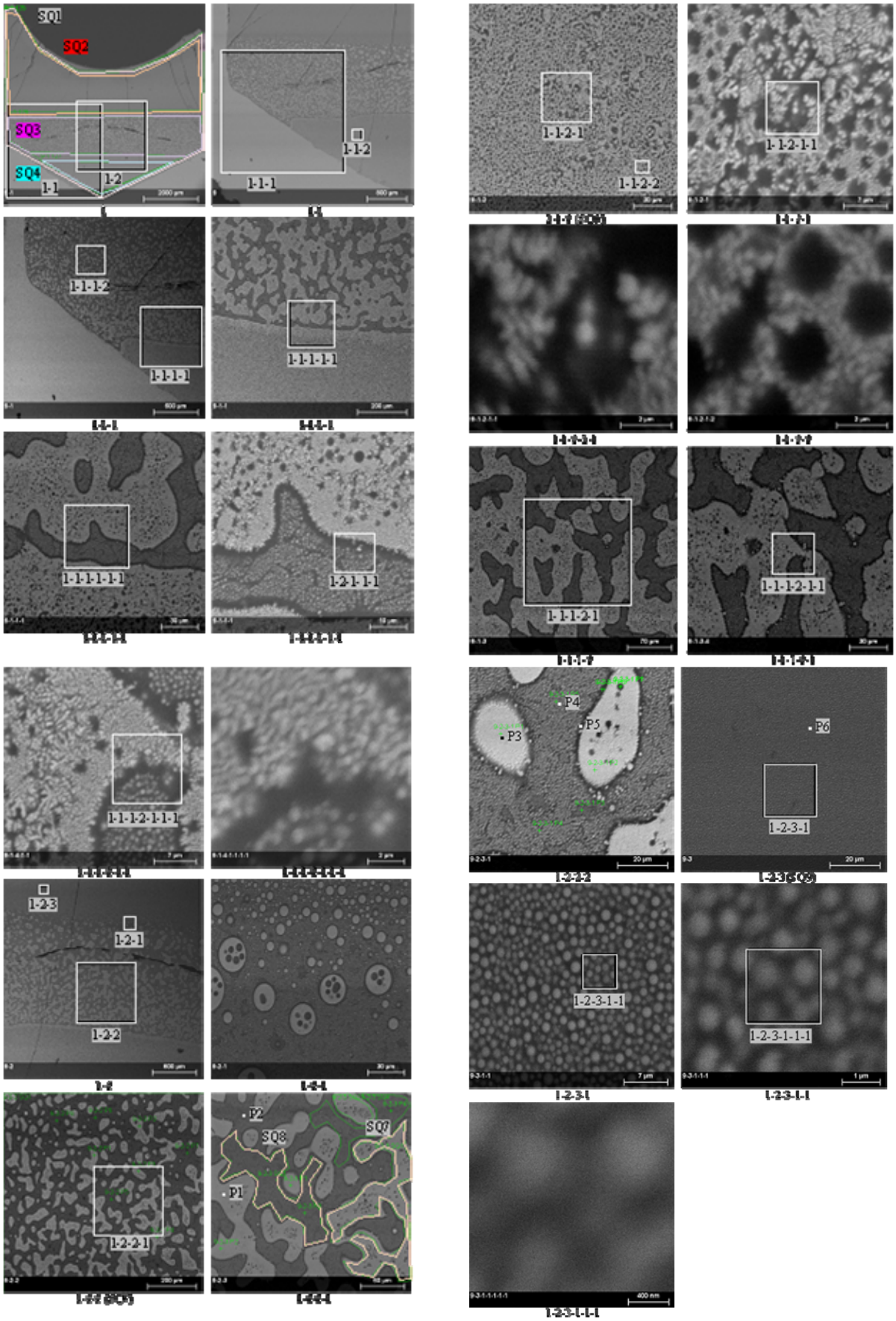

Fig. 2.37 - Microphotographs of crucible regions studied in GPRS27

Table 2.27 - EDX data of crucible regions studied in GPRS27

#		U	Si	O	UO_2	SiO_2
SQ1	mass%	45.7	22.7	31.6	51.7	48.3
	mol.%	6.5	27.1	66.4	19.2	80.8
SQ2	mass%	42.8	24.1	33.1	48.5	51.5
	mol.%	5.8	27.6	66.6	17.4	82.6
SQ3	mass%	48.6	21.6	29.8	54.4	45.6
	mol.%	7.2	27.2	65.6	21.0	79.0
SQ4	mass%	55.6	17.2	27.2	63.1	36.9
	mol.%	9.2	24.1	66.7	27.6	72.4
SQ5	mass%	54.8	17.4	27.8	62.6	37.4
	mol.%	8.9	23.9	67.1	27.1	72.9
SQ6	mass%	47.3	22.4	30.4	52.9	47.1
	mol.%	6.9	27.5	65.6	20.0	80.0
SQ7	mass%	50.7	19.9	29.4	57.4	42.6
	mol.%	7.7	25.7	66.6	23.1	76.9
SQ8	mass%	40.5	26.0	33.4	45.2	54.8
	mol.%	5.3	29.1	65.6	15.5	84.5
SQ9	mass%	44.6	23.7	31.7	50.0	50.0
	mol.%	6.2	28.0	65.8	18.2	81.8
P1	mass%	65.3	12.3	22.4	73.8	26.2
	mol.%	13.0	20.7	66.3	38.5	61.5
P2	mass%	37.7	27.4	34.9	42.2	57.8
	mol.%	4.8	29.4	65.8	14.0	86.0
P3	mass%	66.5	12.1	21.4	74.4	25.6
	mol.%	13.6	21.1	65.3	39.3	60.7
P4	mass%	38.5	28.0	33.5	42.2	57.8
	mol.%	5.0	30.7	64.3	14.0	86.0
P5	mass%	33.1	30.8	36.2	36.3	63.7
	mol.%	4.0	31.3	64.7	11.3	88.7
P6	mass%	44.1	23.6	32.3	49.8	50.2
	mol.%	6.1	27.6	66.3	18.1	81.9

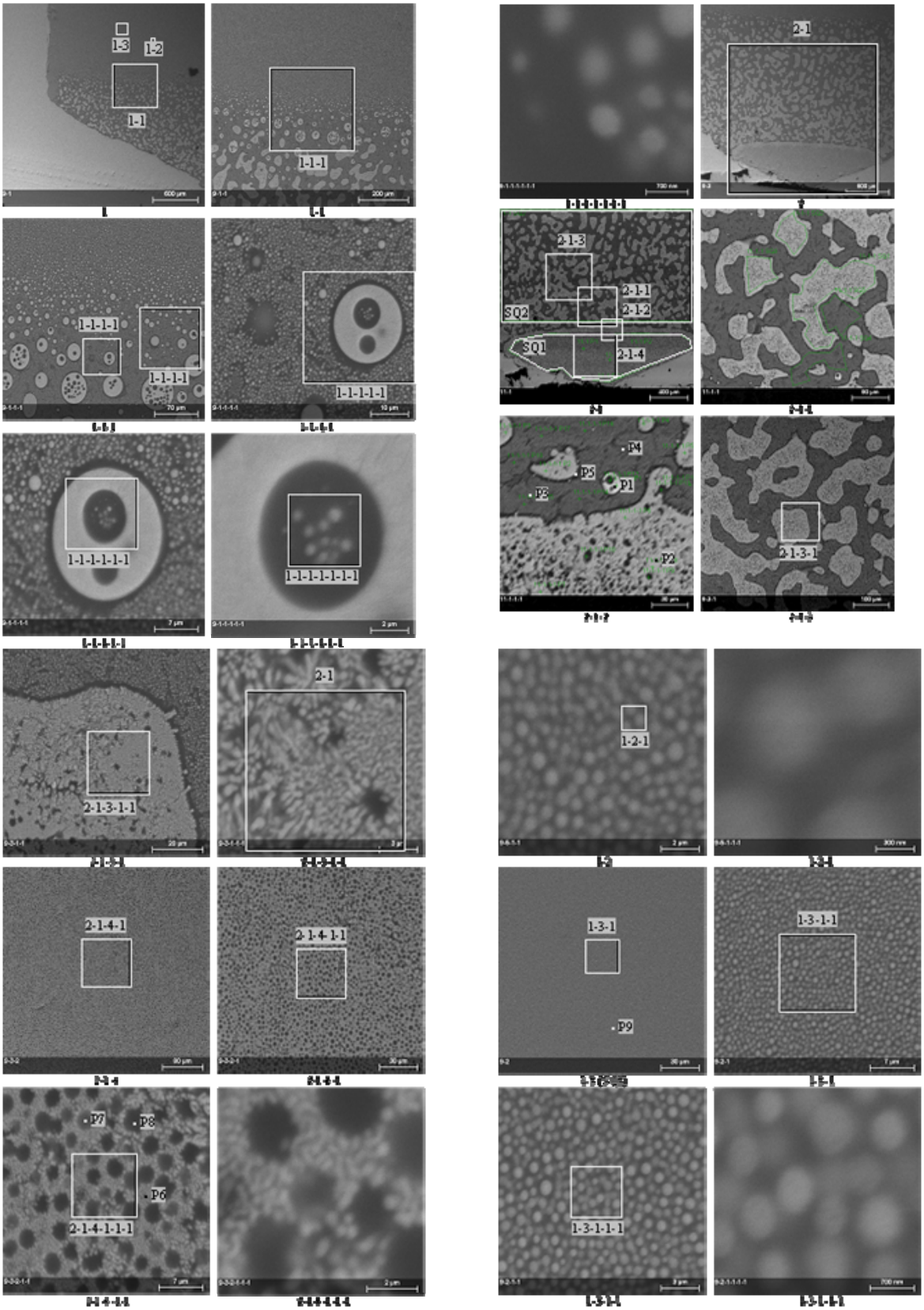

Fig. 2.38- Microphotographs of crucible regions studied in GPRS32(19.0 mol.% UO_2 from charge, 2130°C, 10 min exposition)

Table 2.28- EDX data of crucible regions studied in GPRS32

#		U	Si	O	UO_2	SiO_2
SQ1	mass%	53.9	18.1	28.0	61.3	38.7
	mol.%	8.7	24.6	66.8	26.0	74.0
SQ2	mass%	48.7	21.1	30.2	55.0	45.0
	mol.%	7.2	26.4	66.4	21.4	78.6
SQ3	mass%	47.4	21.4	31.2	54.1	45.9
	mol.%	6.8	26.1	67.0	20.8	79.2
P1	mass%	67.9	9.9	22.2	78.5	21.5
	mol.%	14.1	17.3	68.6	44.8	55.2
P2	mass%	60.2	13.7	26.2	70.0	30.0
	mol.%	10.6	20.5	68.9	34.2	65.8
P3	mass%	35.8	27.0	37.2	41.3	58.7
	mol.%	4.4	27.9	67.7	13.6	86.4
P4	mass%	38.4	26.7	34.9	43.3	56.7
	mol.%	4.9	28.8	66.3	14.5	85.5
P5	mass%	34.5	28.7	36.9	38.9	61.1
	mol.%	4.2	29.4	66.4	12.4	87.6
P6	mass%	60.8	15.1	24.1	68.1	31.9
	mol.%	11.1	23.4	65.5	32.2	67.8
P7	mass%	56.0	16.8	27.2	63.8	36.2
	mol.%	9.3	23.6	67.1	28.2	71.8
P8	mass%	47.1	20.4	32.5	55.1	44.9
	mol.%	6.7	24.6	68.7	21.4	78.6
P9	mass%	47.4	21.2	31.4	54.3	45.7
	mol.%	6.8	25.9	67.3	20.9	79.1

Conclusions on the UO_2-SiO_2 system

Table 2.29 gives the comparison of data provided by chemical analysis and EDX of melt samples.

Table 2.29- PRS9 melt analysis results

Item	Content derived from data, mol.%			
	Content, mass % (EDX)		Content, mass % (ChA)	
	UO_2	SiO_2	UO_2	SiO_2
Sample #1	93.4	6.6	94.2	5.8
Sample #2	95.0	5.0	93.7	6.3
Sample #3	95.5	4.5	93.8	6.2

The comparison of EDX and chemical analysis data has shown their good convergence. As EDX is a microanalysis, the compositions of experimental samples determined by the chemical analysis were plotted in the diagram.

Recommended experimental data on liquidus temperatures of different compositions are given in Table 2.30.

Table 2.30- Measured liquidus temperatures for melt compositions in PRS9

Item	Content derived from data XA, at.%		Tliq, C
	UO_2	SiO_2	
Sample #1	78.20±3.91	21.80±3.10	2573±38.6
Sample #2	76.73±3.84	23.27±3.02	2563±38.4
Sample #3	76.98±3.85	23.02±3.03	2541±38.1

2. Specified boundaries of the miscibility gap are given in Fig. 2.39 The critical point of the miscibility gap is located between 2080 and 2200 °C

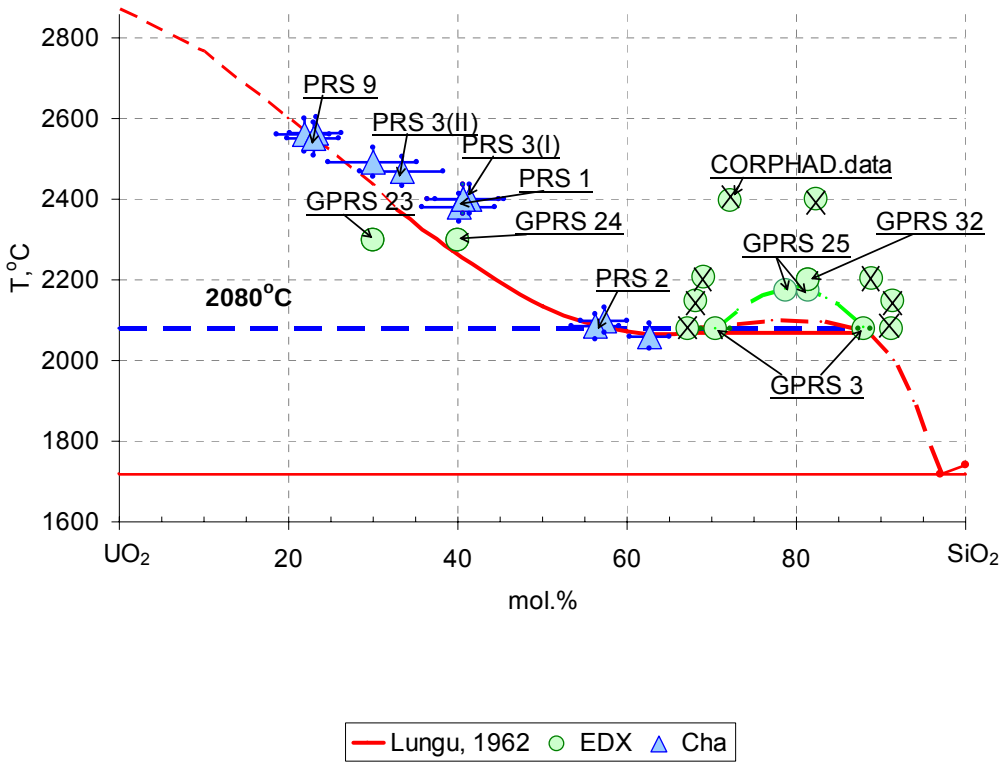

Fig. 2.39- Produced data in comparison with the Lungu UO_2-SiO_2 phase diagram

UO_2-CaO system

To study the binary oxidic system UO_2-CaO in the PRS experimental series the VPA IMCC method and SEM/EDX analysis were used.

Experiments PRS10-12 were performed on the Rasplav-4 test facility. Furnace schematics is given in Fig 2.1.

Table 2.31 shows the PRS experimental matrix for the UO_2-CaO system.

Table 2.31 - PRS experimental matrix for the UO_2-CaO system

Test	Charge composition, mass% / mol.%		Objectives
	UO_2	CaO	
PRS10	73.2 / 36.2	26.8 / 63.8	Determine T_{liq} by VPA IMCC. Ingot removal from the inductor at the speed of 10 mm/h to form the eutectic nucleus and equilibrium structures of solid solution
PRS11	67.4 / 30	32.6 / 70	
PRS12	87.8 / 60	12.2 / 40	Determine T_{liq} by VPA IMCC for two melt compositions:
	91.8 / 70	8.2 / 30	

- **Experiment PRS10**

Table 2.32 shows the PRS10 experimental procedure.

Table 2.32 - PRS10 experimental procedure

Time from the experiment start, s	Stage
0-500	Startup heating , molten pool formation .Charge is added and molten pool is homogenized. Temperature on the molten pool surface is 2400°C.
511-519	Molten pool and bottom crust are measured. They are 58 and 10 mm respectively.
898-1798	Power deposition into the melt is lowered to reduce temperature on the melt surface. Melt surface temperature was 2100°C
1436-1450	Molten pool and bottom crust are measured. They are 62 and 8 mm respectively.
2019-2082	1st melt sample is taken.
2144-2215	Crucible is shifted up to reduce the surface temperature and crystallization start. Melt temperature before the shift is 2150°C. Even at a considerable shift the crust was not formed due to strong superheating above the liquidus temperature.
2199-2397	Power deposition into the melt is lowered to reduce temperature on the melt surface. Melt surface temperature is 2031°C
2397-2453	2nd melt sample is taken
2453-2523	Crucible is shifted up to reduce the surface temperature and crystallization start.. Melt temperature before the shift is 2030°C. Even at a considerable shift the crust was not formed due to strong superheating above the liquidus temperature.
2523-2668	Further reduction of power deposition into the melt. Convective pattern on the melt surface disappeared.
2668-2848	Power deposition into the melt is increased. Convective pattern reappears. Melt temperature was 2030°C.
2996-3027	Molten pool and bottom crust are measured. They are 46 and 17 mm respectively.
3077-3099	3rd melt sample is taken
3123-3252	VPA IMCC #1

Time from the experiment start, s	Stage
3336-3373	4th melt sample is taken
3397-3497	VPA IMCC #2
3647-4130	Crucible is shifted down versus the inductor until the plate current is changed
4207-4220	Molten pool and bottom crust are measured. They are 36 and 25 mm respectively
4296	Ingot is taken out of the crucible during two hours. Before disconnection the pool has a solid region, like in PRS4.
11664	HF heating is disconnected. The ingot is crystallized in nitrogen and cooled.

Fig. 2.40 shows pyrometer readings (Tm), voltage (Ua), plate current (Ia), heat transfer from the crucible (Qccr) versus time. Figures 2.41, 2.42 show thermogram fragments at the time of liquidus temperature measurement.

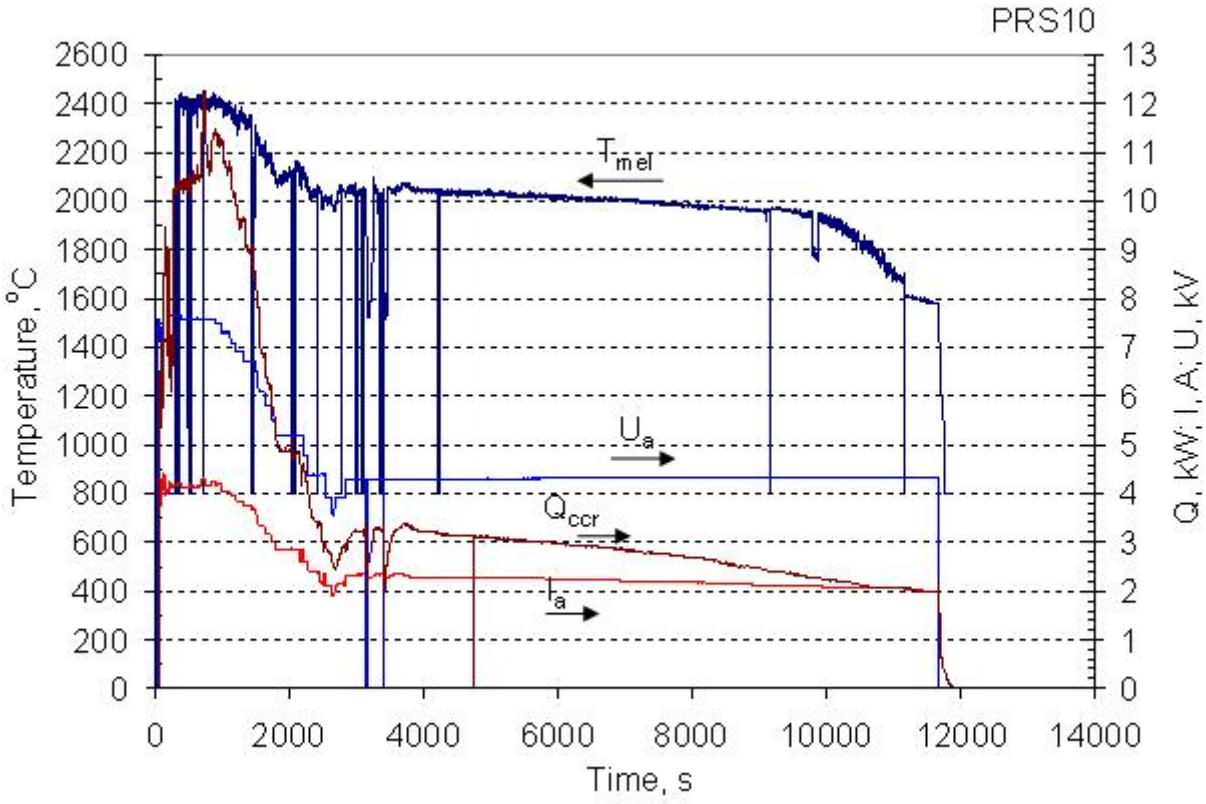

Fig. 2.40- Plate voltage (U_a) and current (I_a), heat transfer from the crucible (Q_{ccr}), melt temperature by pyrometer(T_{mel}) versus time in PRS10

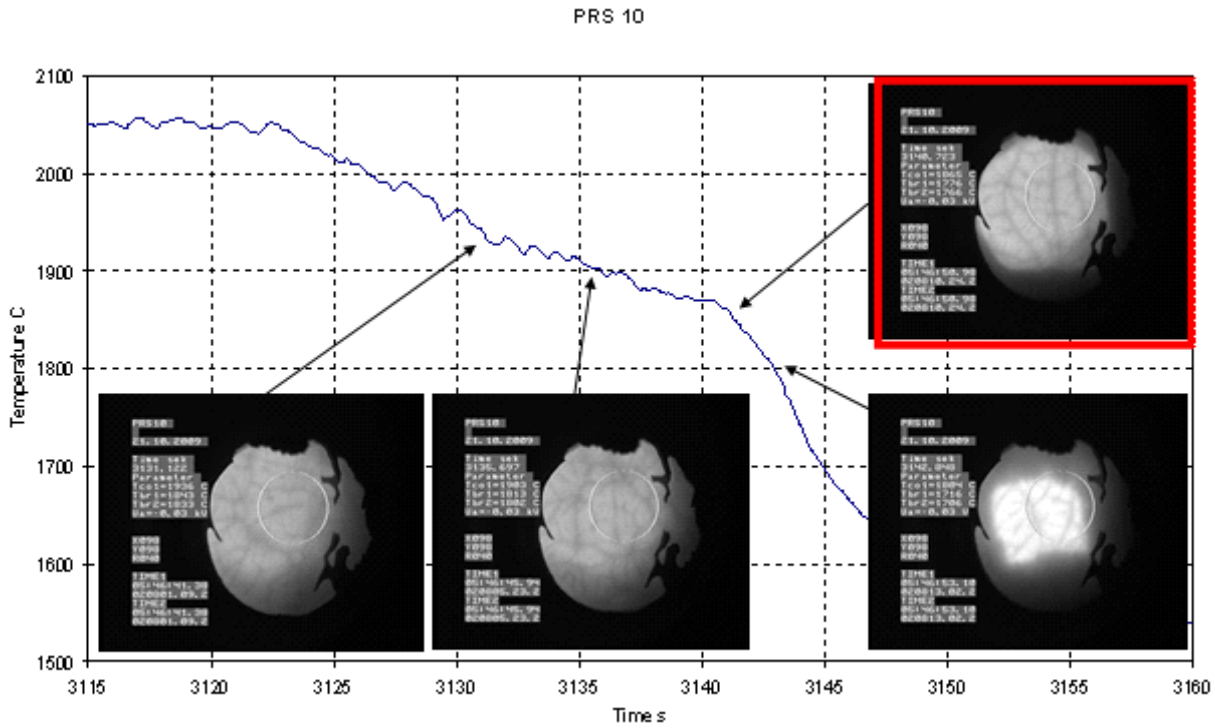

Fig. 2.41- PRS10 thermogram fragment during VPA IMCC #1

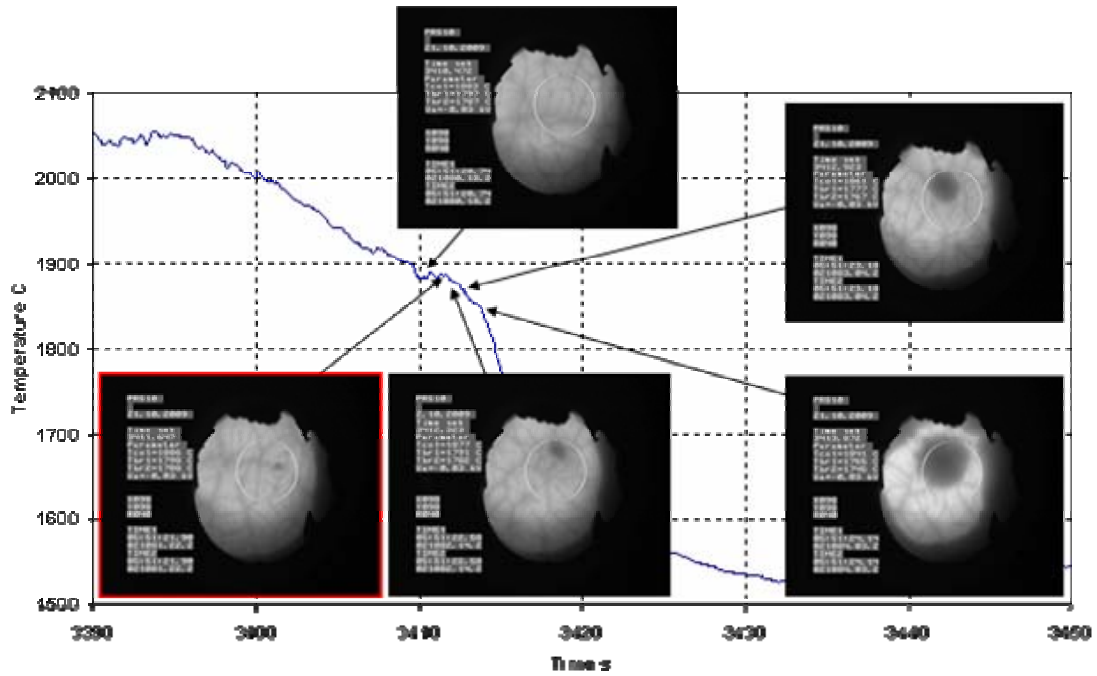

Fig. 2.42- PRS10 thermogram fragment during VPA IMCC #2

Liquidus temperatures measured in the experiment are 1865, 1865°C, respectively. Average T_{liq}=1865±28°C.

Fig. 2.43 shows the crucible after experiment. Table 23.2 gives 17 and 25 mm crust thicknesses during T_{liq} measurements. As the composition was changing during the

experiment, each measurement was preceded by the melt sampling. At VPA IMCC melt composition was determined from the physicochemical analysis of melt samples No 3 and 4 taken immediately before the measurement.

Fig. 2.44 shows the photograph of PRS1o ingot. After experiment the ingot was taken from the crucible, weighed, included into the epoxy resin and cut along the axis. A ½ part of the ingot was used to make a polished section for the SEM/EDX analysis, and an average sample was made from the second half for the physicochemical analysis. Fig. 2.44 shows the photograph of PRS10 ingot.

Fig. 2.43- Crucible after PRS10

Fig. 2.44- PRS10 ingot top and side view

Table 2.33 gives PRS10 mass balance.

Table 2.33 - PRS10 mass balance

Introduced into the		Collected, g	
UO_2	287.32	**Ingot**	302.08
CaO	107.24	**Melt samples**	8.54
U	5.00	**Probe sample**	11.76
		Aerosols	0.92
		Above-melt crust	46.78
		Spillages[1)]	28.98
Σ	**399.56**	**Σ**	**399.06**
Imbalance	**-0.50**		

Note:
[1)] – Spillages- unreacted charge and aerosols, collected from sections when the crucible was disassembled.

Table 2.34 shows the chemical analysis data of molten products and elemental material balance of experiment PRS10 recalculated for oxides. Only uranium content was evaluated by chemical method [3,4,5] and recalculated for UO_2, and the content of CaO was calculated from the residue.

The following assumptions were taken in the elemental material balance:

1. As the mass of aerosols collected during the experiment is very small (m=0.92 g), they were not analyzed.
2. Samples from the probe were not analyzed as well, because their content was assumed to be identical to the samples of melt #1, collected practically at the same time.
3. CaO content in the samples is calculated from the residue.

Table 2.34 –PRS10 chemical analysis of corium samples and elemental material balance

Item	Content, mass%		Mass, g	Mass, g	
	UO_2	CaO[1)]		UO_2	CaO
Melt sample #1	74.16	25.84	2.43	1.80	0.63
Melt sample #2	72.6	27.4	2.04	1.48	0.56
Melt sample #3	73.6	26.4	2.13	1.57	0.56
Melt sample #4	71.55	28.45	1.95	1.40	0.55
Above-melt crust	66.93	33.07	46.78	31.31	15.47
Ingot	73.04	26.96	302.08	220.64	81.44
Spillages[2)]	73.21	26.79	28.98	21.22	7.77
Aerosols	100.00	-	0.92	0.92	-
Probe sample	74.16	25.84	11.76	8.72	3.04
Collected, g				289.05	110.03
Introduced, g				292.99	107.24
Imbalance, g				-3.94	+2.79

Note:
[1)]- calculated from the residue.
[2)] – spillages – unreacted charge and aerosols dropped from sections when the crucible was disassembled

It can be seen from the presented mass balance of experiment PRS10 (Table 2.34) that the imbalance for uranium oxide (-3.94 g), and for calcium oxide (+2.79 g), which is 1.34 and 2.6% of the introduced amount, is basically explained by the analysis error; for U it is not more than 5 rel.%.

Table 2.35 shows XRF data of corium samples and elemental material balance of experiment PRS10 recalculated for oxides [6].

The following simplifications were made in the elemental material balance:

1. As the mass of aerosols collected during the experiment is very small (m=0.92 g), they were not analyzed.
2. Samples from the probe were not analyzed as well, because their content was assumed to be identical to the samples of melt #1, collected practically at the same time.

Table 2.35 –PRS10 XRF of corium samples and elemental material balance

Item	Content, mass%		Mass, g	Mass, g	
	UO_2	CaO		UO_2	CaO
Melt sample #1	77.51	22.49	2.43	1.89	0.55
Melt sample #2	76.8	23.2	2.04	1.56	0.47
Melt sample #3	76.19	23.81	2.13	1.62	0.51
Melt sample #4	74.01	25.99	1.95	1.44	0.51
Above-melt crust	75.01	24.99	46.78	35.09	11.69
Ingot	75.30	24.70	302.08	227.47	74.61
Spillages[1)]	73.21	26.79	28.98	21.22	7.77
Aerosols[2)]	100	-	0.92	0.92	-
Probe sample	77.51	22.49	11.76	9.11	2.64
Collected, g				300.33	98.74
Introduced, g				292.99	107.24
Imbalance, g				+7.34	-8.50

Note:
1) – "spillages' – unreacted charge and aerosols dropped from the sections when the crucible was disassembled.
2) aerosols collected on the F3 filter were analyzed, their composition was identical to all aerosols of the experiment.

It is seen from the PRS10 mass balance (Table 2.35) that UO_2 imbalance is +7.34 g, and for CaO it is -8.50 g, which is 2.5 and 7.9% of the introduced quantity. It is mostly explained by the analysis error. The comparison of elemental mass balances compiled using XRF (Table 2.35) and ChA (Table 2.34) has shown that the imbalance for ChA data is considerable smaller. The ChA data for samples collected during the experiment were plotted in the diagram for the correlation with the liquidus temperature determined by the VPA IMCC.

SEM/EDX analysis of PRS10 is in progress.

- **Experiment PRS11**

Table 2.36 shows PRS11 experimental procedure.

Fig. 2.45 shows pyrometer readings (Tm), plate voltage (Ua) and current (Ia) versus time. Figures 2.46-2.48 show thermogram fragments at the time of liquidus temperature measurement.

Table 2.36 –PRS11 experimental procedure

Time from the experiment start, s	Stage/observations
0-300	Startup heating , molten pool formation .Charge is added and molten pool is homogenized. Temperature on the molten pool surface is 2420°C.
364-368	Molten pool and bottom crust are measured. They are 50 and 13 mm respectively.
900-1300	Power deposition into the melt is increased to melt bottom crust. Temperature on the melt surface is 2500°C.
1392-1403	Molten pool and bottom crust are measured. They are 51 and 11 mm respectively
1535-1616	Crucible is shifted up to start the crystallization. Melt temperature before the shift is

Time from the experiment start, s	Stage/observations
	2500°C. Even at a considerable shift the crust was not formed due to strong superheating above the liquidus temperature.
1829-2460	Power deposition into the melt is lowered to reduce temperature on the melt surface. Melt surface temperature is 2250°C
2499-2510	Molten pool depth and bottom crust thickness are measured. They are 46 and 15 mm respectively
2557-2613	Crucible is shifted up by 50mm to produce films-crusts. Melt temperature before the shift is 2250°C. Crust formation on the molten pool surface is registered.
2793-2845	1st melt sample is taken
2867-2922	VPA IMCC measurement #1
3130-3293	2nd melt sample is taken by two samplers
3310-3366	VPA IMCC measurement #2
3708-3893	3rd melt sample is taken by three samplers
3916-3970	VPA IMCC measurement #3
4050-4630	Power deposition into the melt is decreased to reduce the melt surface temperature. Temperature on the melt surface is 2160°C
4699-4800	Crucible is shifted down versus the inductor until the plate current changes
4829-13330	Ingot is moved out of inductor at 10 mm/h
13335	HF heating is disconnected. The ingot is crystallized in nitrogen and cooled.

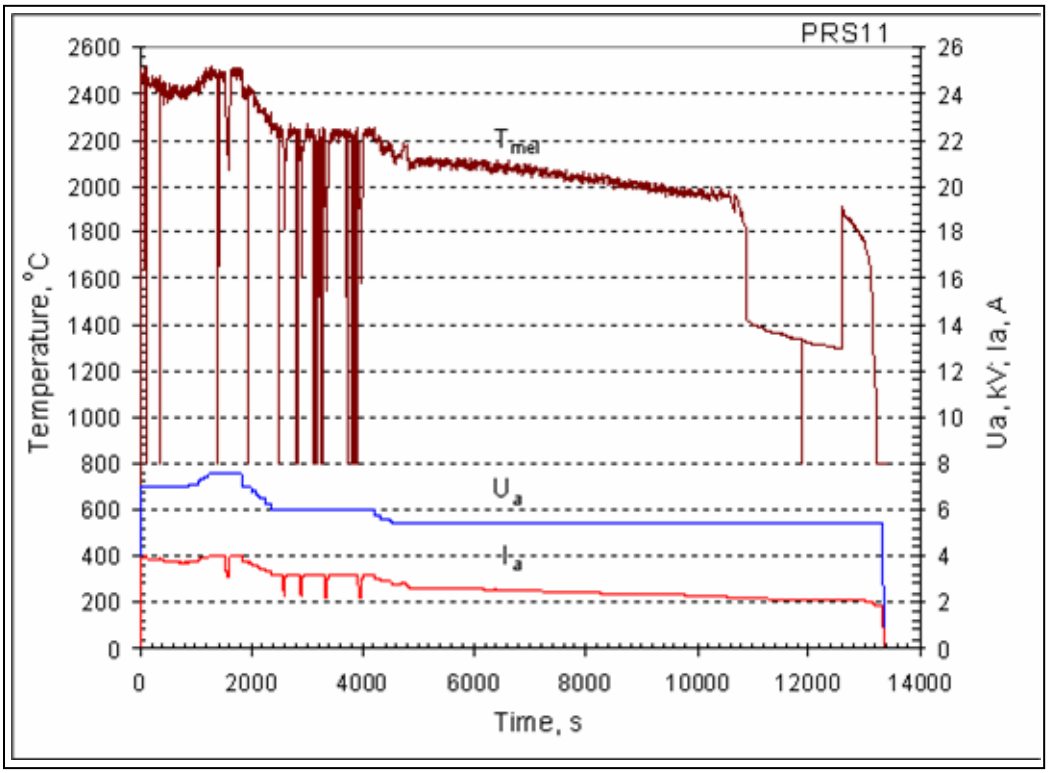

Fig. 2.45- PRS11 pyrometer readings (T_m), plate voltage (U_a), current (I_a) versus time

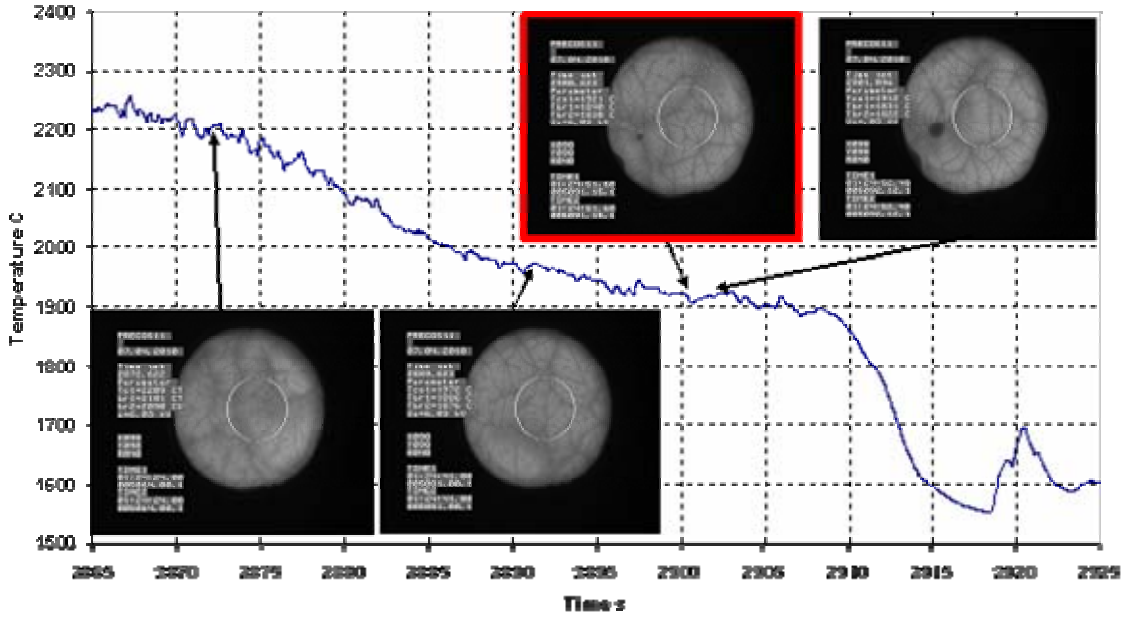

Fig. 2.46- PRS11 thermogram fragment during VPA IMCC measurement #1

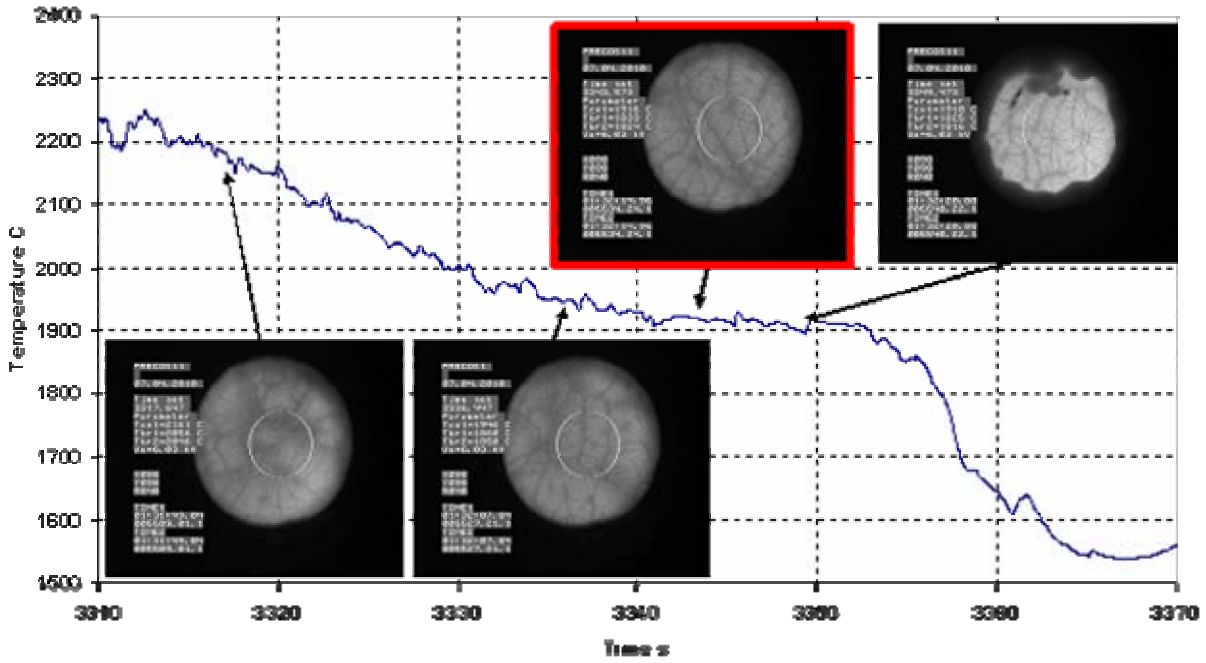

Fig. 2.47- PRS11 thermogram fragment during VPA IMCC measurement #2

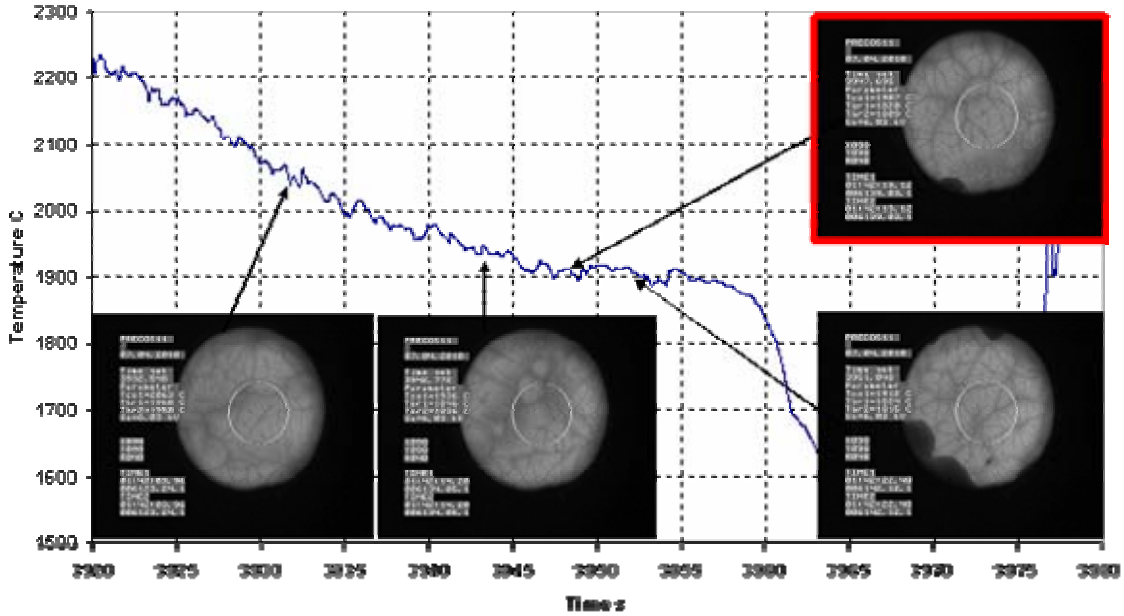

Fig. 2.48- PRS11 thermogram fragment during VPA IMCC measurement #3

Liquidus temperatures measured in the experiment are 1921, 1916, 1907°C, respectively. Average T_{liq}=1915±29°C.

Fig. 2.49 shows the PRS11 ingot picture. After experiment the ingot was taken from the crucible, weighed, included into the epoxy resin and made an axial cut. A ½ part of the ingot was used to make a polished section for the SEM/EDX analysis, and an average sample was made from the second half for the physicochemical analysis. Fig. 2.49 shows the photograph of PRS11 ingot.

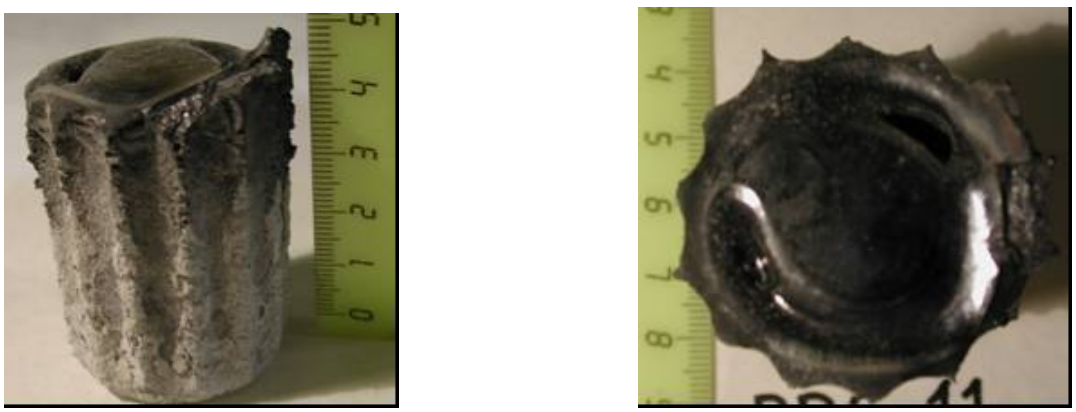

Fig. 2.49- PRS11 ingot top and side view

Table 2.37 gives PRS11 mass balance.

Table 2.37 –PRS11 mass balance

Introduced into the		Collected, g	
UO_2	230.08	**Ingot**	267.13
CaO	114.24	**Samples**	12.36
U	5.00	**Probe sample**	4.90
		Aerosols	4.81
		Above-melt crust	42.78
		Spillages[1)]	17.97
Σ	**349.32**	**Σ**	**349.95**
Imbalance	**+0.63**		

Note:
[1)] – Spillages- unreacted charge and aerosols, collected from sections when the crucible was disassembled.

Table 2.38 shows the chemical analysis data of molten products and elemental material balance of experiment PRS11 recalculated for oxides.

Table 2.38 –PRS11 chemical analysis of corium samples and elemental material balance

Item	Content, mass%		Mass, g	Mass, g	
	UO_2	**CaO[1)]**		**UO_2**	**CaO**
Melt sample #1	67.88	32.12	4.81	3.27	1.54
Melt sample #2	67.46	32.54	3.2	2.16	1.04
Melt sample #3	68.18	31.82	4.35	2.97	1.38
Probe sample	65.75	34.25	4.9	3.22	1.68
Above-melt crust	65.04	34.96	42.78	27.82	14.96
Spillages [2)]	50.07	49.93	17.97	9.00	8.97
Aerosols[3)]	33.49	66.51	4.81	1.61	3.2
Ingot	67.27	32.73	267.13	179.7	87.43
Collected, g				229.74	120.21
Introduced, g				235.75	114.24
Imbalance, g				-6.01	+5.97

Note:
[1)]- calculated from the residue.
[2)] –spillages – unreacted charge and aerosols dropped from sections when the crucible was disassembled; 3) - aerosols collected by the F3 filter were analyzed; their composition was identical to all aerosols of the experiment.

UO_2 imbalance (-6.01 g), and CaO imbalance (+5.97 g) amount to 2.5 and 5.2% of the introduced quantity. It is explained mostly by the error, which for U and Ca is 5 rel.%.

Table 2.39 shows XRF data of corium samples and elemental mass balance of experiment PRS11 recalculated for oxides.

Table 2.39– XRF data of corium samples and elemental mass balance of PRS11

Item	Content, mass%		Mass, g	Mass, g	
	UO_2	CaO		UO_2	CaO
Melt sample #1	69.38	30.62	4.81	3.34	1.47
Melt sample #2	70.25	29.75	3.2	2.25	0.95
Melt sample #3	71.72	28.28	4.35	3.12	1.23
Probe sample	76.8	23.2	4.9	3.76	1.14
Above-melt crust	70.29	29.71	42.78	30.07	12.71
Spillages [1)]	38.42	61.58	17.97	6.9	11.07
Aerosols[2)]	46.9	53.1	4.81	2.26	2.55
Ingot	68.69	31.31	267.13	183.49	83.64
Collected, g				235.18	114.77
Introduced, g				235.75	114.24
Imbalance, g				-0.57	+0.53

Note:
[1)] - Spillages – unreacted charge and aerosols dropped from crucible sections when they were disassembled
[2)] -Aerosols collected by the F3 filter were analyzed; their composition was identical to all aerosols of the experiment.

Imbalance for uranium oxide (-0.57 g) and for calcium oxide (+0.53 g) is 0.23 and 0.45% of the introduced amount.

SEM/EDX analysis of PRS11 is in progress.

- **Experiment PRS12**

Table 2.40 gives the PRS12 experimental procedure.

Table 2.40 –PRS12 experimental procedure

Time from the experiment start, s	Stage
0-1030	Startup heating , molten pool formation .Charge is added and molten pool is homogenized. Temperature on the molten pool surface is 2490°C.
1066-1076	Molten pool depth and bottom crust thickness are measured. They are 34 and 15mm respectively.
1076-2000	Power deposition into the melt is increased to melt the bottom crust. Temperature on the melt surface is 2625°C
2050-2055	Molten pool depth and bottom crust thickness are measured. They are 42 and 5mm respectively
2249-2271	Crucible is shifted up by 30 mm to initiate the crystallization process.
2443-2546	1st melt sample is taken
2573-2599	VPA IMCC measurement #1
2814-2861	2nd melt sample is taken
2910	VPA IMCC measurement #2.

3116-3145	3rd melt sample is taken
3253	VPA IMCC measurement #3.
3401-4144	UO_2 is added, molten pool is homogenized. Power deposition in the melt is increased. Temperature on the molten pool surface is 2700°C
4699-4800	Molten pool depth and bottom crust thickness are measured. They are 45 and 5mm respectively
4423-4458	4th melt sample is taken
4578	VPA IMCC measurement #4.
4707-4758	5th melt sample is taken
4839	VPA IMCC measurement #5.
5004-5054	6th melt sample is taken
5178	VPA IMCC measurement #6
5307	HF heating is disconnected. The ingot is crystallized in nitrogen and cooled..

Fig. 2.50. shows the pyrometer readings (T_{mel}), plate voltage (U_a), current (I_a), heat transfer from the crucible (Q_{ccr}) versus time. Figures 2.51-2.56 show thermogram fragments at the time of liquidus temperature measurement.

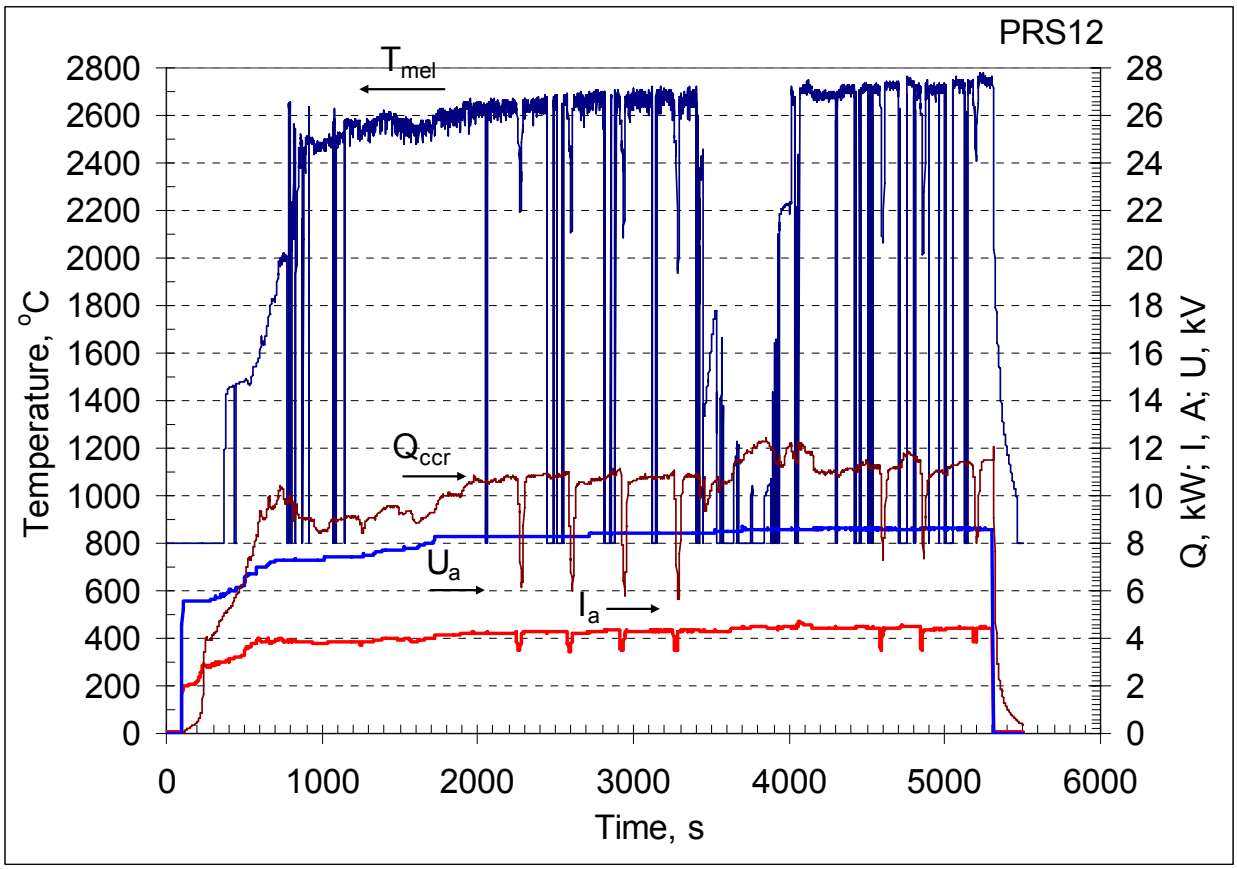

Fig. 2.50- Pyrometer readings (T_m), voltage (U_a), plate current (I_a), heat flux into the crucible (Q_{ccr}) and melt surface temperature (T_{mel}) versus time in PRS12

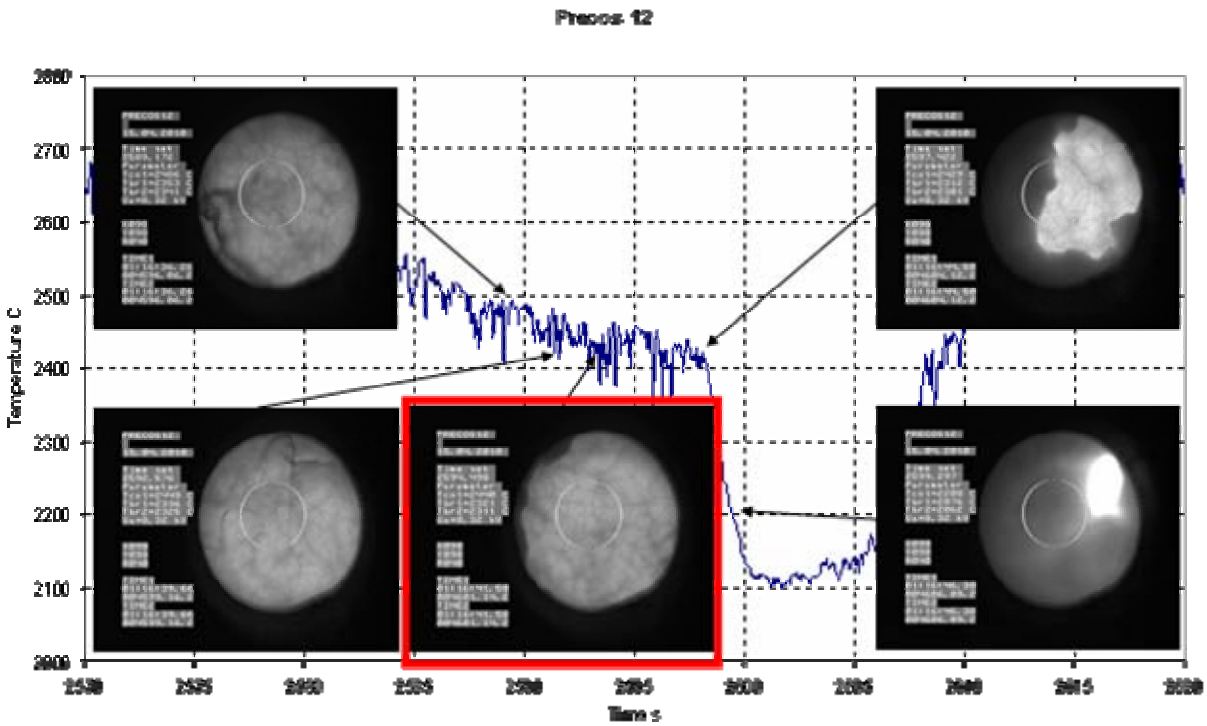

Fig. 2.51- PRS12 thermogram fragment during the VPA IMCC measurement #1

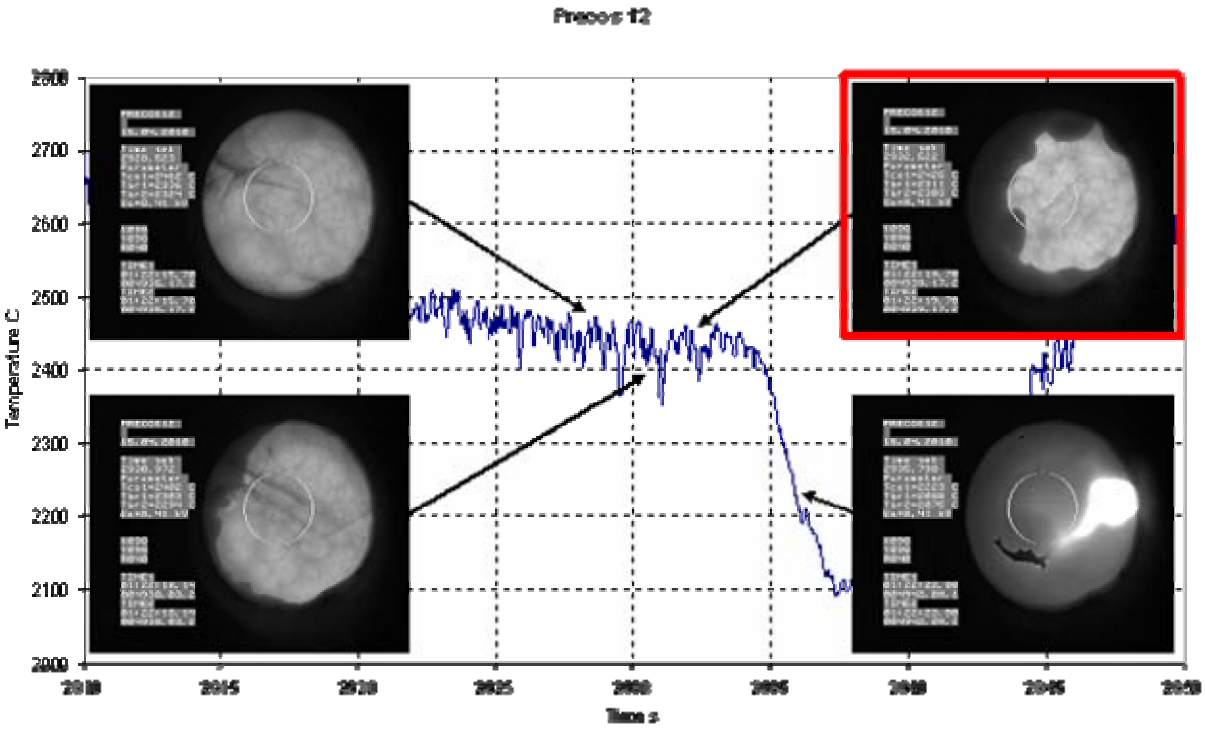

Fig. 2.52- PRS12 thermogram fragment during the VPA IMCC measurement #2

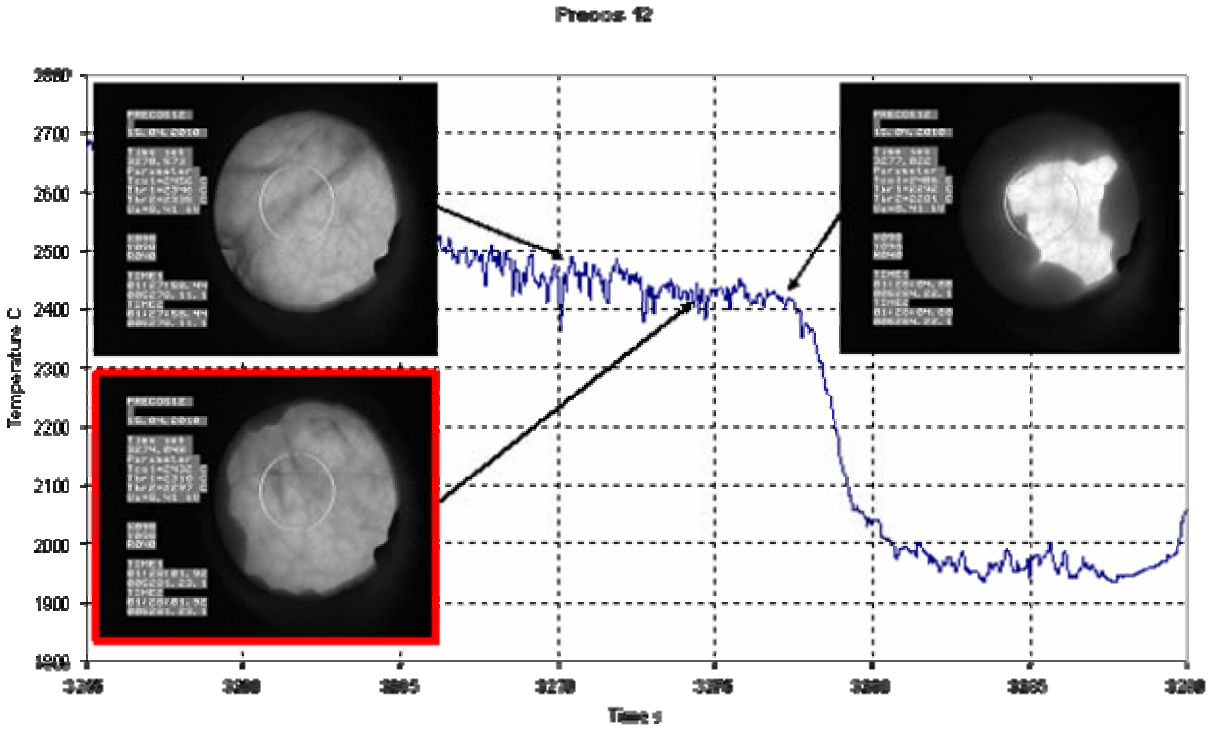

Fig. 2.53- PRS12 thermogram fragment during the VPA IMCC measurement #3

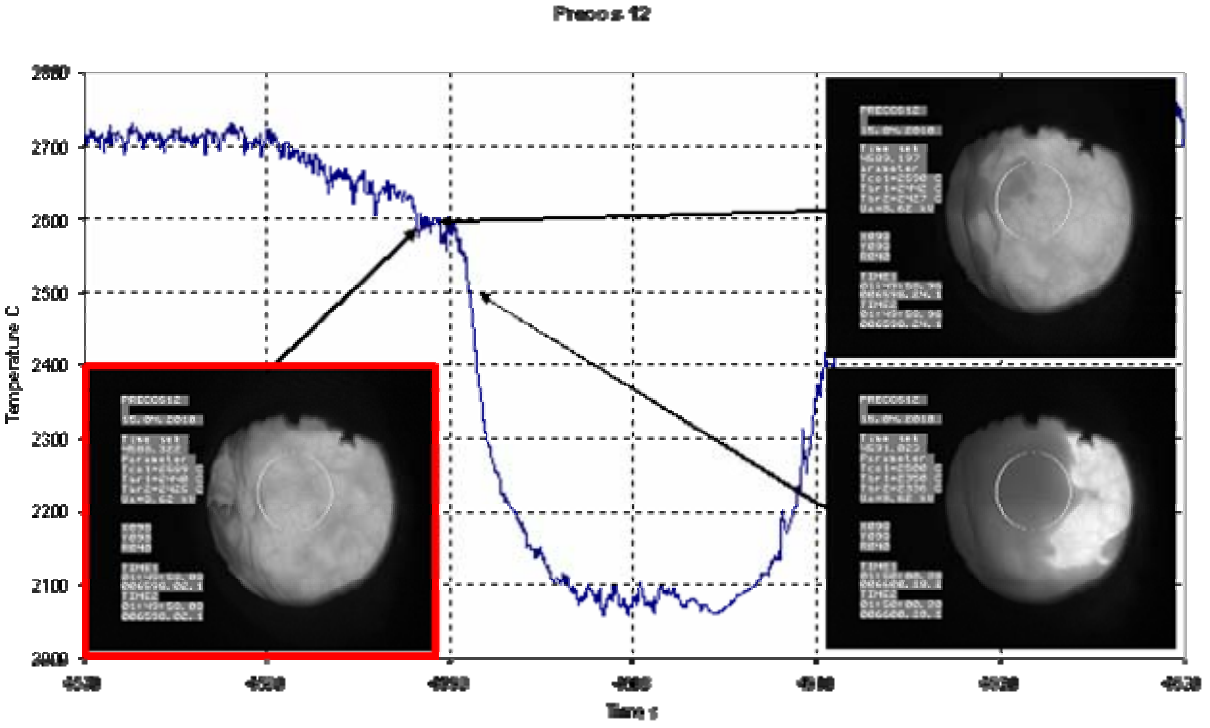

Fig. 2.54- PRS12 thermogram fragment during the VPA IMCC measurement #4

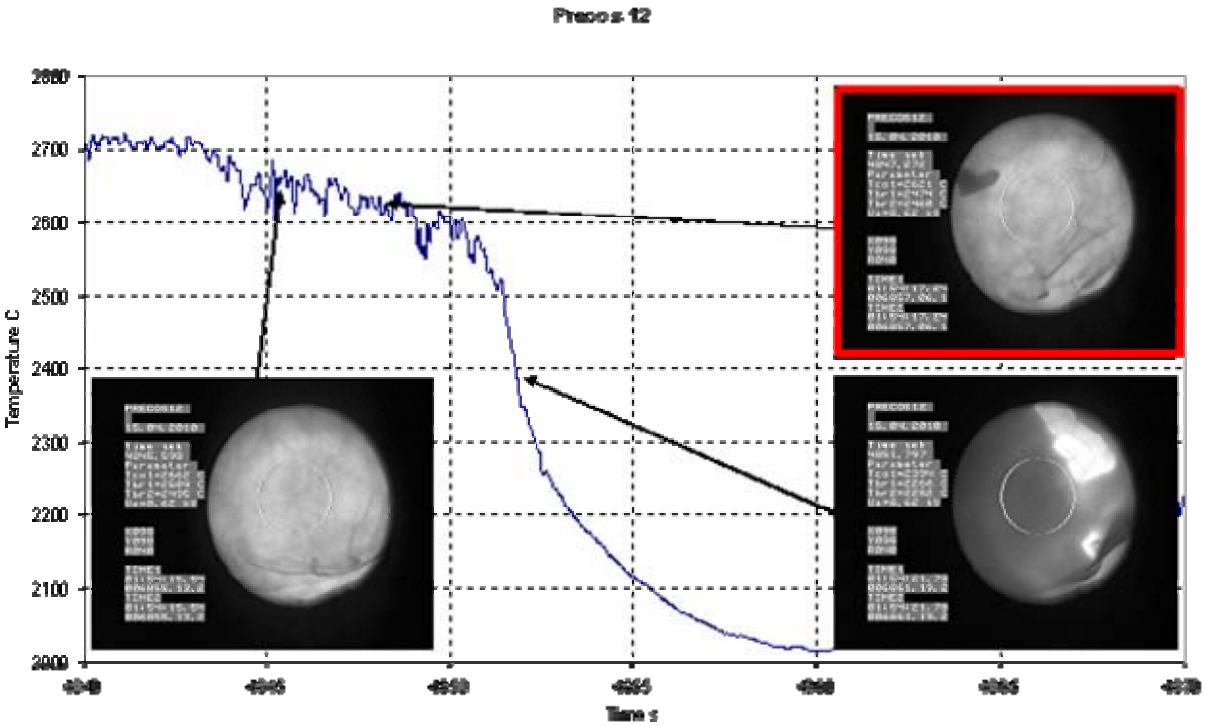

Fig. 2.55- PRS12 thermogram fragment during the VPA IMCC measurement #5

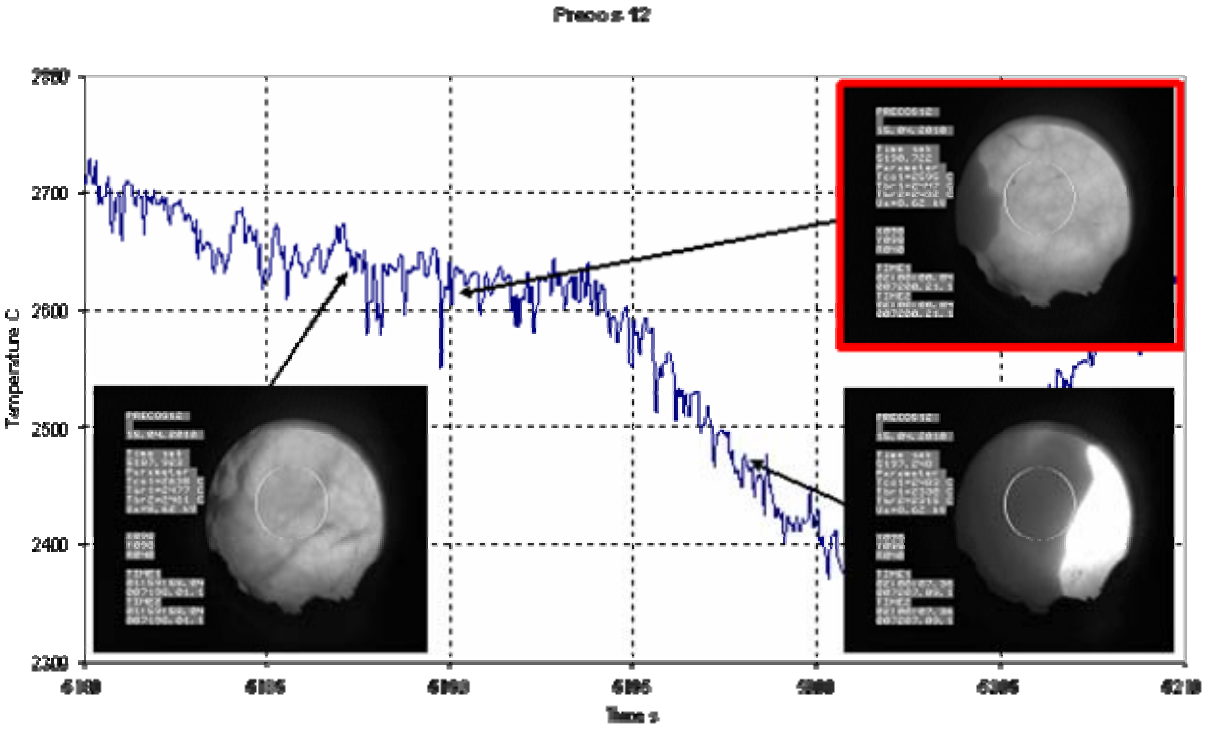

Fig. 2.56- PRS12 thermogram fragment during the VPA IMCC measurement #6

Mass balance of experiment PRS12 is shown in Table 2.41.

Table 2.41 - PRS12 mass balance

Introduced into melt		Collected, g	
UO_2	301.63	**Ingot**	302.56
CaO	42.70	**Samples**	48.24
U	5.00	**Probe sample**	66.07
Addition	170.73	**Aerosols**	8.51
		Above-melt crust	68.25
		Spillages [1)]	28.22
Σ	**520.06**	**Σ**	**521.85**
Imbalance	**+1.79**		

Note:
[1)] – Spillages- unreacted charge and aerosols, collected from sections when the crucible was disassembled.
.

Table 2.42 shows the chemical analysis data of molten products and elemental material balance of experiment PRS12 recalculated for oxides s.

Table 2.42 – PRS12 chemical analysis of corium samples and elemental material balance

Item	Content, mass%		Mass, g	Mass, g	
	UO_2	**CaO[1)]**		**UO_2**	**CaO**
Melt sample #1	86.6	13.4	4.85	4.20	0.65
Melt sample #2	84.08	15.92	6.43	5.41	1.02
Melt sample #3	87.52	12.48	6.94	6.07	0.87
Melt sample #4	92.39	7.61	16.7	15.43	1.27
Melt sample #5	89.86	10.14	9.32	8.37	0.95
Melt sample #6	89.54	10.46	4	3.58	0.42
Probe sample	91.37	8.63	66.07	60.37	5.7
Aerosols[2)]	92.25	7.75	8.51	7.85	0.66
Above-melt crust	89.29	10.71	68.25	60.94	7.31
Spillages [3)]	88.22	11.78	28.22	24.9	3.32
Ingot	92.52	7.48	302.56	279.92	22.64
Collected, g				477.05	44.80
Introduced, g				478.03	42.70
Imbalance, g				-0.98	+2.10

Note:
[1)]- calculated from the residue.
[2)] – aerosols collected by the F3 filter were analyzed; their composition was identical to all aerosols of the experiment.
3) – spillages- unreacted charge and aerosols, collected from sections when the crucible was disassembled

UO_2 imbalance (-0.98 g), and CaO imbalance (+2.10 g), amount to 0.2 and 4.9 % of the introduced quantity. It is explained mostly by the error, which for U is 5 rel.%.

Table 2.43 shows XRF data of corium samples and elemental material balance of experiment PRS12 recalculated for oxides..

Table 2.43- XRF data of corium samples and elemental material balance of experiment PRS12

Item	Content, mass%		Mass, g	Mass, g	
	UO_2	CaO		UO_2	CaO
Melt sample #1	85.49	14.51	4.85	4.15	0.70
Melt sample #2	86.12	13.88	6.43	5.54	0.89
Melt sample #3	85.53	14.47	6.94	5.94	1.00
Melt sample #4	91.93	8.07	16.7	15.35	1.35
Melt sample #5	91.86	8.14	9.32	8.56	0.76
Melt sample #6	91.32	8.68	4	3.65	0.35
Probe sample	93.22	6.78	66.07	61.59	4.48
Aerosols[1)]	92.25	7.75	8.51	7.85	0.66
Above-melt crust	93.1	6.9	68.25	63.54	4.71
Spillages [2)]	78.09	21.91	28.22	22.04	6.18
Ingot	93.17	6.84	302.56	281.88	20.68
Collected, g				480.09	41.76
Introduced, g				478.03	42.7
Imbalance, g				+2.06	-0.94

Note:
1) aerosols collected by the F3 filter were analyzed; their composition was identical to all aerosols of the experiment.
2) spillages- unreacted charge and aerosols, collected from sections when the crucible was disassembled

Imbalance for uranium oxide (+2.06 g), and for calcium oxide (-0.94 g),is 0.4 and 2.2% of the introduced amount.

SEM/EDX analysis of PRS12 is in progress.

Conclusions on the UO_2 – CaO system

Table 2.44 gives the comparison of XRF and chemical analysis data for samples collected during the experiments. The comparison of data has shown that the difference in the content of elements determined by different methods in the PRS11,12 samples is smaller than for PRS10. This is because the XRF of PRS10 samples was made by the method of regressive analysis using calibration specimens. For that samples from previous experiments were used. U content in them was determined by the chemical analysis. A difference between PRS10 data was considerable. XRF of PRS11, 12 samples was made by the method of fundamental parameters (MFP), and $Ca_3(PO4)_2$ was used as the reference sample. At this the difference between the data provided by the two methods was diminished.

As SEM/EDX analysis of the melt samples and eutectic regions of ingots from experiments is still in progress, the diagram of Fig. 2.57 shows the results provided both by ChA and XRF. Compositions corresponding to measured liquidus temperatures will be specified after the EDX analysis is completed.

Table 2.44. Comparison of XRF and chemical analysis data for the UO_2-CaO system

Experiment	Item	Content, mass% / mol.%			
		XRF		Chemical analysis	
		UO_2	CaO	UO_2	CaO[1)]
PRS10	Melt sample #3	76.19±0.78 41.40	23.81	73.60±1.48 38.10	26.4
	Melt sample #4	74.01±0.77 38.6	25.99	71.55±1.45 35.70	28.45
PRS11	Melt sample #1	69.38±0.69 32.00	30.62	67.88±1.36 30.50	32.12
	Melt sample #2	70.25±0.70 32.90	29.75	67.46±1.37 31.00	32.54
	Melt sample #3	71.72±0.72 34.50	28.28	68.18±1.36 30.80	31.82
PRS12	Melt sample #1	85.49±0.85 55.03	14.51	86.60±1.73 57.30	13.4
	Melt sample #2	86.12±0.86 56.30	13.88	84.08±1.69 52.30	15.92
	Melt sample #3	85.53±0.86 55.10	14.47	87.52±1.75 59.30	12.48
	Melt sample #4	91.93±0.92 70.30	8.07	92.39±1.85 71.60	7.61
	Melt sample #5	91.86±0.92 70.10	8.14	89.86±1.80 64.80	10.14
	Melt sample #6	91.32±0.92 68.60	8.68	89.54±1.79 64.00	10.46

Note:
1) – calculated from the residue.

Experimental data on liquidus temperatures of different compositions are given in Table 2.45.

Table 2.45- Measured liquidus temperatures in experiment PRS10-12

Experiment	Item	Content UO_2, mol.%		T_{liq}, °C
		XRF	ChA	
PRS10	Melt sample #3	41.40	38.10	**1876±28**
	Melt sample #4	38.6	35.70	**1886±29**

Experiment	Item	Content UO_2, mol.%		T_{liq}, °C
		XRF	ChA	
PRS11	**Melt sample #1**	32.00	30.50	**1912±29**
	Melt sample #2	32.90	31.00	**1910±29**
	Melt sample #3	34.50	30.80	**1907±29**
PRS12	**Melt sample #1**	55.03	57.30	**2440±36**
	Melt sample #2	56.30	52.30	**2420±36**
	Melt sample #3	55.10	59.30	**2432±36**
	Melt sample #4	70.30	71.60	**2589±39**
	Melt sample #5	70.10	64.80	**2620±39**
	Melt sample #6	68.60	64.00	**2595±39**

Preliminary experimental results confirm the Halk Холк version on the UO2-CaO phase diagram in the liquidus domain and specify it in the liquidus line coordinates and eutectic point, CaO solubility limit in the UO_2-based solid solution

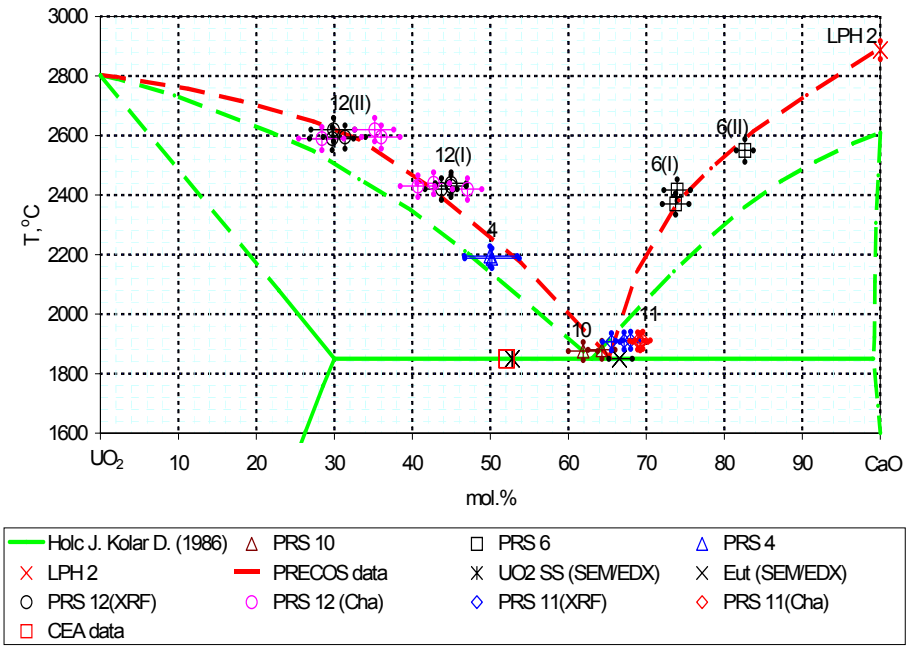

Fig. 2.57– Comparison of results with available UO_2-CaO phase diagrams

Task 3 Study of ternary oxidic systems.
Subtask 3.2 Experimental investigations and analysis of produced data.

In the studies of ternary oxidic systems UO_2-FeO-SiO_2 and UO_2-FeO-CaO the VPA IMCC method (Experiments of the PRS series), high-temperature annealing in the Galakhov microfurnace followed by the specimen (Experiments of the GPRS series) and SEM/EDX analysis were used.

Experiments PRS13, 14 were performed on the Rasplav-4 test facility Furnace schematics is given in Fig 2.1.

Experiments GPRS33-36 were performed in the Galakhov microfurnace. The Galakhov furnace schematics is given in Fig. 2.2.

For the UO_2-FeO-SiO_2 system: one large-scale experiment PRS13 and four experiments in the Galakhov microfurnace were performed. For the UO_2-FeO-CaO system – one large-scale experiment PRS14.

Experimental matrix of the PRS system is given in table 3.1.

Table 3.1- Experimental matrix of the PRS series

Test	Charge composition, mol.%				Objectives
	UO_2	FeO	CaO	SiO_2	
PRS 13	30.0	46.7	-	23.3	Determine T_{liq} by VPA IMCC. Ingot removal from the crucible at 9 mm/h to form the eutectic core and equilibrium structures of solid solution

The GPRS experimental matrix is given in Table 3.2.

Table 3.2- The GPRS experimental matrix

Test	Charge composition, mol.%			Annealing temperature, °C	Exposition, min
	UO_2	FeO	SiO_2		
GPRS33	5.0	25.0	70.0	1100	60
				2100	5
GPRS34	10.0	10.0	80.0	1100	60
				1850	5
GPRS35	20.0	7.0	73.0	1100	60
				1950	5
GPRS36	1.7	32.8	65.5	1100	60
				1300	20
				1300-900	240

- **Experiment PRS13**

Table 3.3 gives the PRS13 experimental procedure.

Table 3.3–PRS13 experimental procedure

Time from the experiment start, s	Stage/event
0-789	Startup heating , molten pool formation .Charge is added and molten pool is homogenized. Temperature on the molten pool surface is 2420C.
789-795	Molten pool depth and bottom crust thickness are measured. They are 63 and 5mm respectively.
1094-1130	Crucible is shifted up by 30mm to the position at which the crystallization starts. Melt temperature before the shift - 2230C. The upward shift did not result in the crust formation.
1239-1263	Another upward shift by 50 mm to fix the position for film crust formation. Melt temperature before the shift -2246C. The upward shift did not produce crusts.
1535-1616	Molten pool depth and bottom crust thickness are measured. They are 60 and 10mm respectively
1829-2460	Power deposition into the melt is lowered to reduce temperature on the melt surface. It was 2250C. Crust formation on the molten pool surface was registered.
1589-1631	1st melt sample is taken.
1707-1755	VPA IMCC #1
1990-2023	2nd melt sample is taken by two samplers
2054-2105	VPA IMCC #2
2289-2323	3rd melt sample is taken by three samplers.
2375-2440	VPA IMCC #3
2535-2560	4th melt sample is taken by three samplers.
2658-2669	HF heating is interrupted and liquidus temperature is measured
2710-3175	Power deposition into the melt is lowered to reduce temperature on the melt surface. The temperature was 2200C
3175-3253	Crucible is moved down versus the inductor before the plate current starts changing.
3276-16400	Ingot is pulled out of the inductor at the speed of 9 mm/h
16401	HF heating is disconnected. The ingot is crystallized in nitrogen and cooled

Fig. 3.1 shows the pyrometer readings (T_{mel}), plate voltage (U_a), current (I_a), heat transfer from the crucible (Q_{ccr}) versus time . Figures 3.2 – 3.5 show thermogram fragments at the time of liquidus temperature measurement.

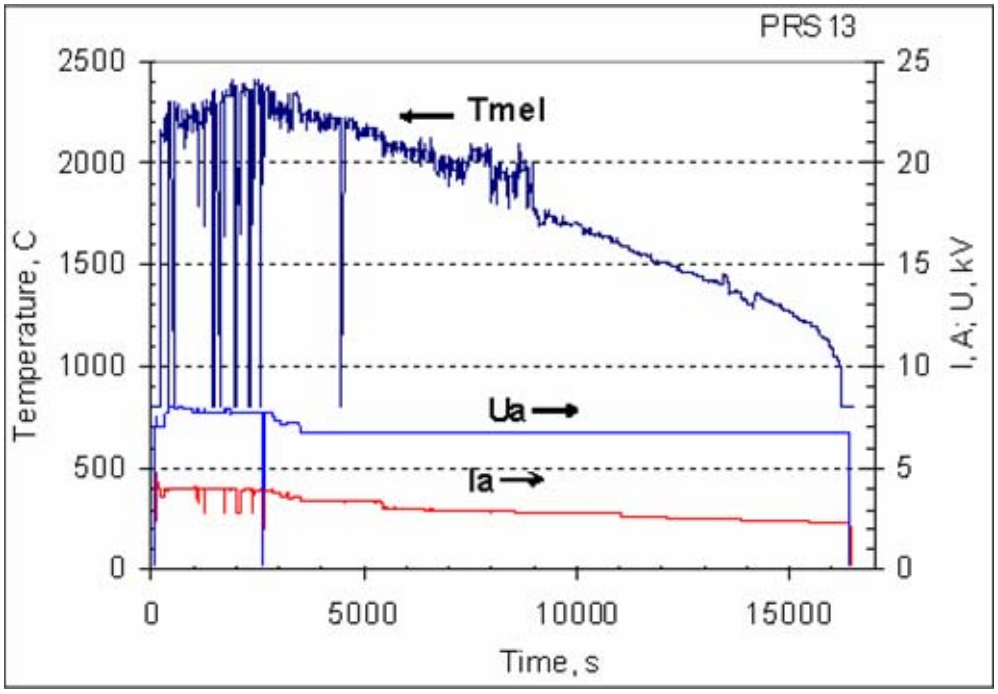

Fig. 3.1 – Pyrometer readings (T_{mel}), plate voltage (U_a), current (I_a), versus time in PRS13

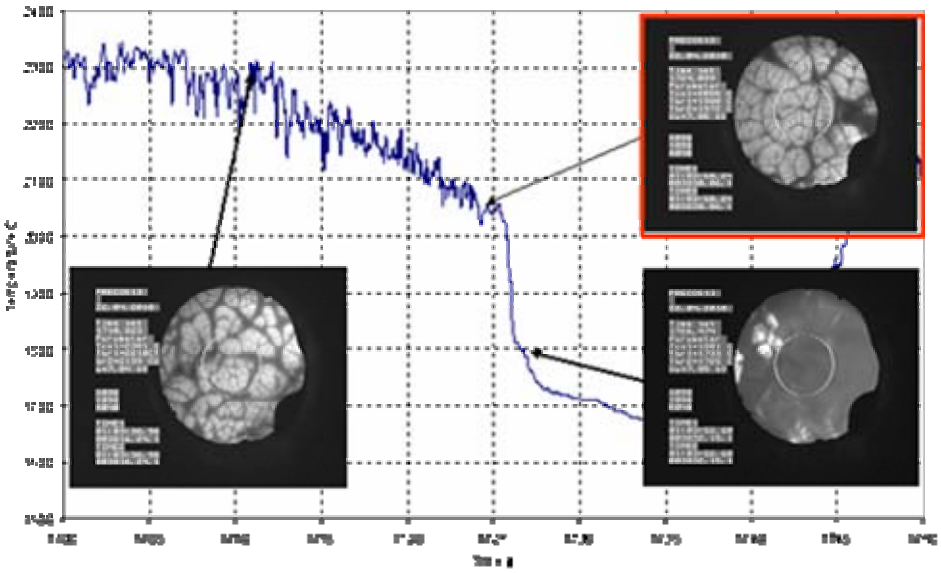

Fig. 3.2- PRS13 thermogram fragment during VPA IMCC # 1 measurement

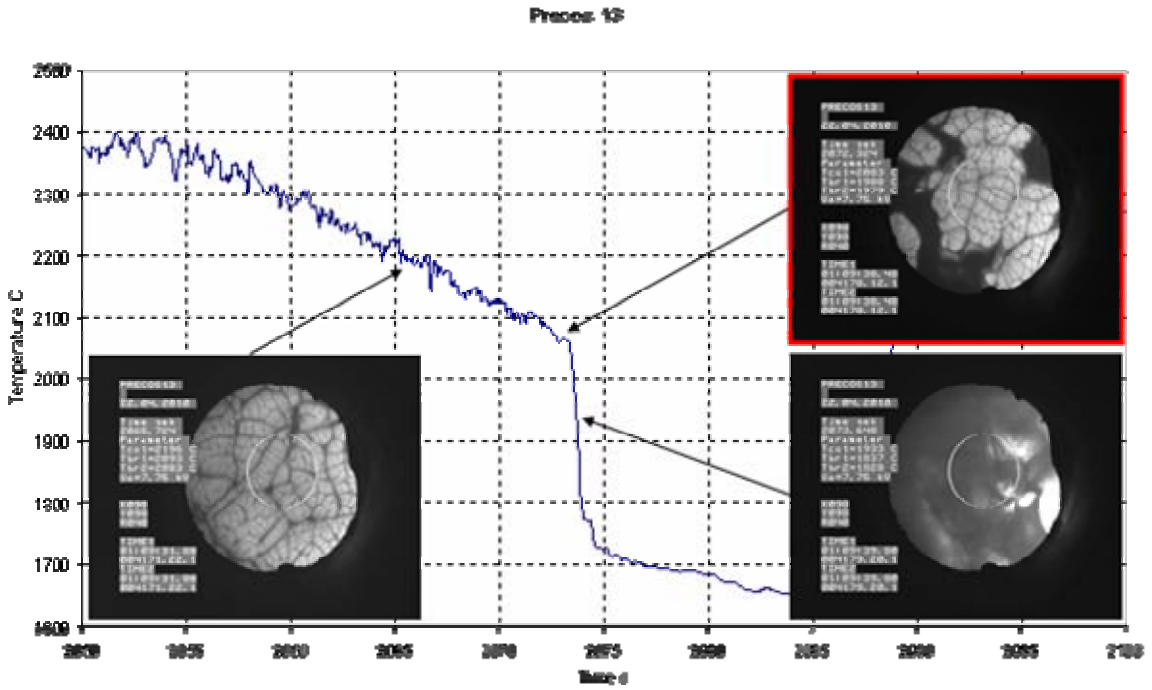

Fig. 3.3- PRS13 thermogram fragment during VPA IMCC # 2

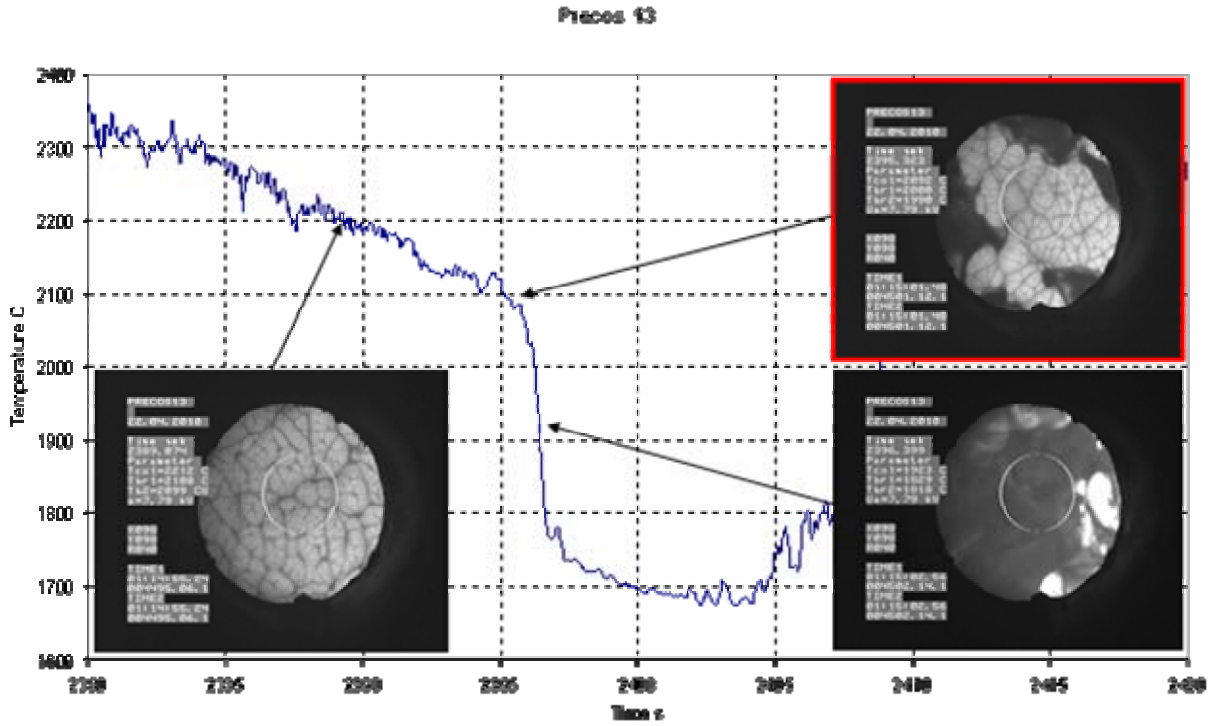

Fig. 3.4- PRS13 thermogram fragment during VPA IMCC # 3

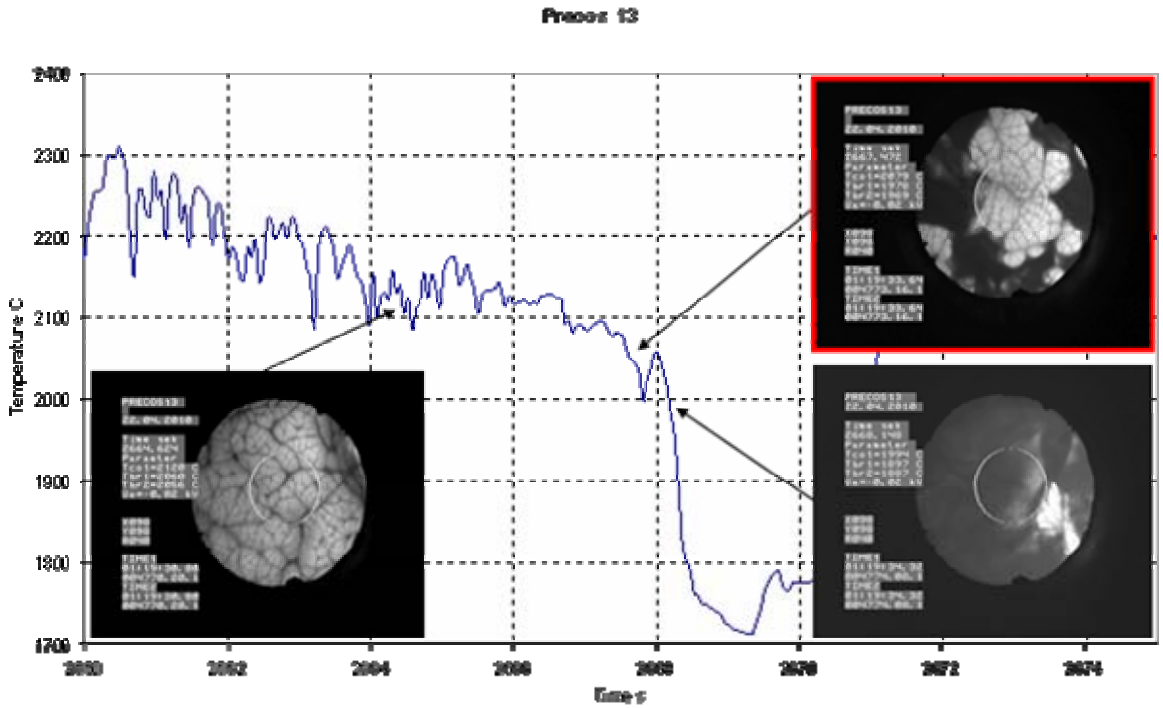

Fig. 3.5- PRS13 thermogram fragment when heating was interrupted

Liquidus temperatures measured in this experiment were 2055, 2083, 2092, 2079°C. Average T_{liq}=2077±30°C.

Fig**. 3.6** shows the axial section of PRS13 corium ingot**.**PRS13 ingot was included in the epoxy resin and cut along the axis. ½ of the ingot was used to make a polished section for SEM/EDX analysis, and an average sample was made from the second half for the physicochemical analysis. The bottom part of PRS13 corium ingot had a metallic inclusion of 1.1 g.

Fig 3.6 shows the axial section of the PRS13 ingot.

Fig. 3.6- Axial section of PRS13 ingot

Table 3.4 shows the PRS13 mass balance.

Table 3.4 - PRS13 mass balance

Introduced into melt		Collected, g	
UO_2	245.75	**Ingot**	256.97
FeO	91.85	**Melt samples**	23.49
Fe	14.26	**Spillages**	32.39
SiO_2	48.53	**Aerosols**	11.11
		Above-melt crust	33.22
		Spillages [1)]	38.62
Σ	**400.39**	**Σ**	**399.15**
Imbalance	**-1.24 (0.31%)**		

Note:
[1)] Spillages - unreacted charge and aerosols dropped from sections when the crucible was disassembled.

A 1.1 g metallic inclusion was found in the bottom part of PRS13 ingot. The ingot mass is much smaller than the charge mass For this reason it is impossible to derive melt composition from the charge.

Physicochemical analysis of PRS13 corium samples, which were taken when liquidus temperature was measured, is in progress.

- **Experiments GPRS33-36**

With only exclusion of GPRS36 all GPRS experimental procedures were similar and included:

1 - Weighing of empty crucible.
2 -Layer-by-layer filling of crucible with charge and compacting of each layer.
3 -Weighing of crucible with charge.
4 - Crucible installation into the furnace,
5 - Degassing of furnace internal space and filling it with argon-hydrogen mixture (Ar+4.2 vol % H_2) at 3 atm. pressure
6 - Heating is turned on and exposition is made at 1100°C during 60 minutes.
7 - Stepwise heating to the specified temperature.
8 - Specimen exposition for 10 min followed by its dropping into the quenching chamber (7).
9 - Crucible is taken from the chamber after cooling, cut along the axis, a polished section is prepared for SEM/EDX analysis

For GPRS36 the procedure was the same from 1 to 7 point. After that it was cooled from the fixed temperature of 1300 to 900°C during 240 min.

Samples of GPRS33-36 experiments were subjected to the SEM/EDX analysis.

- **Experiment PRS14**

Table 3.5 shows the PRS14experimental procedure

Table 3.5 –PRS14 experimental procedure

Time from the experiment start, s	Stage
0-2000	Startup heating , molten pool formation .Charge is added and molten pool is homogenized. Temperature on the molten pool surface is 1420C.
2002-2012	Molten pool depth and bottom crust thickness are measured. They are 38 and 12 mm respectively.
2097-2209	Crucible is shifted up by 40mm to the position at which film crusts are formed. Melt temperature before the shift 1420C. The upward shift did not result in the crust formation.
2595-2733	1st melt sample is taken with 2 samplers
2787-2875	VPA IMCC #1
3204-3230	2nd melt sample is taken
3280-3352	VPA IMCC #2
3463-3521	3rd melt sample is taken with two samplers
3565-3619	VPA IMCC #3
3931-3969	4th melt sample is taken
4064-4330	Power deposition into the melt is lowered to reduce temperature on the melt surface
4430-4510	Crucible is moved down versus the inductor before the plate current starts changing
4519-25880	Ingot is pulled out of the inductor at the speed of 9 mm/h
26880	HF heating is disconnected. The ingot is crystallized in nitrogen and cooled

Fig. 3.7 shows pyrometer readings (T_{mel}), plate voltage (U_a), current (I_a), heat transfer from the crucible (Q_{ccr}) versus time . Figures 3.8 – 3.9 show thermogram fragments at the time of liquidus temperature measurement.

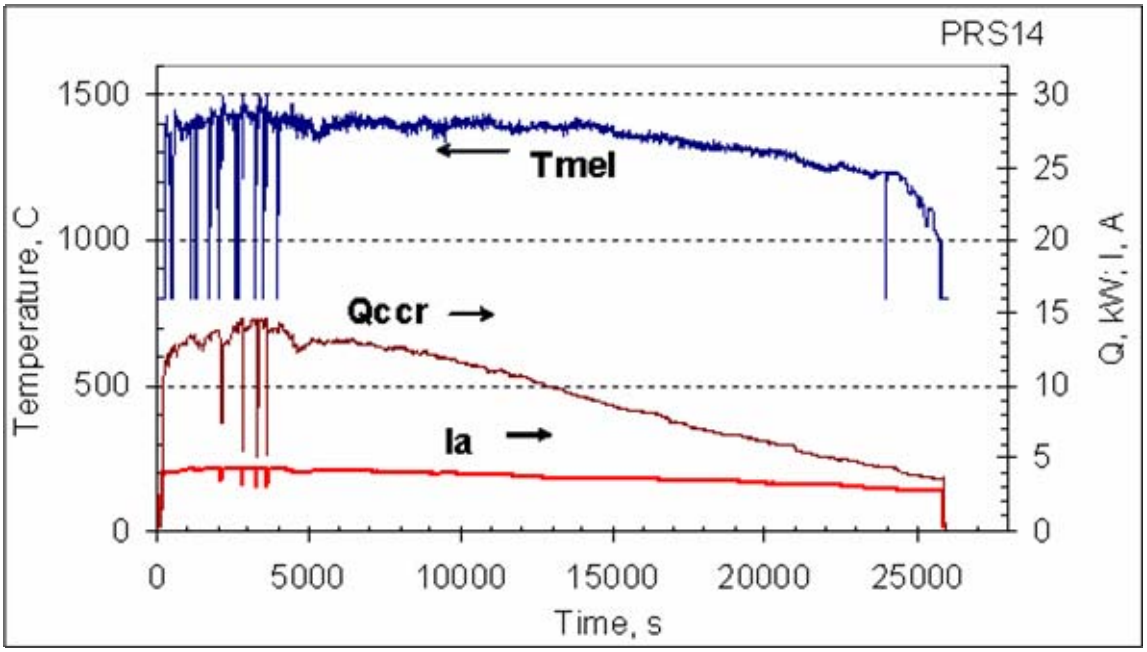

Fig. 3.7 - PRS14 plate voltage (U_a), current (I_a), and pyrometer readings (T_{mel}) versus time in

Three measurements of Tliq were made by VPA IMCC, but measurement #1 could not be derived from the video recording.

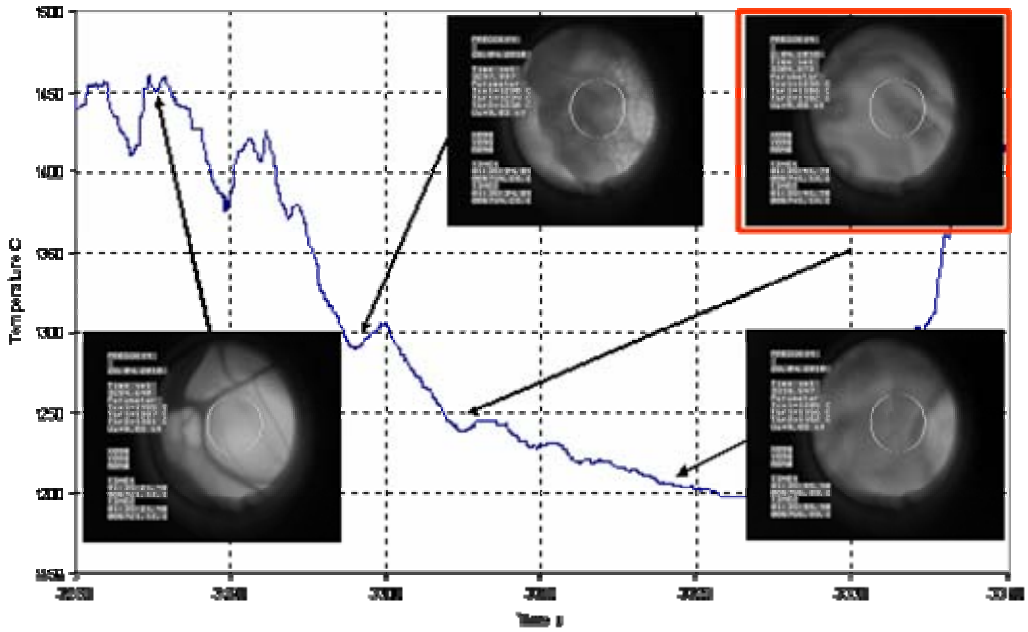

Fig. 3.8- PRS14 thermogram fragment during VPA IMCC #2

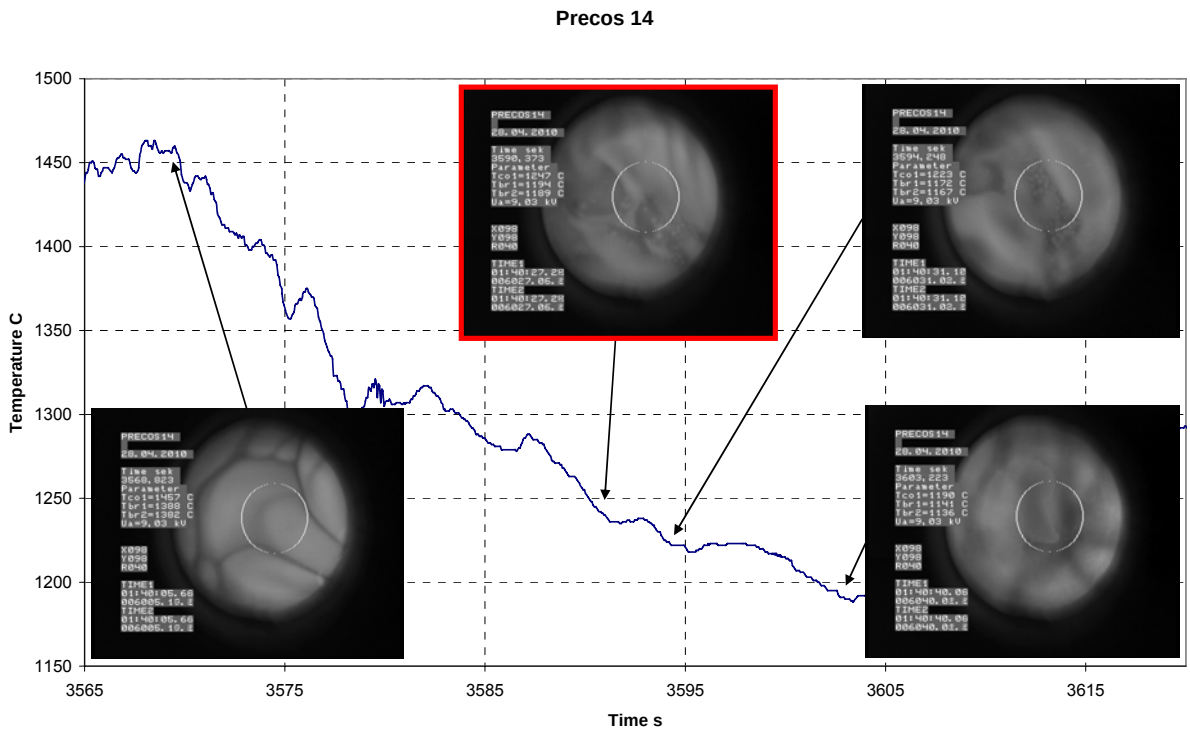

Fig. 3.9- PRS14 thermogram fragment during VPA IMCC #3

Liquidus temperatures measured in this experiment were 1238, 1247°C. Average T_{liq}=1243±20°C.

Fig. 3.10 shows the PRS14 corium ingot.

After the experiment the ingot was taken out of the crucible, weighed and included in the epoxy resin. ½ of the ingot was used to make a polished section for SEM/EDX analysis, and an average sample was made from the second half for the physicochemical analysis. Fig. 3.10 shows the PRS14 ingot.

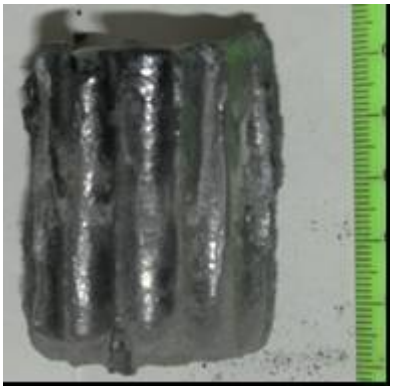

Fig. 3.10 – Corium ingot of experiment PRS14

Mass balance of experiment PRS14 is given in Table 3.6.

Table 3.6 – Mass balance of experiment PRS14

Introduced into melt, g		**Collected, g**	
UO_2	60.20	**Melt samples**	17.05
FeO	180.80	**Ingot**	276.10
Fe	22.40	**Aerosols**	2.49
CaO	39.60	**Spillages** [1)]	6.79
Σ	**303.00**	**Σ**	**302.43**
Imbalance	**-0.57 (0.19%)**		

Note: [1)] Spillages – unreacted charge and aerosols spilled from sections, when crucible was disassembled.

Imbalance in PRS14 is insignificant.

Physicochemical analysis of PRS14 corium samples taken during the liquidus temperature measurements is in progress.

3. References

1. V.V. Gusarov, L.P. Mezentseva, V.I. Almyashev et al. Report on research work "Study of binary oxidic systems: System UO2–SiO2», SPb., 2004 .
2. S.V. Elinson, T.I. Nezhnova // Industrial laboratory, 1964. V. 30, №4.
3. V.G. Goriushina, E.V. Romanova, T.A. Archakova // Industrial laboratory, 1961, V. 27, №7.
4. Methods for determining O/U ration in the prestoichiometric uranium dioxide. // radiochemistry, 1994. V. 36, № .3. C.
5. N.F. Losev. Quantitative X-Ray fluorescence analysis. M.: Nauka, 1969.

1. Current technical status

- Activities are carried out in accordance with schedule, with an exclusion for the U-Zr-Fe-O system – the investigation is postponed due to a delay in granting the permit for uranium handling to the partner-institute IHT RAS

2. Cooperation with foreign collaborators

Foreign collaborators within the project are well-known experts representing EU scientific research centers:

1. Dr. Marc Barrachin), France
   IRSN/DRS/SEMAR/CEN Cadarache
2. Dr. Fransoise Defoort, France
3. Dr. Alexei Miassoedov, Germany
   Forschungszentrum Karlsruhe GmbH, IKET
4. Dr. David Bottomley, Germany
   EUROPAISCHE KOMISSION, Institut fur Transurane (ITU)

5. Dr. Pascal Piluso, France
   CEA Cadarache – DEN/DTN/STRI
6. Manfred Fischer, Germany
   AREVA NP GmbH
7. Dr. Sieghard Hellmann, Germany
   AREVA NP GmbH

The Project is implemented in close cooperation with foreign collaborators, in particular: detailed discussion and approval of Work Plan and experimental matrix; analysis and evaluation of results of each experiment; introduction of updates into the experimental specifications; numerical analyses carried out in parallel; preparation of joint papers and contributions into conferences.

Discussion of the scope of work and results achieved within the PRECOS project took place at the joint meetings with collaborators.

3. Problems encountered and suggestions to remedy

Research activities within Project 3813 produced essentially new and partially controversial results. Additional studies were necessary for their confirmation and explanation.

Due to the increased amount of work and changes in the actual expenditures on some budget items in comparison with those foreseen by the Work Plan, an update of the Project budget was made in the 8th Quarter (2nd year) without changing the total budget sum.

4. Perspectives of future developments of the research/technology

In discussion.